AFRL-RV-PS-
TR-2022-0038

STUDIES ON ATMOSPHERIC PROPAGATION EFFECTS AND ANTENNA DESIGN FOR W/V-BAND

Christos Christodoulou, et al.

University of New Mexico
Department of Electrical Engineering and Computer Engineering
MSC01 1100
Albuquerque, NM 87131-0001

30 November 2021

Final Report

AIR FORCE RESEARCH LABORATORY
Space Vehicles Directorate
3550 Aberdeen Ave SE
AIR FORCE MATERIEL COMMAND
KIRTLAND AIR FORCE BASE, NM 87117-5776

DTIC COPY

NOTICE AND SIGNATURE PAGE

AFRL-RV-PS-TR-2022-0038 HAS BEEN REVIEWED AND IS APPROVED FOR PUBLICATION IN ACCORDANCE WITH ASSIGNED DISTRIBUTION STATEMENT.

//SIGNED//	//SIGNED//
_____	_____
Dr. Steven A. Lane	For: Erin N. Pettyjohn, Chief
Program Manager/AFRL/RVB	AFRL Geospace Technologies Division

REPORT DOCUMENTATION PAGE

Form Approved
OMB No. 0704-0188

1. REPORT DATE *(DD-MM-YYYY)*	**2. REPORT TYPE**	**3. DATES COVERED** *(From - To)*
30-11-2021	Final Report	30 Aug 2016 – 30 Nov 2021

4. TITLE AND SUBTITLE
Studies on Atmospheric Propagation Effects and Antenna Design for W/V-band

5a. CONTRACT NUMBER
FA9453-16-2-0073

5b. GRANT NUMBER

5c. PROGRAM ELEMENT NUMBER
63401F

6. AUTHOR(S)
Christos Christodoulou, Steven A. Lane[1], Ralph L. Gesner, and Firas Ayoub

5d. PROJECT NUMBER
3682

5e. TASK NUMBER
EF129630

5f. WORK UNIT NUMBER
V15A

7. PERFORMING ORGANIZATION NAME(S) AND ADDRESS(ES)
University of New Mexico
Department of Electrical Engineering and Computer
Engineering MSC01 1100
Albuquerque, NM 87131-0001

[1]Air Force Research Laboratory
Space Vehicles Directorate
3550 Aberdeen Avenue SE
Kirtland AFB, NM 87117-5776

8. PERFORMING ORGANIZATION REPORT NUMBER

9. SPONSORING / MONITORING AGENCY NAME(S) AND ADDRESS(ES)
Air Force Research Laboratory
Space Vehicles Directorate
3550 Aberdeen Avenue SE
Kirtland AFB, NM 87117-5776

10. SPONSOR/MONITOR'S ACRONYM(S)
AFRL/RVBYC

11. SPONSOR/MONITOR'S REPORT NUMBER(S)
AFRL-RV-PS-TR-2022-0038

12. DISTRIBUTION / AVAILABILITY STATEMENT
Approved for public release; distribution is unlimited (AFRL-2022-1182 dtd 09 Mar 2022).

13. SUPPLEMENTARY NOTES

14. ABSTRACT
Work performed under this cooperative agreement between AFRL Space Vehicles Directorate and the University of New Mexico focused on research topics supporting development of military satellite communications capability using W/V-band (i.e., 81-86 GHz and 71-76 GHz). The primary accomplishment of this work was to develop and experimentally validate models of cloud absorption at W/V-band. Results demonstrate the uncertainty and limitations of cloud models. Results demonstrate the necessity to validate modeling tools using geostationary satellite beacon measurements. Work towards modeling depolarization effects at W/V-band is still ongoing. The second accomplishment was to develop and experimentally validate high-efficiency, high-gain W/V-band antenna to support wideband communications and circularly polarized signals. Results demonstrate significant improvements in manufacturability and electrical performance.

15. SUBJECT TERMS
space communication, W/V-band, propagation effects, antenna design

16. SECURITY CLASSIFICATION OF:			**17. LIMITATION OF ABSTRACT**	**18. NUMBER OF PAGES**	**19a. NAME OF RESPONSIBLE PERSON**
a. REPORT	**b. ABSTRACT**	**c. THIS PAGE**			Dr. Steven A. Lane
Unclassified	Unclassified	Unclassified	Unlimited	162	**19b. TELEPHONE NUMBER** *(include area code)*

ACKNOWLEDGMENTS

This material is based on research sponsored by Air Force Research Laboratory under agreement number FA9453-16-2-0073. The U.S. Government is authorized to reproduce and distribute reprints for Governmental purposes notwithstanding any copyright notation thereon.

DISCLAIMER

The views and conclusions contained herein are those of the authors and should not be interpreted as necessarily representing the official policies or endorsements, either expressed or implied, of Air Force Research Laboratory or the U.S. Government.

TABLE OF CONTENTS

TABLE OF CONTENTS (Continued)

LIST OF FIGURES

Figure **Page**

LIST OF FIGURES (Continued)

Figure **Page**

LIST OF FIGURES (Continued)

Figure **Page**

LIST OF FIGURES (Continued)

Figure **Page**

LIST OF FIGURES (Continued)

Figure **Page**

LIST OF FIGURES (Continued)

Figure **Page**

LIST OF TABLES

Table **Page**

This page is intentionally left blank.

1 SUMMARY

Work performed under this cooperative agreement between AFRL Space Vehicles Directorate and the University of New Mexico focused on research topics supporting development of military satellite communications capability using W/V-band (i.e., 81-86 GHz and 71-76 GHz). This report presents analysis and results of graduate student projects accomplished during the period of performance. Significant contributions to our success were provided by Government scientists, engineers, and contractor employees of the W/V-band Satellite Communications Experiment program.

The primary objective of this work was to develop and experimentally validate models of cloud absorption at W/V-band. This follows prior work to model precipitation effects at W/V-band that were accomplished and documented under a prior cooperative agreement. Signal attenuation due to clouds occurs more frequently than precipitation effects, but there has been much less effort to understanding and model cloud effects. Work towards modeling depolarization effects at W/V-band is still ongoing and will be reported upon completion.

This report presents fundamental concepts that are necessary for understanding absorption and scattering effects from the atmosphere, clouds, and precipitation at W/V-band. Concepts and calculations are illustrated using the Standard Atmosphere model and radiosonde data. The W/V-band Terrestrial Link Experiment (WTLE) was used to measure propagation effects in order to assess model performance. The W/V-band Terrestrial Link Experiment (WTLE) was established in 2015 in Albuquerque, NM, to enable W/V-band propagation studies. It was developed by scientists and engineers from the Air Force Research Laboratory, the University of New Mexico, and NASA Glenn Research Center. The propagation path between the transmitter and receiver is 24.3 km. The propagation path slant angle is 4.16°, which yields a vertical altitude change of about 1763 m. Results demonstrate the uncertainty and limitations of cloud models. Several recommendations are provided for future research efforts. Results also demonstrate the necessity to validate modeling tools using geostationary satellite beacon measurements.

The second objective was to develop and experimentally validate high-efficiency, high-gain W/V-band antenna to support wideband communications and circularly polarized signals. Prototype antenna were designed, fabricated, and tested. Results demonstrate significant improvements in manufacturability and electrical performance relative to prior antenna designs.

2 INTRODUCTION

2.1 Motivation

The frequency bands of 71-76 GHz (in the V-band) and 81-86 GHz (in the W-band) have been allocated by the International Telecommunications Union for fixed and mobile satellite service, but are currently unused. The W-band has been allocated for uplinks and the V-band for downlinks. W/V-band would substantially augment the bandwidth available for Government and commercial satellite communications[1]. Greater bandwidth means support for more users and increased data rate / quality-of-service for users. Since higher frequency systems can be made more directional, there is less potential for interference and more opportunity for frequency reuse. However, W/V-band is not as directional as laser communication, and therefore, can more readily support multiple users in a single region of interest[2].

There has been much development of W/V-band technology for point-to-point systems for terrestrial links (i.e., wireless "backhaul"). However, use of W/V-band for satellite communications is not as mature. Commercial satellite communication providers typically use portions of the Ka-band for uplinks and K-band for downlinks. Many commercial and Government systems use even lower frequencies for communication services. Thus, there has not been a clear business case for commercial satellite communication service providers to invest in and develop W/V-band satellite communication capability (although this is starting to change given the new mega-constellations that are in development). Rather, it has been the Air Force (and now Space Force) that is seeking spectrum options to provide more capacity and less vulnerability to interference and jamming.

Although there are various models of propagation effects at W/V-band, these models are generally extrapolations of models that have only been validated at lower frequencies. Signal absorption resulting from atmospheric water vapor is greater at W/V-band than at lower frequencies. Likewise, signal attenuation due to clouds (i.e., suspended water droplets) and rain (i.e., "rain-fade") is also greater at W/V-band than at lower frequencies. Models must be validated and/or the propagation effects statistically characterized before an operational communications satellite can be designed and developed. Link availability is directly dependent upon rain-fade and will drive the necessary power / aperture requirements.

Most of the hardware and software technology necessary for W/V-band satellite communications is mature and commercially available. Much of the technology used for terrestrial point-to-point links can be used for satellite communication links. The two notable exceptions are high power amplifier technology and antenna technology – particularly for the satellite transponder. The overall path losses are much greater for a satellite communications link than for a terrestrial point-to-point link, regardless of whether the satellite is in low earth orbit (LEO) or geostationary earth orbit (GEO).

[1] Convention is to indicate the uplink frequency / downlink frequency, resulting in W/V-band.
[2] Multi-access laser communication is more difficult to realize than multi-access W/V-band communication.

2.2 Objective

The two research objectives of this cooperative agreement were to (1) investigate atmospheric attenuation at W/V-band, and (2) investigate novel W/V-band antenna designs.

3 METHODS, ASSUMPTIONS AND PROCEDURES

This section begins with discussion of the communications link budget model. This frames the relevance of (1) understanding atmospheric attenuation at W/V-band, and (2) design of antenna for W/V-band.

Concepts of specific attenuation, optical thickness, and atmosphere opacity are described and illustrated using the Standard Atmosphere model and measured radiosonde profiles. Models for clear-day attenuation (i.e., absorption from atmosphere gases and water vapor), cloud absorptions, and precipitation extinction are presented and analyzed. Finally, the development the W/V-band Terrestrial Link Experiment (WTLE) test range is presented. WTLE is a unique propagation test range designed and operated by the Air Force Research Laboratory and the University of New Mexico under this cooperative agreement. Much of the work with WTLE is still on-going and will be reported separately in graduate student theses and dissertations.

Next, design and development of a novel rectangular waveguide antenna array for W/V-band is presented. This is followed by the design and development of a novel W/V-band cross-slotted waveguide-fed horn antenna. Both antenna designs were fabricated and experimentally evaluated using the W/V-band compact range test facility designed and operated by the University of New Mexico and the Air Force Research Laboratory under this cooperative agreement. Results have been documented in graduate student research papers and theses, and are summarized in this report.

3.1 Link Budget Model

For radio frequency (RF) communication links, performance is modeled using a "link budget" for the system or architecture. A link budget is a tabulation of parameters to estimate the received power for a given wireless communication path between a transmitter and receiver. These parameters include propagation path length, antenna gain, transmit power, and various sources of signal attenuation. The tabulation of parameters is reduced to an addition and subtraction problem through the use of the properties of the logarithm (decibel) scale. Once the received signal power is estimated, it can be compared to the expected noise power, which gives the signal-to-noise ratio (SNR). The carrier-to-noise ratio (CNR) is often used instead of SNR to characterize wireless communication links. Regardless, SNR or CNR are key performance metrics for satellite link budgets. From the SNR or CNR, the ratio of the energy-per-bit, E_b, to noise power spectral density, n_0, can be calculated (i.e., E_b/n_o), which then can be used to predict the probability of bit error for a digital communications link. Improved modeling of atmospheric losses will result in better estimates of the received power and therefore performance of the communications link.

Figure 1 illustrates a simple communications link. The transmitter antenna and the receiver antenna are separated by a distance, R, which is large enough for each to be in the far-field region of the

other. The ratio of received power to transmitted power between two antennas along a point-to-point link can be expressed using the Friis transmission equation given as:

$$\frac{P_r}{P_t} = \left(\frac{\lambda}{4\pi R}\right)^2 G_r\, G_t, \tag{1}$$

where λ is the wavelength of the electromagnetic signal, R is the path length, P_t is the transmitted power, P_r is the received power, and G_t and G_r are the antenna gain for the transmitter and receiver, respectively [1, 2]. The squared term is called the "free space loss" or "spreading loss" and is a function of wavelength and path distance, and is denoted as:

$$L_{FS} = \left(\frac{\lambda}{4\pi R}\right)^2. \tag{2}$$

Additional loss factors can be included to improve model accuracy, such as loss due to antenna pointing error (i.e., pointing loss, $L_{pointing}$), waveguide loss (i.e., transmission line loss, L_{TL}), and atmosphere losses (i.e., L_{atm}). Substituting yields:

$$P_r = L_{FS}\, G_r\, L_{pointing}\, L_{TL}\, L_{atm}\, G_t\, P_t. \tag{3}$$

Equation (3) can be expressed in terms of decibels as:

$$10 * \log_{10}(P_r) = 10 * \log_{10}(L_{FS}) + 10 * \log_{10}(G_r) + 10 * \log_{10}\left(L_{pointing}\right) + 10 * \log_{10}(L_{TL}) + 10 * \log_{10}(L_{atm}) + 10 * \log_{10}(G_t) + 10 * \log_{10}(P_t). \tag{4}$$

The link budget model can be expressed as shown in Table 1. Each parameter in the link budget is a function of frequency. Gains (i.e., values greater than 1) result in positive decibel numbers, while losses (i.e., values less than 1) result in negative decibel numbers. The next part of this section focuses on investigating and modeling atmosphere loss, L_{atm} at W/V-band. Subsequent sections focus on the antenna gain.

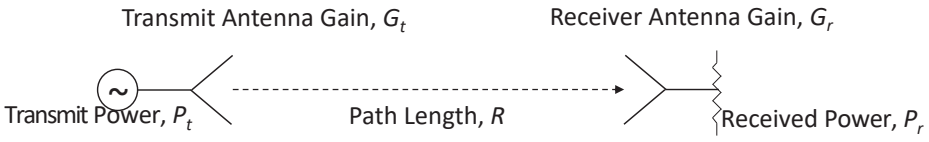

Figure 1. Diagram Illustrating Components of a Basic Radio Frequency Link

Table 1. Generalized Link Budget for a Basic Radio Frequency Link

Transmit Power	P_t	dB
Transmit Antenna Gain	G_t	dB
Atmosphere Loss	L_{atm}	dB
Transmission Line Loss	L_{TL}	dB
Pointing Loss	$L_{pointing}$	dB
Receive Antenna Gain	G_r	dB
Free Space Loss	L_{FS}	dB
Receive Power	P_r	dB

3.2 Atmospheric Propagation Effects

This section focuses on modeling atmospheric effects, specifically (1) absorption by oxygen molecules and water vapor (i.e., gaseous attenuation), (2) absorption by clouds (i.e., suspended water droplets), and (3) extinction (i.e., absorption and scattering) by precipitation. The Standard Atmosphere model and measured radiosonde profiles are described and used to illustrate concepts of optical thickness and opacity. Finally, the W/V-band Terrestrial Link Experiment (WTLE) is described.

3.2.1 Wave Propagation

A time-varying electric field induces a magnetic field and, conversely, a time-varying magnetic field induces an electric field. Electromagnetic (EM) waves may propagate in both lossless and lossy media. Waves propagating in a lossless medium (e.g., free space and perfect dielectrics[3]) do not attenuate. When propagating in a lossy medium (i.e., material with nonzero conductivity, such as water), part of the power carried by an EM wave gets converted into heat [3].

Regardless of its material composition, a small differential volume is characterized by four electromagnetic constitutive parameters:

$\varepsilon'\varepsilon_0$ = electrical permittivity (F/m)

μ = magnetic permeability (H/m)

[3] Materials interact with electric fields because they are composed, in part, of charged particles. When subjected to an electric field, these charges experience electric forces that cause them to move. How the charges move depends upon the nature of the material. Some materials, such as metals, possess charges that are free to move about the material as conduction currents. These materials are called conductors. Dielectrics, on the other hand, are composed of charges that are tightly bound to individual nuclei. These charges can move only small distances, but they can generate secondary electric fields that can substantially alter the total electric field, both inside and outside the material [4].

ρ_v = volume charge density (C/m^3)

σ = conductivity (S/m)

were ε_0 = 8.85e-12 F/m is the permittivity of free space and ε' is the permittivity of the material relative to that of free space. Examples of constitutive parameters include:

Free space:

$\varepsilon' = 1$

$\mu = \mu_0 = 4\pi \times 10^{-7}$ H/m (μ_0 denotes permeability in free space)

$\rho_v = 0$

$\sigma = 0$

Pure dielectric:

ε' = depends on the medium

$\mu = \mu_0 = 4\pi \times 10^{-7}$ H/m for all materials except ferromagnetic materials

$\rho_v = 0$

$\sigma = 0$

Conducting medium:

ε' = depends on the medium

$\mu = \mu_0 = 4\pi \times 10^{-7}$ H/m except for ferromagnetic materials

ρ_v = may or may not be zero

$\sigma \neq 0$

An EM wave can propagate through a dielectric medium (including free space) with no loss of energy (i.e., zero attenuation). In contrast, a conducting medium absorbs part of the energy carried by an EM wave, thereby attenuating it.

The phase velocity of an EM wave is given as:

$$u_p = \frac{\omega}{k} = \frac{\omega}{\omega\sqrt{\mu\varepsilon'\varepsilon_0}} = \frac{1}{\sqrt{\mu\varepsilon'\varepsilon_0}} \text{ (m/s)}, \tag{5}$$

where ω is the angular frequency (rad/sec) and k is the wavenumber. The wavelength is:

$$\lambda = \frac{2\pi}{k} = \frac{u_p}{f} \text{ (m)}, \tag{6}$$

where f is the frequency in Hz (cycles/sec or 1/sec). In vacuum (i.e., free space), $\varepsilon' = 1$ and $\mu = \mu_0$, and the phase velocity u_p is the speed of light given as c = 3e8 m/s. Therefore,

$$\lambda = \frac{c}{f} \text{ (m)}. \tag{7}$$

The index of refraction for a medium is denoted as n and is defined as the ratio of the phase velocity in free space to the phase velocity in the medium:

$$n = \frac{c}{u_p} = \sqrt{\frac{\mu_0 \varepsilon_0 \varepsilon'}{\mu_0 \varepsilon_0}} = \sqrt{\varepsilon'}. \tag{8}$$

In general, n is complex and can be expressed as:

$$n = n' - jn''. \tag{9}$$

The average relative dielectric constant of a material is denoted as ε and is complex and expressed as:

$$\varepsilon = \varepsilon' - j\varepsilon'', \tag{10}$$

where ε' is the relative permittivity of the material (as defined previously) and ε'' is its dielectric loss factor. The dielectric constant ε is related to the complex index of refraction n through:

$$\varepsilon = n^2. \tag{11}$$

For a plane wave propagating in a lossy medium in direction denoted as z, the electric field intensity at a distance z is given by:

$$E(z) = E_0 \exp(-\gamma z), \tag{12}$$

where E_0 is the field intensity at $z = 0$, and

$$\gamma = \alpha + j\beta, \tag{13}$$

where γ is the propagation constant, α is the absorption constant, and β is the phase constant of the medium. Terms are related to n and ε by:

$$\alpha = k_0 n'' = -k_0 \Im m\{\sqrt{\varepsilon}\} \quad \text{(Np/m)} \tag{14}$$

$$\beta = k_0 n' = k_0 \Re e\{\sqrt{\varepsilon}\} \quad \text{(rad/m)}, \tag{15}$$

where k_0 is the wavenumber in free space, and λ_0 is the free space wavelength in meters[4].

Similarly, for a plane wave propagating in a lossy medium in direction denoted as z, the power intensity (flux) at a distance is given by:

$$\mathcal{S}(z) = \mathcal{S}_0 \exp(-\kappa_e z) \quad (\text{W/m}^2), \tag{16}$$

where κ_e is the extinction coefficient:

$$\kappa_e = \kappa_a + \kappa_s \quad \text{(Np/m)}, \tag{17}$$

where κ_a is the absorption coefficient and κ_s is the scattering coefficient. In our frequency range of interest (i.e., 70 – 90 GHz), it is reasonable to ignore scattering losses ($\kappa_s = 0$) during clear-day

[4] The neper (Np) is the logarithmic unit for ratios of fields or power quantities. For Eq. (12), it is the natural logarithm (i.e., log) of $E(z)/E_0$. For Eq. (16), it is $\log(\mathcal{S}(z)/\mathcal{S}_0)$. Context must be considered.

atmosphere conditions (we will revisit this assumption later when we consider precipitation). Thus, the extinction coefficient is simply the absorption coefficient given by[5]:

$$\kappa_a = 2\alpha \quad \text{(Np/m)}, \tag{18}$$

where the units are nepers (Np) per unit length. The absorption coefficient is often specified in units of dB/km rather than Np/m. It can be shown that the conversion is[6]:

$$\kappa_a\left(\frac{\text{dB}}{\text{km}}\right) = 4342.9 * \kappa_a\left(\frac{\text{Np}}{\text{m}}\right), \tag{19}$$

or more precisely,

$$\kappa_a\left(\frac{\text{dB}}{\text{km}}\right) = 1000 * \log_{10}(e^1) * \kappa_a\left(\frac{\text{Np}}{\text{m}}\right). \tag{20}$$

Finally, the absorption coefficient is frequently referred to as the "specific attenuation". The next section will present a model for computing the absorption coefficient for clear-day atmosphere conditions.

3.2.2 Gaseous Attenuation

An electromagnetic (EM) wave can interact with molecules in the atmosphere when propagating through the atmosphere. The degree of interaction depends on the frequency of the EM wave, molecular resonances of molecules in the atmosphere, and the density of those molecules along the propagation path. The primary molecules of interest are oxygen (O_2) and water vapor (H_2O). Both behave as ideal gases in our frequency range and for our temperature and pressure conditions.

Oxygen comprises about 21% of the atmosphere. The O_2 molecule possesses a permanent magnetic moment, which leads to magnetic interactions with incident EM waves [5]. Coupling, and hence transfer of energy from the EM wave to the O_2 molecule, occurs very strongly at 50 – 70 GHz and 118 – 119 GHz. Thus, the atmosphere is a strong attenuator of EM signals in these two frequency bands.

Water vapor exists in the atmosphere, but the concentration of water vapor molecules (H_2O) varies greatly, both spatially and temporally. Water vapor is a polar molecule that exhibits an electric dipole, which strongly interacts with EM waves at 22 – 23 GHz and 183 – 184 GHz [5].

Nitrogen and other gases that comprise the atmosphere have relatively less impact on EM wave propagation in the frequency range of interest.

Recommendation ITU-R P.676-11, *Attenuation by Atmospheric Gases*, describes a line-by-line calculation method for the "specific attenuation" (i.e., attenuation per unit length) given in dB/km [6]. "Line-by-line" refers to specific molecular resonances (i.e., modes of absorption) of the oxygen and water vapor molecules.

---

[5] The Poynting vector is the cross product of the electric and magnetic fields, both of which decay in a lossy medium at a rate of $e^{-\alpha z}$. Thus, the power decays at a rate of $e^{-2\alpha z}$.

[6] For power ratio $\mathcal{S}(z)/\mathcal{S}_0$, we compute decibels as $10 * \log_{10}(e^{-\kappa_e z}) = (-\kappa_e z)(10 * \log_{10}(e)) = (-\kappa_e z)(4.3429)$. To convert from dB/m to dB/km, simply multiply by 1000 m/km.

The ITU-R model gives the specific attenuation for frequencies up to 1,000 GHz as a function of atmosphere temperature, pressure, and humidity. The model uses a summation of 44 individual resonance lines for oxygen and 35 resonance lines for water vapor. It also includes additional factors for the non-resonant Debye spectrum of oxygen below 10 GHz, pressure-induced nitrogen attenuation above 100 GHz, and a wet continuum to account for the excess water vapor-absorption that has been experimentally measured. This model, often referred to as the "millimeter-wave propagation model" was developed in the 1980's by Hans Liebe and his collaborators at the Institute of Telecommunications Sciences of the U.S. National Telecommunication and Information Administration [7, 8, 9]. For completeness, we describe the model and computation method.

Following the ITU publication, we denote the specific attenuation as *S*. For a frequency, *f*, and atmosphere conditions defined by temperature, dry air pressure, and water vapor pressure, the specific attenuation is calculated by:

$$S = 0.1820 * f * \left(\sum_{i=1}^{44} S_{o_i} F_{o_i} + \sum_{i=1}^{35} S_{w_i} F_{w_i} + N_D''(f)\right) \text{ (dB/km)}, \tag{21}$$

where *f* is the frequency in GHz, S_o is the strength of the i^{th} oxygen line, F_o is the line shape factor of the i^{th} oxygen line, S_w is the strength of the i^{th} water vapor line, F_w is the line shape factor of the i^{th} water vapor line, and $N_D''(f)$ is the dry continuum due to pressure-induced nitrogen absorption and the Debye spectrum.

Line strength is given by:

$$S_{o_i} = a_{1_i} * 10^{-7} * p * \theta^3 * exp\left(a_{2_i}(1-\theta)\right) \tag{22}$$

$$S_{w_i} = b_{1_i} * 10^{-1} * e * \theta^{3.5} * exp\left(b_{2_i}(1-\theta)\right), \tag{23}$$

where *p* is dry air pressure (hPa), *e* is water vapor partial pressure (hPa), $\theta = 300/T$, and *T* is temperature in Kelvin.

Line shape factor for the oxygen lines is given by:

$$F_{o_i} = \frac{f}{f_{o_i}}\left[\frac{\Delta f_{o_i} - \delta_{o_i} * \left(f_{o_i} - f\right)}{\left(f_{o_i} - f\right)^2 + \left(\Delta f_{o_i}\right)^2} + \frac{\Delta f_{o_i} - \delta_{o_i} * \left(f_{o_i} + f\right)}{\left(f_{o_i} + f\right)^2 + \left(\Delta f_{o_i}\right)^2}\right], \tag{24}$$

where Δf_{o_i} is the width of the line, given by

$$\Delta f_{o_i} = a_{3_i} * 10^{-4} * \left(p * \theta^{\left(0.8 - a_{4_i}\right)} + 1.1 * e * \theta\right). \tag{25}$$

This must be modified to account for Zeeman splitting of oxygen lines:

$$\Delta f_{o_i} = \sqrt{\left(\Delta f_{o_i}\right)^2 + 2.25 * 10^{-6}}. \tag{26}$$

The correction factor δ_{o_i} arises due to interference effects in oxygen lines and is given by

$$\delta_{o_i} = \left(a_{5_i} + a_{6_i} * \theta\right) * 10^{-4} * (p + e) * \theta^{0.8}. \tag{27}$$

Note that the oxygen shape factors include water vapor partial pressure.

Line shape factor for the water vapor lines is given by:

$$F_{w_i} = \frac{f}{f_{w_i}}\left[\frac{\Delta f_{w_i}}{\left(f_{w_i}-f\right)^2+\left(\Delta f_{w_i}\right)^2} + \frac{\Delta f_{w_i}}{\left(f_{w_i}+f\right)^2+\left(\Delta f_{w_i}\right)^2}\right], \tag{28}$$

where Δf_{w_i} is the width of the line, given by:

$$\Delta f_{w_i} = b_{3_i} * 10^{-4} * \left(p * \theta^{b_{4_i}} + b_{5_i} * e * \theta^{b_{6_i}}\right). \tag{29}$$

This must be modified to account for Doppler broadening of the water vapor lines:

$$\Delta f_{w_i} = 0.535 * \Delta f_{w_i} + \sqrt{0.217 * \left(\Delta f_{w_i}\right)^2 + \frac{2.1316*10^{-12}*f_{w_i}^{\ 2}}{\theta}}. \tag{30}$$

Note that the water vapor shape factors include dry air pressure.

The dry air continuum arises from the non-resonant Debye spectrum of oxygen below 10 GHz and a pressure-induced nitrogen attenuation above 100 GHz. It is given by:

$$N_D''(f) = f * p * \theta^2 * \left[\frac{6.14*10^{-5}}{d*\left(1+\left(\frac{f}{d}\right)^2\right)} + \frac{1.4*10^{-12}*p*\theta^{1.5}}{1+1.9*10^{-5}*f^{1.5}}\right], \tag{31}$$

where *d* is the width parameter for the Debye spectrum,

$$d = 5.6 * 10^{-4} * (p + e) * \theta^{0.8}. \tag{32}$$

Note that $N_D''(f)$ is a function of both dry air pressure and water vapor pressure.

Oxygen spectroscopic parameters $\{a_{1_i}, a_{2_i}, \ldots, a_{6_i}\}$ and water vapor spectroscopic parameters $\{b_{1_i}, b_{2_i}, \ldots, b_{6_i}\}$ are listed in Table 2 and Table 3 [6]. Given the temperature, dry air pressure, water vapor partial pressure for a parcel of air, the specific attenuation for a given frequency, *f*, can be calculated using this model.

Table 2. Spectroscopic Data for Oxygen Attenuation

f_o (GHz)	a_1	a_2	a_3	a_4	a_5	a_6
50.474214	0.975	9.651	6.690	0.0	2.566	6.850
50.987745	2.529	8.653	7.170	0.0	2.246	6.800
51.503360	6.193	7.709	7.640	0.0	1.947	6.729
52.021429	14.320	6.819	8.110	0.0	1.667	6.640
52.542418	31.240	5.983	8.580	0.0	1.388	6.526
53.066934	64.290	5.201	9.060	0.0	1.349	6.206
53.595775	124.600	4.474	9.550	0.0	2.227	5.085
54.130025	227.300	3.800	9.960	0.0	3.170	3.750
54.671180	389.700	3.182	10.370	0.0	3.558	2.654
55.221384	627.100	2.618	10.890	0.0	2.560	2.952
55.783815	945.300	2.109	11.340	0.0	–1.172	6.135
56.264774	543.400	0.014	17.030	0.0	3.525	–0.978
56.363399	1331.800	1.654	11.890	0.0	–2.378	6.547
56.968211	1746.600	1.255	12.230	0.0	–3.545	6.451
57.612486	2120.100	0.910	12.620	0.0	–5.416	6.056
58.323877	2363.700	0.621	12.950	0.0	–1.932	0.436
58.446588	1442.100	0.083	14.910	0.0	6.768	–1.273
59.164204	2379.900	0.387	13.530	0.0	–6.561	2.309
59.590983	2090.700	0.207	14.080	0.0	6.957	–0.776
60.306056	2103.400	0.207	14.150	0.0	–6.395	0.699
60.434778	2438.000	0.386	13.390	0.0	6.342	–2.825
61.150562	2479.500	0.621	12.920	0.0	1.014	–0.584
61.800158	2275.900	0.910	12.630	0.0	5.014	–6.619
62.411220	1915.400	1.255	12.170	0.0	3.029	–6.759
62.486253	1503.000	0.083	15.130	0.0	–4.499	0.844
62.997984	1490.200	1.654	11.740	0.0	1.856	–6.675
63.568526	1078.000	2.108	11.340	0.0	0.658	–6.139
64.127775	728.700	2.617	10.880	0.0	–3.036	–2.895
64.678910	461.300	3.181	10.380	0.0	–3.968	–2.590
65.224078	274.000	3.800	9.960	0.0	–3.528	–3.680
65.764779	153.000	4.473	9.550	0.0	–2.548	–5.002
66.302096	80.400	5.200	9.060	0.0	–1.660	–6.091
66.836834	39.800	5.982	8.580	0.0	–1.680	–6.393
67.369601	18.560	6.818	8.110	0.0	–1.956	–6.475
67.900868	8.172	7.708	7.640	0.0	–2.216	–6.545
68.431006	3.397	8.652	7.170	0.0	–2.492	–6.600
68.960312	1.334	9.650	6.690	0.0	–2.773	–6.650
118.750334	940.300	0.010	16.640	0.0	–0.439	0.079
368.498246	67.400	0.048	16.400	0.0	0.000	0.000
424.763020	637.700	0.044	16.400	0.0	0.000	0.000
487.249273	237.400	0.049	16.000	0.0	0.000	0.000
715.392902	98.100	0.145	16.000	0.0	0.000	0.000
773.839490	572.300	0.141	16.200	0.0	0.000	0.000
834.145546	183.100	0.145	14.700	0.0	0.000	0.000

Table 3. Spectroscopic Data for Water Vapor Attenuation

f_w (GHz)	b_1	b_2	b_3	b_4	b_5	b_6
22.235080	0.1079	2.144	26.38	0.76	5.087	1.00
67.803960	0.0011	8.732	28.58	0.69	4.930	0.82
119.995940	0.0007	8.353	29.48	0.70	4.780	0.79
183.310087	2.2730	0.668	29.06	0.77	5.022	0.85
321.225630	0.0470	6.179	24.04	0.67	4.398	0.54
325.152888	1.5140	1.541	28.23	0.64	4.893	0.74
336.227764	0.0010	9.825	26.93	0.69	4.740	0.61
380.197353	11.67	1.048	28.11	0.54	5.063	0.89
390.134508	0.0045	7.347	21.52	0.63	4.810	0.55
437.346667	0.0632	5.048	18.45	0.60	4.230	0.48
439.150807	0.9098	3.595	20.07	0.63	4.483	0.52
443.018343	0.1920	5.048	15.55	0.60	5.083	0.50
448.001085	10.41	1.405	25.64	0.66	5.028	0.67
470.888999	0.3254	3.597	21.34	0.66	4.506	0.65
474.689092	1.260	2.379	23.20	0.65	4.804	0.64
488.490108	0.2529	2.852	25.86	0.69	5.201	0.72
503.568532	0.0372	6.731	16.12	0.61	3.980	0.43
504.482692	0.0124	6.731	16.12	0.61	4.010	0.45
547.676440	0.9785	0.158	26.00	0.70	4.500	1.00
552.020960	0.1840	0.158	26.00	0.70	4.500	1.00
556.935985	497.0	0.159	30.86	0.69	4.552	1.00
620.700807	5.015	2.391	24.38	0.71	4.856	0.68
645.766085	0.0067	8.633	18.00	0.60	4.000	0.50
658.005280	0.2732	7.816	32.10	0.69	4.140	1.00
752.033113	243.4	0.396	30.86	0.68	4.352	0.84
841.051732	0.0134	8.177	15.90	0.33	5.760	0.45
859.965698	0.1325	8.055	30.60	0.68	4.090	0.84
899.303175	0.0547	7.914	29.85	0.68	4.530	0.90
902.611085	0.0386	8.429	28.65	0.70	5.100	0.95
906.205957	0.1836	5.110	24.08	0.70	4.700	0.53
916.171582	8.400	1.441	26.73	0.70	5.150	0.78
923.112692	0.0079	10.293	29.00	0.70	5.000	0.80
970.315022	9.009	1.919	25.50	0.64	4.940	0.67
987.926764	134.6	0.257	29.85	0.68	4.550	0.90
1780.000000	17506.0	0.952	196.3	2.00	24.15	5.00

3.2.3 Standard Atmosphere Model

The Standard Atmosphere model provides a reasonable starting point to estimate clear-day atmosphere conditions (i.e., temperature, pressure, and water vapor partial pressure) as a function of altitude, which can then be used to estimate clear-day specific attenuation [10, 11]. The Standard Atmosphere model is an idealized, steady-state representation of the earth's atmosphere from the surface to ~100 km as it is assumed to exist in a period of moderate solar activity. This model is time-invariant and does not represent any single ground site location. The model was intended to represent mean global and annual mid-latitude (45 degree North) temperature, pressure, and density conditions. It does not include hydrometers (i.e., clouds or precipitation).

3.2.3.1 Temperature

Figure 2 presents the atmospheric temperature profile as a function of altitude for the Standard Atmosphere model from sea level up to 500 km. Below 85 km, the model is empirical, being based upon temperature measurements by radiosondes, rocket-sondes, rockets, and satellites. Also below 85 km, the model provides a linearly segmented temperature-height profile. Further, below 85 km, the model assumes ***hydrostatic equilibrium***, in that air is treated as a homogeneous mixture of the several constituent gases. Various atmosphere layers are indicated.

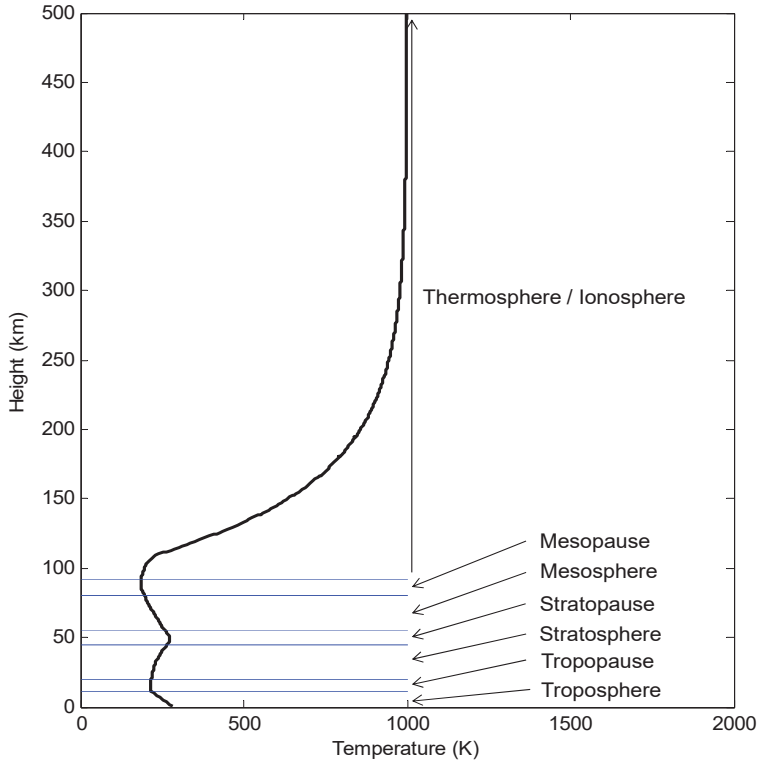

Figure 2. Plot of Temperature as a Function of Altitude for the Standard Atmosphere Model (up to 500 km)

Figure 3 presents the temperature profile for 0 – 100 km. Below 80 km, the atmosphere can be modeled as well-mixed (homogenous). Except for water vapor variations, the relative composition of the atmosphere is essentially constant. The troposphere (up to about 11 km) and tropopause (from 11 km to 20 km) contain approximately 75% of the total mass of the atmosphere. The stratosphere (from 20 km to about 47 km) and stratopause (from 47 km to about 51 km) contain approximately 24% of the total mass of the atmosphere. Approximately 90% of the water vapor in the atmosphere is found below 5 km.

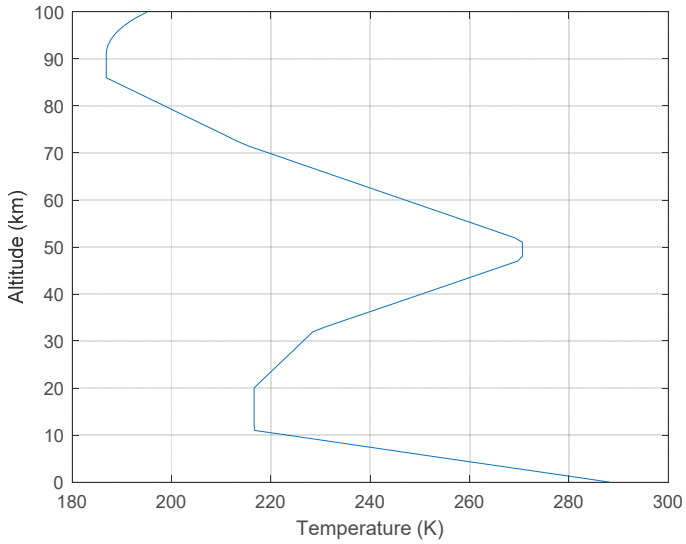

Figure 3. Plot of Temperature as a Function of Altitude for the Standard Atmosphere Model (up to 100 km)

The ratio of the change in temperature to the change in altitude (dT/dh) is generally called the "lapse rate". The Standard Atmosphere model assumes a linear lapse rate (dT/dh) for each of the seven layers up through 91 km above sea level. For example, the lapse rate in the troposphere (i.e., the lowest level) is -6.5 K/km[7]. The temperature is assumed constant in the tropopause, stratopause, and mesopause. The temperature increases in the stratosphere. The Standard Atmosphere temperature at sea level is defined to be T_0 = 15 °C (288.15 K).

3.2.3.2 Dry Atmosphere Pressure

The Standard Atmosphere dry air pressure at sea level is defined to be P_{d_0}= 1013.25 hPa. Figure 4 presents the dry air pressure as a function of altitude for the Standard Atmosphere model. Figure 4 is plotted with a logarithmic abscissa, which illustrates the exponential decrease of pressure with increasing altitude. The dry air pressure approximately follows:

$$P_d(h) = P_{d_0}\exp\left(\frac{-h}{7.7\ km}\right) \quad \text{(hPa)}, \tag{33}$$

although the Standard Atmosphere model is a bit more detailed.

[7] Since we are discussing a change in the temperature profile, we note that -6.5 K/m is equivalent to -6.5 °C/m.

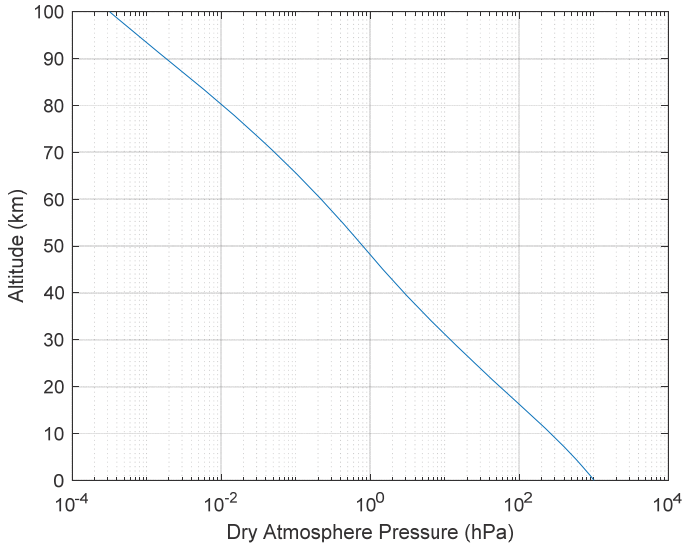

Figure 4. Plot of Dry Air Pressure as a Function of Altitude for the Standard Atmosphere Model (up to 100 km)

At normal and low densities, the behavior of air can be modeled using the ideal gas equation of state with good accuracy. The ideal gas equation of state can be expressed as:

$$P_d = \rho_d R_d T, \tag{34}$$

where P_d is the dry air pressure in units of Pa, ρ_d is the density in units of kg/m^3, R_d is the gas constant in units of J/(kg·K), and T is the temperature in Kelvin. Given that the gas constant for dry air is R_d = 287 J/(kg·K) [12], the density of dry air can be estimated using the ideal gas equation of state:

$$\rho_d = \frac{P_d}{R_d \, \mathrm{T}} \text{ (kg/m}^3\text{)}, \tag{35}$$

which is ρ_{d_0} = 1.225 kg/m^3 at sea level.

3.2.3.3 Moist Atmosphere Pressure

Now, let's add moisture to our dry atmosphere. For the Standard Atmosphere model, water vapor density at sea level is defined as ρ_{v_0} = 0.0075 kg/m^3 [10]. Water vapor density as a function of altitude, h, is given by:

$$\rho_v(h) = \rho_{v_0} exp\left(\frac{-h}{h_0}\right) \text{ (kg/m}^3\text{)}, \tag{36}$$

where the scale height is defined as h_0 = 2 km. Water vapor pressure as a function altitude, denoted here as $e(h)$, can be calculated using the ideal gas law:

$$e(h) = \rho_v(h) * R_v * T(h), \tag{37}$$

where the gas constant for water vapor (steam) is R_v = 461.51 J/(kg·K) [12]. For the Standard Atmosphere model, the water vapor mixing ratio decreases with increasing altitude up to the altitude at which:

$$\frac{e(h)}{P_d(h)} = 2e-6. \tag{38}$$

Above this altitude, the mixing ratio is assumed to be constant (i.e., it does not decrease beyond 2e-6). The reason for this assumption is not explained in the reference. Figure 5 shows the water vapor partial pressure as a function of altitude for the Standard Atmosphere model. There is a change in the slope of the water vapor pressure at about h = 23 km as a result of the assumption on the mixing ratio. This is far above the troposphere, so water vapor is inconsequential to our W/V-band models.

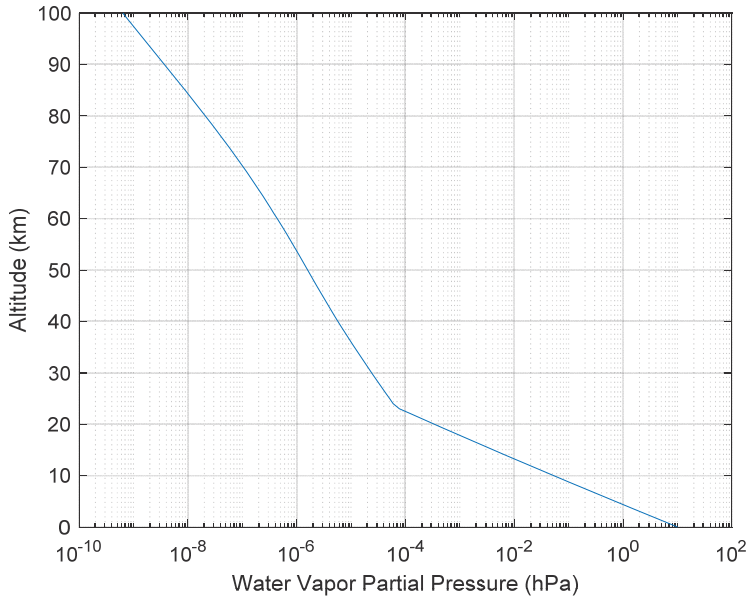

Figure 5. Plot of Water Vapor Partial Pressure as a Function of Altitude for the Standard Atmosphere Model (up to 100 km)

At sea level, the partial pressure of water vapor for the Standard Atmosphere model is e_0 = 9.97 hPa. The total atmospheric (barometric) pressure is given as:

$$P_t(h) = P_d(h) + e(h). \tag{39}$$

Thus, the total atmospheric pressure at sea level is P_{t_0} = 1023.22 hPa.

3.2.3.4 Relative Humidity

The relative humidity, ϕ, is the ratio of the mole fraction of water vapor in an air mixture to the mole fraction of water vapor in a saturated mixture at the same temperature and total pressure [13]. Since we can assume water vapor behaves as an ideal gas, this definition reduces to the ratio of the partial pressure of water vapor, e, to the saturation pressure of water vapor at the same temperature, denoted here as e_s. Expressing as a percentage:

$$\phi = 100\left(\frac{e}{e_s}\right)\%. \tag{40}$$

At temperatures above freezing ($T > 0$ °C), the saturation pressure and saturation temperature represent the equilibrium between the rate of condensation of vapor and the rate of evaporation of liquid for the unit volume. If the temperature increases, then the saturation pressure increases, meaning that more water vapor can exist in the unit volume (hence, liquid water droplets evaporate). Likewise, if the temperature decreases, then more vapor condenses into liquid droplets in the unit volume (hence, the water vapor pressure decreases).

At temperatures below freezing ($T < 0$ °C), the saturation pressure and saturation temperature represent the equilibrium between the rate of deposition of vapor and the rate of sublimation of solids (ice or snow) for the unit volume. If the temperature increases, then the saturation pressure increases, meaning that more water vapor can exist in the unit volume (hence, ice crystals sublimate). Likewise, if the temperature decreases, then more vapor changes into ice crystals (process known as deposition) in the unit volume (hence, the water vapor pressure decreases).

The Clausius-Clapeyron equation expresses the relation between the saturation pressure and temperature for water vapor and liquid water [14, 15]:

$$\frac{1}{e_s}\frac{de_s}{dT} = \frac{L_v}{R_v T^2}, \tag{41}$$

where L_v is the enthalpy of vaporization. Likewise, the relation between the saturation pressure and temperature for water vapor and solid water (i.e., ice) is given by:

$$\frac{1}{e_{si}}\frac{de_{si}}{dT} = \frac{L_s}{R_v T^2}, \tag{42}$$

where L_s is the enthalpy of sublimation. If we assume that L_v and L_s are constant, then the solutions are:

$$e_s = e_{s0} \cdot \exp\left(\frac{L_v}{R_v T_0}\right) \cdot \exp\left(\frac{-L_v}{R_v T}\right) \quad \text{(hPa)} \tag{43}$$

$$e_{si} = e_{s0} \cdot \exp\left(\frac{L_s}{R_v T_0}\right) \cdot \exp\left(\frac{-L_s}{R_v T}\right) \quad \text{(hPa)}, \tag{44}$$

where T_0 = 273.15 K, e_{s0} = 6.11 hPa, R_v = 461.51 J/(kg·K), and L_v = 2.5e6 J/kg or L_s = 2.834e6 J/kg. Solutions for e_s that account for the small temperature dependence of L_v and L_s are:

$$e_s = e_{s0} \cdot \exp\left[6808\left(\frac{1}{T_0} - \frac{1}{T}\right) - 5.09 \cdot ln\left(\frac{T}{T_0}\right)\right] \quad \text{(hPa)} \tag{45}$$

$$e_{si} = e_{s0} \cdot \exp\left[6293\left(\frac{1}{T_0} - \frac{1}{T}\right) - 0.555 \cdot ln\left(\frac{T}{T_0}\right)\right] \text{ (hPa).} \quad (46)$$

Figure 6 plots e_s as a function of temperature. A logarithmic scale is used, which makes the shape of the curve appear somewhat different than commonly found in the literature. The function for e_s can be extended below 0 °C, because water can remain in the liquid state at lower temperatures as a super-cooled liquid. Along e_s, vapor and liquid are in equilibrium. Figure 6 also shows e_{si}. Along e_{si}, vapor and ice are in equilibrium. The equilibrium line for vapor and ice lies below the equilibrium line for vapor and super-cooled liquid, $e_s > e_{si}$. Saturation pressures can also be interpolated from thermodynamic tables [16, 17]. Values from thermodynamic tables are included in Figure 6. Below $T = 0$ °C, the thermodynamic tables follow e_{si} (as opposed to e_s).

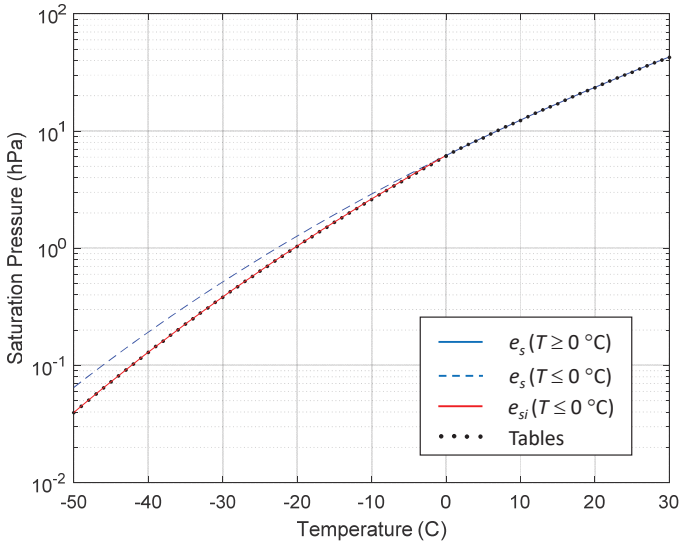

Figure 6. Saturation Pressure of Water Vapor as Function of Temperature

For the Standard Atmosphere temperature at sea level, $T_0 = 15$ °C, the saturation pressure is $e_s = 17.051$ hPa. Therefore, the relative humidity for the Standard Atmosphere model at sea level is:

$$\phi_0 = 100\left(\frac{9.97\ hPa}{17.051\ hPa}\right)\ \% = 58.47\ \%. \quad (47)$$

3.2.3.5 Integrated Precipitable Water Vapor

We can use the water vapor density profile to compute the amount of water vapor contained in a vertical column with unit cross-section area:

$$M_v = \int_{h_{min}}^{h_{max}} \rho_v(h)\, dh \ \text{(kg/m}^2\text{)}, \quad (48)$$

where $h_{\min}$ defines the starting altitude and $h_{\max}$ defines the ending altitude relative to sea level. The integral can be numerically evaluated by applying the trapezoid rule,

$$M_v = \sum_{i=1}^{N-1} \left(\frac{\rho_{v_i} + \rho_{v_{i+1}}}{2} \Delta h \right) \text{ (kg/m}^2\text{)}, \quad (49)$$

where the atmosphere is essentially divided into N layers of thickness Δh. For uniform layer thickness,

$$M_v = \Delta h * \sum_{i=1}^{N-1} \left(\frac{\rho_{v_i} + \rho_{v_{i+1}}}{2} \right) \text{ (kg/m}^2\text{)}. \quad (50)$$

Using the Standard Atmosphere model, we find M_v = 15 kg/m^2 = 15 mm, where 1 kg/m^2 = 1 mm of precipitable water. This is also referred to as "atmosphere water vapor", "total column water vapor", "total mass of water vapor", and "total precipitable water".

3.2.3.6 Dew Point

The dew point is defined as the temperature to which a parcel of air must be cooled at constant pressure for it to become saturated. The dew point is mentioned here for completeness, and to clarify that dew point cannot be used to determine the lifted condensation level (discussed later), because the lifted condensation level assumes adiabatic expansion – thus, the pressure is not constant.

3.2.4 Specific Attenuation, Optical Thickness, and Opacity

Values from the Standard Atmosphere model (i.e., temperature, dry air partial pressure, and water vapor partial pressure) can be used to compute specific attenuation at a given frequency and altitude. To illustrate, Figure 7 plots the specific attenuation (dB/km) as a function of frequency (0 – 1000 GHz) for three different altitudes (0 m, 1000 m, and 10000 m). At the far left, we can see a resonance corresponding to the water vapor absorption band at 22 – 23 GHz. Next, we can see the oxygen absorption band at 50 – 70 GHz. Specific attenuation continues to increase with increasing frequency. We can also see that at higher altitudes, the specific attenuation decreases. This is because the air molecules are less dense with higher altitude. In fact, some resonant peaks are not observable at lower altitudes because the "pressure spreading" effects at lower altitude obscures the weaker resonant peaks.

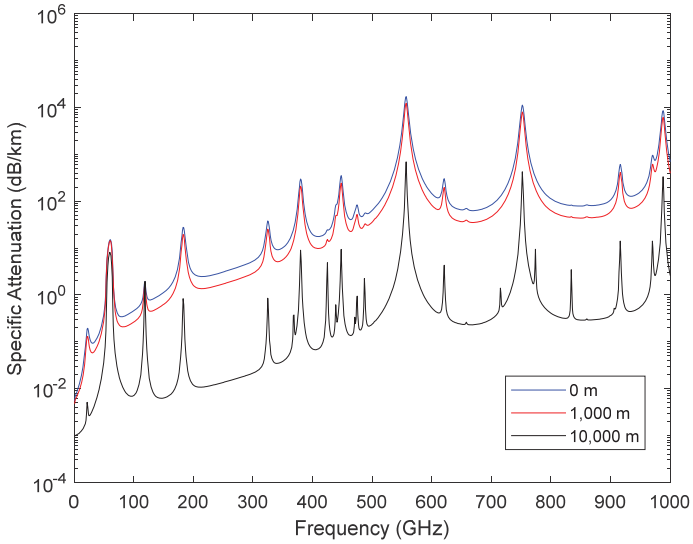

Figure 7. Specific Attenuation as a Function of Frequency for Various Altitudes Using the Standard Atmosphere Model

Figure 8 plots the specific attenuation as a function of altitude (0 – 80 km) at a single frequency, 72.5 GHz. At sea level (0 m), the specific attenuation is 0.4050 dB/km. At 10 km, the specific attenuation is 0.0274 dB/km. The specific attenuation rolls off very quickly with increasing altitude. As we see in Figure 7, this is true for the specific attenuation at any frequency in the given bandwidth.

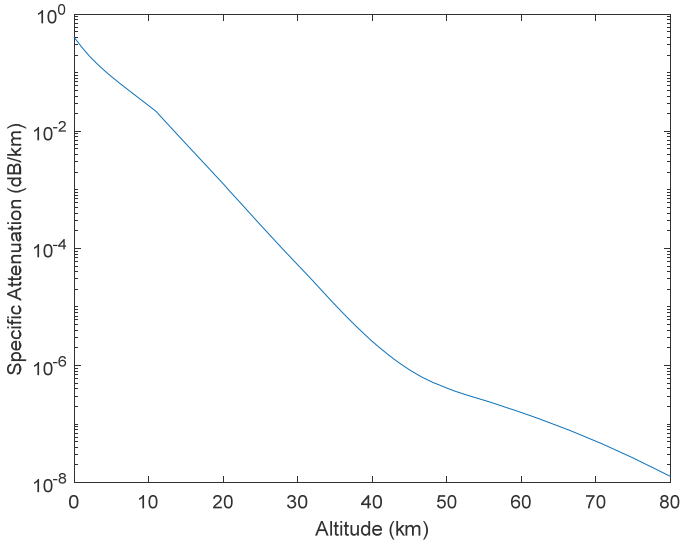

Figure 8. Specific Attenuation as a Function of Altitude for f = 72.5 GHz Using the Standard Atmosphere Model

We can use the specific attenuation to calculate the total attenuation of an EM wave propagating vertically through the atmosphere (i.e., space-to-ground). To illustrate, let's consider the atmosphere as consisting of many horizontal layers (i.e., stratified). Figure 9 shows a single layer between arbitrary altitudes h_0 and h_1 [18]. The angle of arrival of the EM wave, denoted here as θ, is measured from the vertical (dashed) line. We define the ***oblique optical thickness*** of this single layer as:

$$\tau(h_0, h_1) = \sec(\theta) \int_{h_0}^{h_1} S(h)\, dh \text{ (dB)}, \tag{51}$$

where $\sec(\theta)$ is the secant of the angle of arrival, and $S(h)$ is the specific attenuation as a function of altitude expressed in units of dB per unit length as given in Eq. (21). If the angle of arrival is $\theta = 0$, this becomes the ***zenith optical thickness***:

$$\tau_0(h_0, h_1) = \int_{h_0}^{h_1} S(h)\, dh \text{ (dB)}. \tag{52}$$

If τ includes the propagation path from the ground terminal ($h_0 = h_{min}$) to the top of the atmosphere ($h_1 = h_{max}$), then it is called the ***opacity***.

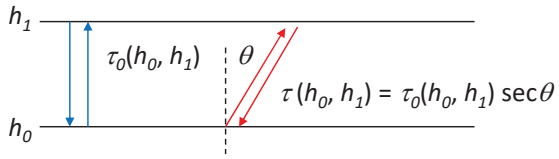

Figure 9. Illustration of Optical Thickness for a Single Layer of Atmosphere

Let's look at an example to compute the opacity. Let's assume the atmosphere is modeled with seven layers, separated by 8 distinct elevation (or altitude) points as shown in Figure 10. For illustration, we assume Δh = 10 km, f = 72.5 GHz, and θ = 0 degrees (thus, we are computing the ***zenith opacity***). Using these parameters and the Standard Atmosphere model, we compute the values given in Table 4. Note that MATLAB does not permit a "zero" index, so we cannot have an $h(0)$ term in our script; so $h(1) = h_0 = h_{min} = 0$ m.

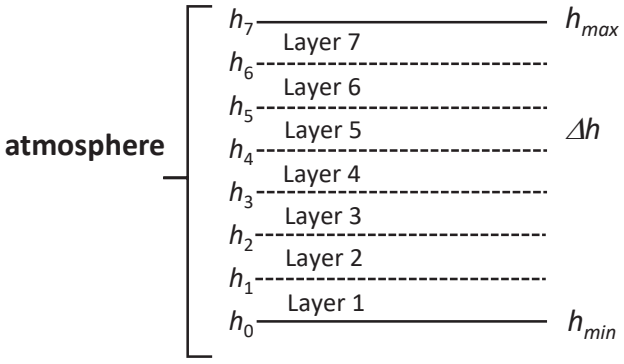

Figure 10. Illustration for Computing Atmosphere Opacity

Table 4. Standard Atmosphere and Specific Attenuation Values for Opacity Calculation

Altitude (km)	Temp (K)	Pressure (hPa)	Water Vapor Pressure (hPa)	Specific Attenuation (dB/km)
h(1) = 0	T(1) = 288.1500	1013.3	9.9729	S(1) = 0.4050
h(2) = 10	T(2) = 223.2521	265.0	0.0521	S(2) = 0.0274
h(3) = 20	T(3) = 216.6500	55.3	3.4042e-04	S(3) = 0.0013
h(4) = 30	T(4) = 226.5091	12.0	2.3941e-05	S(4) = 5.2459e-05
h(5) = 40	T(5) = 250.3496	2.9	5.7430e-06	S(5) = 2.5940e-06
h(6) = 50	T(6) = 270.6500	0.8	1.5956e-06	S(6) = 4.1263e-07
h(7) = 60	T(7) = 247.0209	0.2	4.3919e-07	S(7) = 1.5778e-07
h(8) = 70	T(8) = 219.5848	0.05	1.0442e-07	S(8) = 5.1188e-08

Figure 11 plots the values of specific attenuation as a function of altitude. It is clear that at h_{max} = 70 km, the value of specific attenuation has become relatively inconsequential. To find the opacity, we evaluate the integral:

$$\tau_0(h_0, h_7) = \int_{h_0}^{h_7} S(h)\, dh \text{ (dB)}, \tag{53}$$

using the trapezoid rule:

$$\tau = \sec(\theta) \left[\sum_{i=1}^{7} \left(\frac{S_i + S_{i+1}}{2}\right)\right] \Delta h \quad \text{(dB)}, \tag{54}$$

where we can factor-out sec(θ)Δh, since it is constant. For this example, τ ~2.3 dB. Note that opacity is a positive dB quantity as calculated. However, opacity reduces signal strength, so it is a ***link loss***. Therefore, the loss due to opacity is:

$$L_{atm} = -\tau \text{ (dB)}. \tag{55}$$

We can improve the calculation of the atmosphere opacity by decreasing the layer thickness. At Δh = 100 m, the opacity at 72.5 GHz is calculated as 1.3085 dB (the exact value). As reference, the exact opacity at 82.5 GHz is calculated as 0.8008 dB. Figure 12 presents the atmosphere opacity (starting from sea level) as a function of frequency for the Standard Atmosphere model.

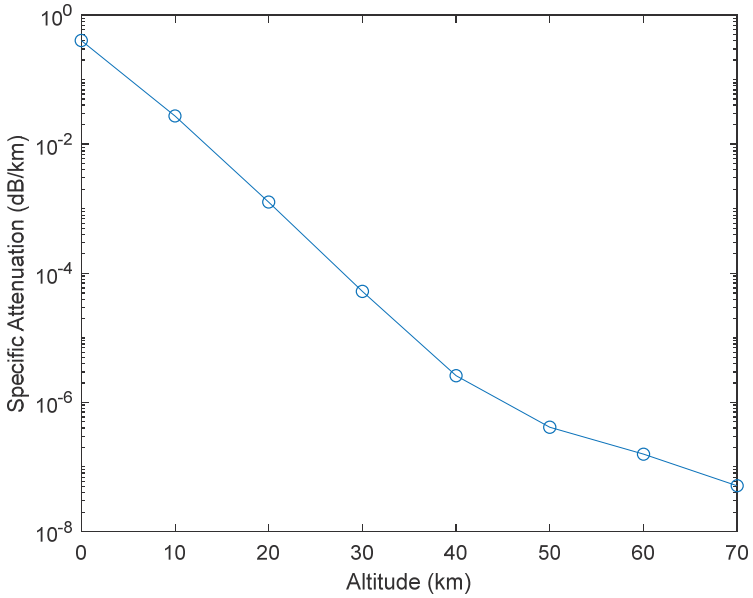

Figure 11. Specific Attenuation Values as a Function of Altitude for Opacity Calculation

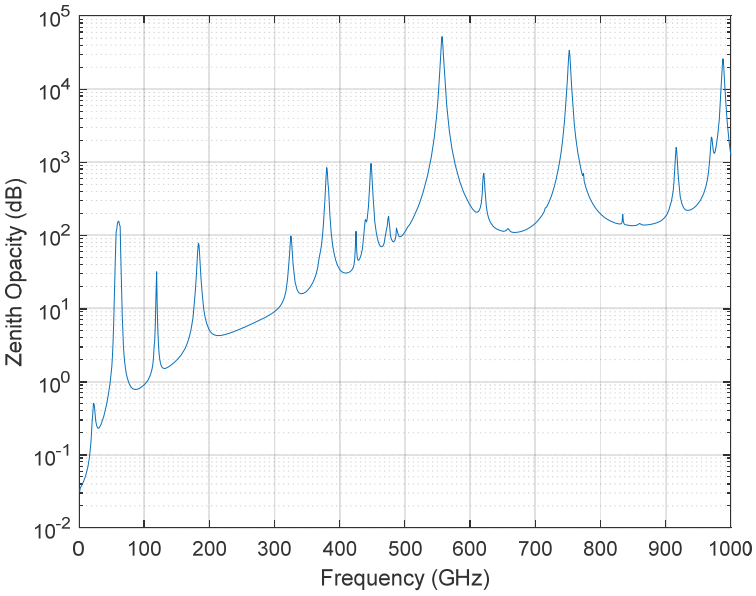

Figure 12. Zenith Opacity as a Function of Frequency Using the Standard Atmosphere Model

Now, let's examine the effect of varying moisture content on zenith opacity. The effect of humidity can be observed by changing the value of the relative humidity from the standard (58.47%) and computing the corresponding ρ_{v0} for the density profile. First, we find the sea level partial pressure of water vapor as a function of relative humidity from Eq. (40):

$$e_0 = \left(\frac{\phi}{100}\right) * e_s(T_0) \ \text{(hPa)}. \tag{56}$$

The corresponding water vapor density can be computed from the ideal gas law:

$$\rho_{v0} = \frac{e_0}{R_v T_0} \ \left(\frac{g}{m^3}\right). \tag{57}$$

We still use the temperature and dry air pressure profiles from the Standard Atmosphere model, but the water vapor pressure profile is computed from the ideal gas law:

$$e(h) = \frac{\rho_v(h) * T(h)}{216.68} \text{(hPa)}, \tag{58}$$

and the water vapor density profile is computed from:

$$\rho_v(h) = \rho_{v0} \exp\left(\frac{-h}{h_0}\right), \tag{59}$$

where ρ_{v0} is computed from Eq. (57) and the scale height remains as h_0 = 2 km. Figure 13 plots the zenith opacity as a function of frequency for several values of (sea level) relative humidity (RH). It is apparent that as the moisture content decreases, so does the opacity, except at frequency bands dominated by oxygen absorption (i.e., 50-70 GHz and 118-119 GHz).

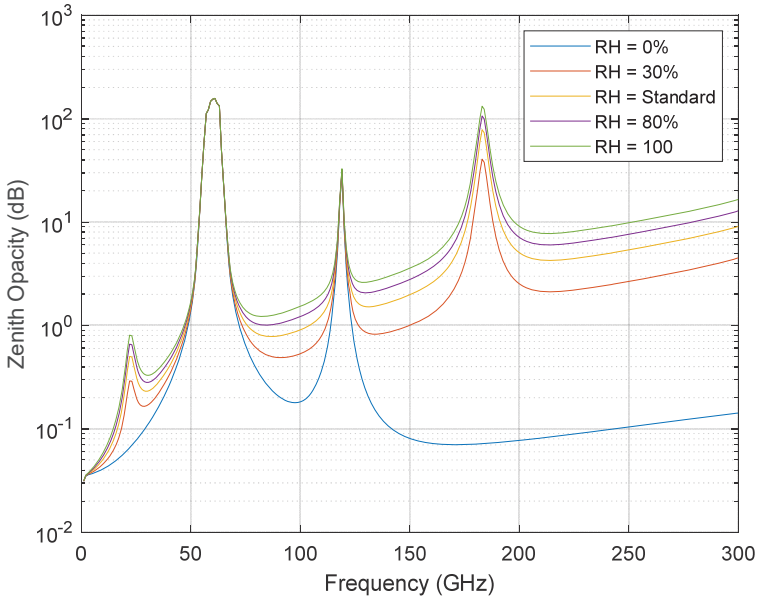

Figure 13. Zenith Opacity for Various Values of Relative Humidity (at Sea Level) Computed Using the Standard Atmosphere Model

In this section, optical thickness and opacity were described using the Standard Atmosphere model, which provided a convenient source for atmospheric temperature, dry air pressure, and water vapor partial pressure profiles. The specific attenuation, optical thickness, and opacity can also be calculated using experimentally measured profiles of temperature and pressure to yield estimates for a specific location and time (i.e., using radiosonde data). The key limitation of our modeling ability is the uncertainty of the parameters along the propagation path. As observed in our 7-layer example, coarse knowledge (i.e., widely separated data points) can result in significant error.

3.2.4.1 Radiosonde Analysis

Radiosonde measurements are performed twice daily across the world to inform weather models. Measurements are made at 0000 UTC[8] and 1200 UTC, so the local time varies with time zone. Radiosonde data files can be retrieved from online archives, such as http://weather.uwyo.edu/upperair/sounding.html. Radiosonde measurements provide better representation of the clear-day conditions than the Standard Atmosphere model. Radiosonde measurements do not provide indications of or data regarding clouds or precipitation. Data begins at the local measurement site surface level and typically go up to at least 10000 m. Often data is reported up to 30000 m, but this varies. Radiosonde measurements typically take an hour to complete, depending on the rate of ascension – thus, it is not an instantaneous profile, but rather one measured over time. It is unknown whether measurements use a fixed sampling rate (Hz). However, the altitudes at which measurements are taken varies (non-uniform spatial sampling). Radiosonde data is easily interpolated to create a uniformly spaced profile.

Figure 14 presents the first few lines from a radiosonde data file. Data was measured on July 31, 2014 at 0000 UTC in Albuquerque, NM, which is equivalent to 6 PM, July 30, 2014 local time. The surface altitude was 1619 m above sea level. Reported data for the sonding included pressure (total atmospheric (barometric) pressure), altitude, temperature, dew point, and relative humidity – which is sufficient for calculating the specific attenuation and opacity. This particular data file included data up to 34573 m with 131 non-uniformly spaced samples.

Station identifier: ABQ
Station number: 72365
Observation time: 140731/0000 <- July 31, 2014, 00:00 UTC
Station latitude: 35.04
Station longitude: -106.62
Station elevation: 1619.0

PRES	HGHT	TEMP	DWPT	RELH	MIXR	DRCT	SKNT	THTA	THTE	THTV	
hPa	m	C	C	%	g/kg	deg	knot	K	K	K	
1000.0	51										
925.0	754										
850.0	1505										
839.0	1619	31.2	10.2	27	9.39	200	3	320.0	350.3	321.8	
829.0	1726	29.8	9.8	29	9.25	233	4	319.6	349.4	321.4	Δh = 107 m
819.5	1829	28.6	9.0	29	8.85	265	4	319.4	347.9	321.1	

Figure 14. First Few Lines from a Radiosonde Data File

[8] Universal Coordinated Time

Data from a radiosonde file can be read into Matlab for analysis. The Standard Atmosphere model can be evaluated at each point in the radiosonde height vector. Figure 15 compares the measured radiosonde data for July 31, 2014 at 0000 UTC in Albuquerque, NM to the computed Standard Atmosphere model values. The temperature near the surface is higher, as expected for a summer day, but the lapse rate is similar to that of the standard model. The pressure curves are very similar. There is a lot of variation of the water vapor partial pressure, but the overall trend follows the Standard Atmosphere model.

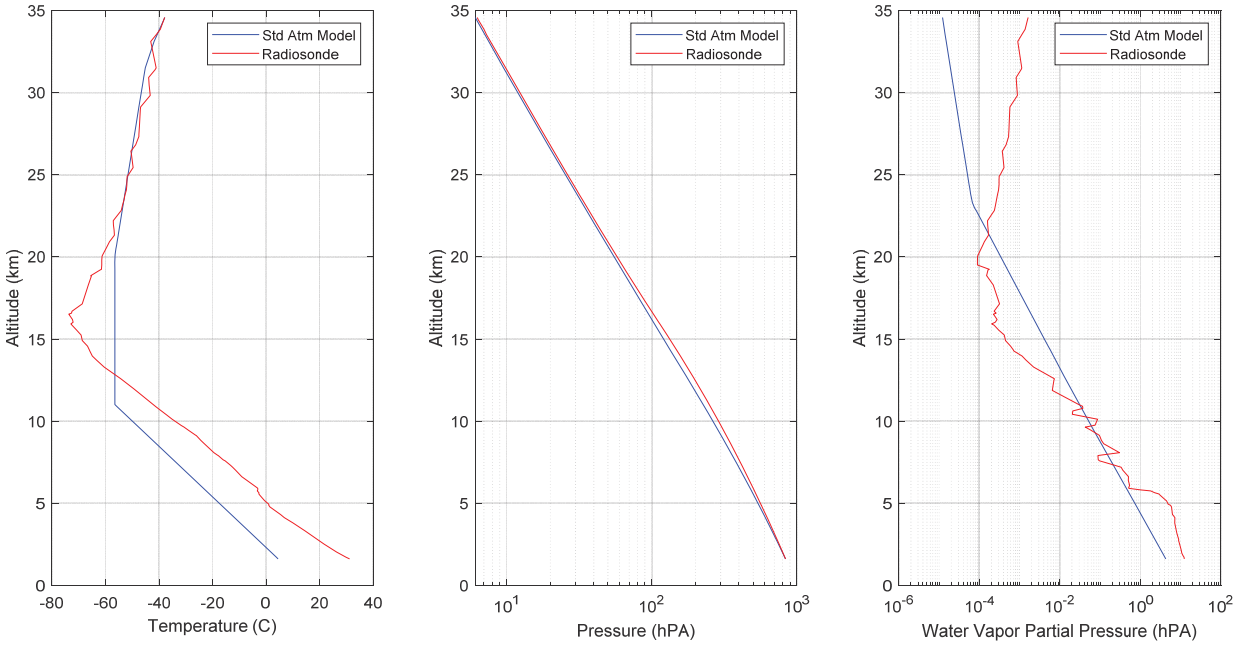

Figure 15. Comparison of Radiosonde Measurements to Standard Atmosphere Model

The specific attenuation was computed for f_1 = 72.5 GHz and f_2 = 82.5 GHz using both the radiosonde and Standard Atmosphere profiles. Then, the opacity was calculated as previously described. Table 5 shows the computed values. Note that the starting altitude was 1620 m, as opposed to sea level. Opacity was calculated from the surface to the highest altitude in the radiosonde data file (i.e., 1620 m – 34520 m). Additionally, the opacity was calculated from the surface to the troposphere (i.e., 1620 m – 10020 m) to assess the potential error that would occur if the data were truncated, which commonly occurs in radiosonde data files. The values computed using the radiosonde profile were significantly higher than for the Standard Atmosphere model, which is reasonable given the higher temperature and moisture content of the measured atmosphere profile. Finally, note that the error introduced from truncation to ~10 km was only about 0.10 dB at 72.5 GHz, and only about 0.04 dB at 82.5 GHz.

Table 5. Comparison of Opacity Calculated with Radiosonde Profile to Standard Atmosphere Model (July 31, 2014 at 0000 UTC in Albuquerque, NM)

f	Standard Atmosphere Model			Radiosonde Profile		
	1620 – 34520 m	1620 – 10020 m	Error	1620 – 34520 m	1620 – 10020 m	Error
72.5 GHz	0.82 dB	0.73 dB	0.09	1.09 dB	0.98 dB	0.11
82.5 GHz	0.42 dB	0.39 dB	0.03	0.83 dB	0.79 dB	0.04

Figure 16 presents the zenith opacity calculated for an entire year of radiosonde measurements, also in Albuquerque, NM. Measurements are from 2019. Calculations included data from the surface (1620 m) to 20000 m and interpolated to a uniform distance, Δh = 100 m. Figure 16 demonstrates the variation of opacity resulting from radiosonde profiles. This does not include effects due to clouds or precipitation. Two red vertical lines are superimposed on each plot, which indicate the normal start and end of the monsoon season for the desert southwest region (Jun 15 - Sep 30), which typically exhibits higher levels of atmospheric moisture relative to the rest of the year. Also shown is the opacity calculated using the Standard Atmosphere model for the same altitude vector (1620-20000 m). Calculated values are remarkably similar, except during the monsoon season. Table 6 presents the annual mean values, standard deviation, and maximum values of opacity for 72.5 GHz and 82.5 GHz.

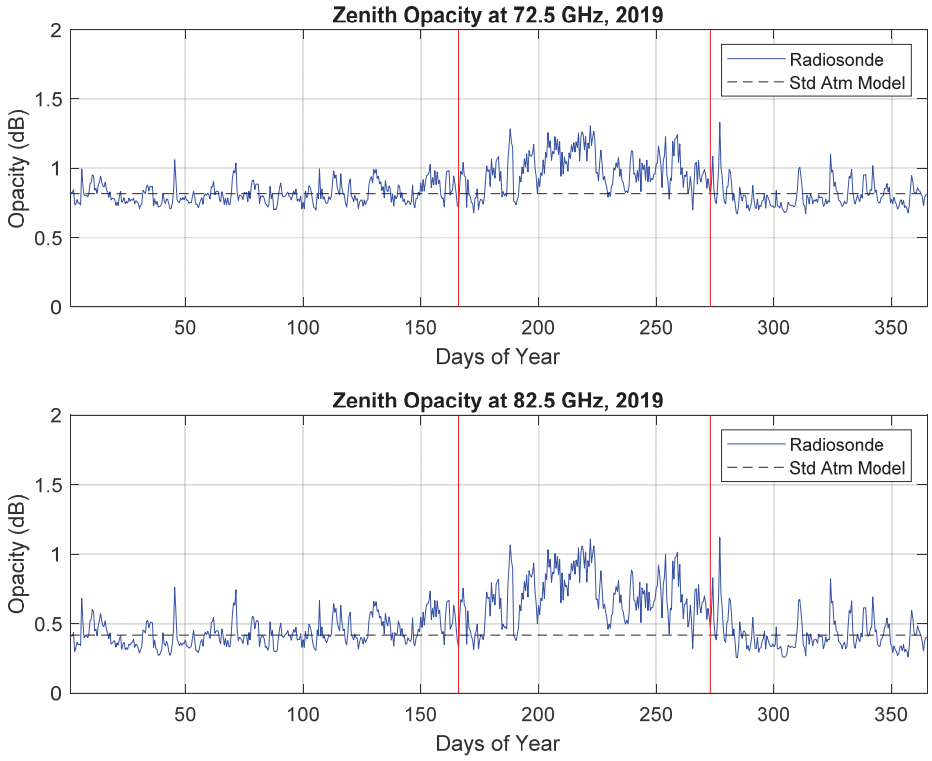

Figure 16. Comparison of Zenith Opacity Computed using Radiosonde Data and the Standard Atmosphere Model for Albuquerque NM During 2019

Table 6. Mean and Standard Deviation of Zenith Opacity Computed using Radiosonde Data for Albuquerque NM During 2019

f	Standard Atmosphere (1620 – 20000 m)	Radiosonde (1620 – 20000 m)		
		Mean	Std Dev	Max
72.5 GHz	0.82 dB	0.86 dB	0.13	1.33 dB
82.5 GHz	0.42 dB	0.51 dB	0.18	1.12 dB

3.2.4.2 Propagation Path Length

Finally, we note that the horizontal layer model for the atmosphere breaks down with increasing angle of arrival, because $\sec(\theta)\Delta h \to \infty$ as $\theta \to 90°$ whereas the earth is actually curved[9]. Thus, the model will overestimate the optical thickness or opacity. Nevertheless, for horizontal propagation paths (or any propagation path in general) of distance R, the total attenuation (i.e., optical thickness) along the propagation path can be determined by calculating:

$$\tau(0,R) = \int_0^R \kappa_e(r)\, dr \ \text{(dB)}, \tag{60}$$

where $\kappa_e(r)$ is the extinction coefficient (dB per unit length) along the propagation path, including effects from gaseous absorption, cloud absorption, precipitation absorption, and scattering:

$$\kappa_e = \kappa_{a_g} + \kappa_{a_{cl}} + \kappa_{a_p} + \kappa_s \ \text{(dB/km)}. \tag{61}$$

Note that the distance through a cloud or through rain can differ from the overall path length, in which case we would need to identify and effective path length for those conditions:

$$\tau(0,R) = \int_0^R \kappa_{a_g}(r)\, dr + \int_0^{R_{cl}} \kappa_{a_{cl}}(r)\, dr + \int_0^{R_{rain}} \kappa_{a_p}(r)\, dr + \int_0^{R_{rain}} \kappa_s(r)\, dr \ \text{(dB)}, \tag{62}$$

where R_{cl} is the effective propagation distance through a cloud and R_{rain} is the effective propagation distance through rain.

3.2.5 Clouds

Discussion so far has been limited to clear-day conditions, where absorption is due only to atmospheric gases and water vapor. In general, the interaction of EM radiation with hydrometeors (such as those in clouds, fog, snow, and rain) is different in nature and may involve both absorption and scattering, which together are called extinction. The ***cloud volume extinction coefficient*** is governed by the density, shape, size distribution, and dielectric properties of the particles (i.e., hydrometeors) contained in the volume [19]. First, we will discuss absorption and scattering from a single particle, and then extend those results to a volume containing many particles. The particles are assumed to be randomly distributed throughout the volume. Therefore, contributions of individual particles can be summed assuming an incoherent process (i.e., superposition). We also assume that particles are spherical.

[9] Therefore, the path through the atmosphere is finite.

3.2.5.1 Single Particle Absorption and Scattering

3.2.5.1.1 Mie Solution and Rayleigh Approximation

Consider a differential volume containing hydrometeor particles and an incident electromagnetic plane wave with power density denoted as $\mathcal{S}_i$ as shown in Figure 17. Each particle is spherical with physical cross-section area $A_p = \pi r^2$, and volume $V_p = 4\pi r^3/3$, where r is the radius. We can describe the power absorbed by the hydrometeor particle as the product of the incident power intensity and an effective absorption cross-sectional area:

$$P_a = Q_a * \mathcal{S}_i \quad \text{(W)}, \tag{63}$$

where Q_a is the product of the physical cross-section area and an absorption efficiency factor:

$$Q_a = \xi_a * \pi r^2 \quad (\text{m}^2), \tag{64}$$

where ξ_a describes the coupling between the EM wave and the hydrometeor particle.

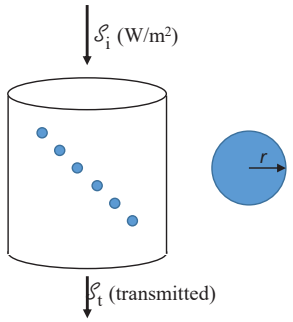

Figure 17. Illustration For Modeling Hydrometeors

Similarly, we can express the power scattered by the particle as the product of the incident power intensity and an effective scattering cross-section area:

$$P_s = Q_s * \mathcal{S}_i \text{ (W)}, \tag{65}$$

where Q_s is the product of the physical cross-section area and a scattering efficiency factor:

$$Q_s = \xi_s * \pi r^2 \quad (\text{m}^2). \tag{66}$$

The total power removed from the incident wave (i.e., power extinction) is:

$$P_e = P_a + P_s \quad \text{(W)}, \tag{67}$$

and the extinction cross section area and efficiency are:

$$Q_e = Q_a + Q_s \quad (\text{m}^2) \tag{68}$$

$$\xi_e = \xi_a + \xi_s \quad \text{(unitless)}. \tag{69}$$

A solution for scattering and absorption of an EM plane wave by a homogeneous dielectric sphere of arbitrary radius was developed by Gustav Mie based on Maxwell's equations [20]. The solution was formulated in terms of two parameters, (1) the normalized particle circumference:

$$\chi = k_b r = \frac{2\pi r}{\lambda_b} = \frac{2\pi r}{\lambda_0}\sqrt{\varepsilon_b'} \quad \text{(unitless)}, \tag{70}$$

and (2) the relative index of refraction:

$$n = \frac{n_p}{n_b} = \sqrt{\frac{\varepsilon_p}{\varepsilon_b}} \quad \text{(unitless)}, \tag{71}$$

where subscript *b* denotes background material (dry air) and subscript *p* denotes particle (water or ice). In air, $\varepsilon_b' = 1$, $n_b = 1$, and $\lambda_b = \lambda_0$.

The results of Mie's solution lead to expressions for the scattering and extinction efficiencies of the sphere in the form of converging series given by:

$$\xi_s(n,\chi) = \frac{2}{\chi^2}\sum_{i=1}^{\infty}(2i+1)(|a_i|^2 + |b_i|^2) \tag{72}$$

$$\xi_e(n,\chi) = \frac{2}{\chi^2}\sum_{i=1}^{\infty}(2i+1)\Re e\{a_i + b_i\}, \tag{73}$$

and

$$\xi_a = \xi_e - \xi_s\,, \tag{74}$$

where $\{a_i, b_i\}$ are the Mie coefficients and are functions of χ and n. The formal expressions for the Mie coefficients involve Bessel functions of complex arguments. For computational purposes, Deirmendjian developed an iterative procedure using the recursion formulas for Bessel functions, which can be found in the references[10] [21, 22]. The variables are (1) the frequency of the EM wave, which determines the wavelength, λ_0, (2) the relative index of refraction (or rather, the relative dielectric constant of the water particle), and (3) the particle radius.

The Mie coefficients are calculated as:

$$a_i = \frac{\left(\frac{A_i}{n}+\frac{i}{\chi}\right)\Re e\{W_i\} - \mathcal{R}e\{W_{i-1}\}}{\left(\frac{A_i}{n}+\frac{i}{\chi}\right)W_i - W_{i-1}} \tag{75}$$

$$b_i = \frac{\left(nA_i+\frac{i}{\chi}\right)\Re e\{W_i\} - \mathcal{R}e\{W_{i-1}\}}{\left(nA_i+\frac{i}{\chi}\right)W_i - W_{i-1}}\,. \tag{76}$$

The terms A_i and W_i are calculated as:

$$A_i = -\frac{i}{n\chi} + \left(\frac{i}{n\chi} - A_{i-1}\right)^{-1} \tag{77}$$

$$A_0 = \cot(n\chi), \tag{78}$$

[10] However, there is an error equation (15) of Deirmendjian's book, which may result in a negative extinction coefficient. The solution given here is from Ulaby's book.

and

$$W_i = \left(\frac{2i-1}{\chi}\right) W_{i-1} - W_{i-2} \tag{79}$$

$$W_0 = \sin(\chi) + j * \cos(\chi) \tag{80}$$

$$W_{-1} = \cos(\chi) - j * \sin(\chi), \tag{81}$$

where $j = \sqrt{-1}$ and n is the index of refraction of the hydrometeor particle.

If the particle size is much smaller than the wavelength of the EM wave, i.e., $|n\chi| << 1$, then the Mie solution simplifies to the Rayleigh approximation [23]. Specifically, only the most significant terms of the series expansions are retained:

$$\xi_s = \frac{8}{3}\chi^4 |K|^2 + \cdots \tag{82}$$

$$\xi_e = 4\chi \Im m\{-K\} + \frac{8}{3}\chi^4 |K|^2 + \cdots \tag{83}$$

$$\xi_a = \xi_e - \xi_x = 4\chi \Im m\{-K\}, \tag{84}$$

where

$$K = \frac{n^2-1}{n^2+2} = \frac{\varepsilon-1}{\varepsilon+2}, \tag{85}$$

where $\mathcal{I}m\{\}$ denotes the imaginary part of the complex value, and n is the index of refraction of the hydrometeor particle.

3.2.5.1.2 Dielectric Constant of Water

A review of the literature suggests that the most accurate model available at the present time for computing the dielectric constant of water is based on a double-Debye dielectric model (D3M) developed by William Ellison and reported in the book edited by Mätzler [24]. The D3M, which was developed for seawater (and reduces to a model for pure water when the water salinity is set to zero), is valid for frequencies below 1000 GHz. The dielectric constants are given by:

$$\varepsilon'_w = \varepsilon_{w\infty} + \frac{\varepsilon_{w0}-\varepsilon_{w1}}{1+(2\pi f \tau_{w1})^2} + \frac{\varepsilon_{w1}-\varepsilon_{w\infty}}{1+(2\pi f \tau_{w2})^2} \tag{86}$$

$$\varepsilon''_w = \frac{2\pi f \tau_{w1}(\varepsilon_{w0}-\varepsilon_{w1})}{1+(2\pi f \tau_{w1})^2} + \frac{2\pi f \tau_{w2}(\varepsilon_{w1}-\varepsilon_{w\infty})}{1+(2\pi f \tau_{w2})^2} + \frac{\sigma_i}{2\pi\varepsilon_0 f}, \tag{87}$$

where ε_0 is the permittivity of free space, and σ_i is the ionic conductivity for the water solution; for pure water, $\sigma_i = 0$. For the derivation and simulations herein, we shall assume pure water. The frequency at which the dielectric constants are evaluated, f, can be in GHz, but then the relaxation time constants, τ_w, must be computed in nanoseconds (ns), so that the units cancel correctly. In general, the parameter functions are:

$$\varepsilon_{w0} = 87.85306 * \exp(-0.00456992 * T - a_1 * S - a_2 * S^2 - a_3 * S * T) \tag{88}$$

$$\varepsilon_{w1} = a_4 * \exp(-a_5 * T - a_6 * S - a_7 * S * T) \tag{89}$$

$$\tau_{w1} = (a_8 + a_9 * S) * \exp\left(\frac{a_{10}}{T+a_{11}}\right) \text{ ns} \quad (90)$$

$$\tau_{w2} = (a_{12} + a_{13} * S) * \exp\left(\frac{a_{14}}{T+a_{15}}\right) \text{ ns} \quad (91)$$

$$\varepsilon_{w\infty} = a_{16} + a_{17} * T + a_{18} * S \quad (92)$$

$$\sigma_i = \sigma * P * Q\ , \quad (93)$$

where

$$\sigma = 2.903602 + (8.607e-2) * T + (4.738817e-4) * T^2 - (2.991e-6) * T^3 + (4.3041e-9) * T^4 \quad (94)$$

$$P = S * \frac{37.5109+5.45216*S+0.014409*S^2}{1004.57+182.283*S+S^2} \quad (95)$$

$$Q = 1 + \frac{\alpha_0(T-15)}{T+\alpha_1}\ , \quad (96)$$

where

$$\alpha_0 = \frac{6.9431+3.2841*S-0.099486*S^2}{84.85+69.024*S+S^2} \quad (97)$$

$$\alpha_1 = 49.843 - 0.2276 * S + 0.00198 * S^2. \quad (98)$$

Coefficients $\{a_1 \ldots a_{18}\}$ are given in Table 7. This semi-empirical model represents the dielectric constant of pure water to within 3% over the frequency range of 30 – 100 GHz. Figure 18 shows the calculated permittivity, ε'_w, and loss factor, ε''_w, as a function of temperature for 72.5 GHz and 82.5 GHz. Permittivity and loss factor increase with temperature. However, they decrease with increasing frequency.

Table 7. Coefficients for Calculating the Dielectric Constant of Water

a_1 = 0.46606917e-2	a_{10} = 0.58366888e3
a_2 = -0.26087876e-4	a_{11} = 0.12684992e3
a_3 = -0.63926782e-5	a_{12} = 0.69227972e-4
a_4 = 0.63000075e1	a_{13} = 0.38957681e-6
a_5 = 0.26242021e-2	a_{14} = 0.30742330e3
a_6 = -0.42984155e-2	a_{15} = 0.12634992e3
a_7 = 0.34414691e-4	a_{16} = 0.37245044e1
a_8 = 0.17667420e-3	a_{17} = 0.92609781e-2
a_9 = -0.20491560e-6	a_{18} = -0.26093754e-1

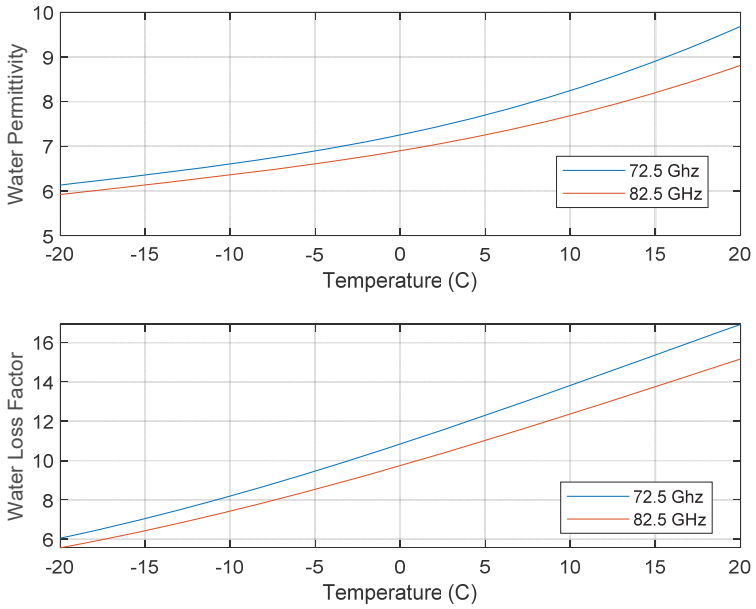

Figure 18. Dielectric Constant of Water as Function of Temperature

3.2.5.1.3 Dielectric Constant for Ice

Now, let's consider the dielectric constant for pure ice, denoted as ε_i. According to Mätlzer and Wegmüller [25], ε_i' is essentially independent of frequency from 10 MHz to 300 GHz and exhibits weak temperature dependence:

$$\varepsilon_i' = 3.1884 + (9.1e-4) * T \ , \tag{99}$$

where T is the temperature in °C and -40 °C ≤ T ≤ 0 °C. The loss factor is given as [26]:

$$\varepsilon_i'' = \frac{\alpha_0}{f} + \beta_0 f \ , \tag{100}$$

where α_0 and f are in GHz, and β_0 is in $(\text{GHz})^{-1}$. The coefficients α_0 and β_0 are given by the semi-empirical expressions:

$$\alpha_0 = (0.00504 + 0.0062 * \theta) * \exp(-22.1 * \theta) \quad \text{(GHz)} \tag{101}$$

$$\beta_0 = \frac{B_1}{T_K} \frac{\exp\left(\frac{b}{T_K}\right)}{\left(\exp\left(\frac{b}{T_K}\right)-1\right)^2} + B_2 * f^2 + \exp\left(-9.963 + 0.0372 * (T_K - 273.16)\right) , \tag{102}$$

where T_K is the temperature in Kelvin, b = 335 K, B_1 = 0.0207 K/GHz, B_2 = 1.16e-11 $(\text{GHz})^{-3}$, and

$$\theta = \frac{300}{T_K} - 1 \ . \tag{103}$$

Figure 19 shows the calculated permittivity, ε_i', and loss factor, ε_i'', as a function of temperature for 72.5 GHz and 82.5 GHz. Permittivity and loss factor increase with temperature. Permittivity is not a function of frequency and only varies slightly over the temperature range. However, the loss

factor increases with frequency. Values of the loss factor are less than 0.008, which is about 3 orders of magnitude lower than for liquid water. Fresh-water ice often contains ionic impurities, such as dissolved salts, which can cause the loss factor to increase significantly (i.e., ~2x – ~8x) in comparison to that for pure ice [27].

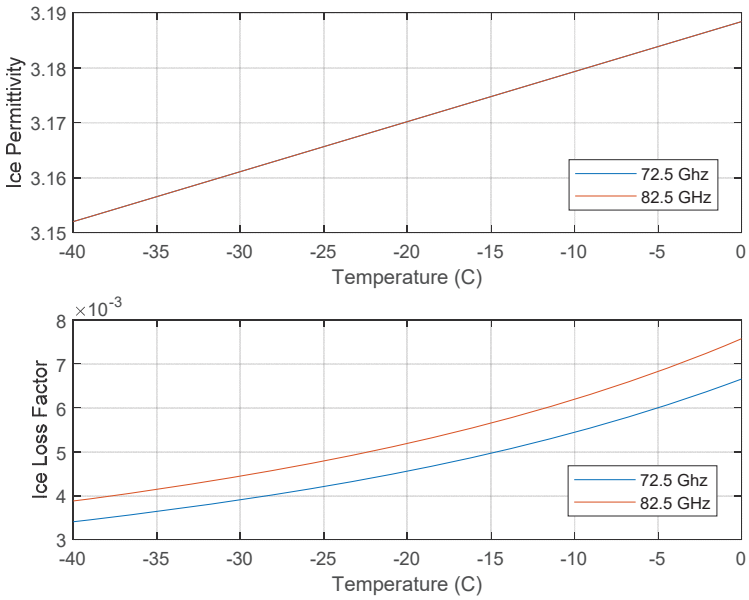

Figure 19. Dielectric Constant of Ice as Function of Temperature

3.2.5.1.4 Absorption and Scattering at W/V-band

Now, let's consider the absorption efficiency, ξ_a, for W/V-band. Let's assume a hydrometeor particle with T = 15 °C and radius r = 10 μm (typical of a liquid water droplet in a fair-weather cumulous cloud), and an EM plane wave with frequency f = 82.5 GHz. The corresponding wavelength is λ_0 = 3.6e-3 m (3.6 mm). The normalized circumference is χ = 0.0173. The dielectric constant (assuming liquid phase) is ε = 8.1994 – j13.7605 and n = 3.4798 – j1.9772. Using the Rayleigh approximation with K = 0.8957 – j0.1407, we find that the absorption efficiency is ξ_a = 0.0097.

For comparison, the first five Mie coefficients were computed and are shown in Figure 20. As expected, their values roll-off quickly. The Mie solution yields ξ_a = 0.0097. The value of $|n\chi|$ = 0.0692. Since $|n\chi| << 1$, the Rayleigh approximation certainly applies to this frequency range and particle size. The scattering efficiency was ξ_s = 1.95e-7, suggesting that scattering can be ignored for this frequency range and particle size.

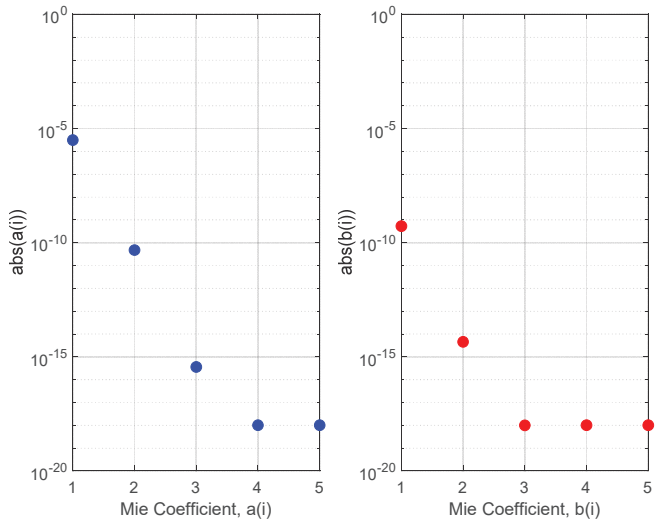

Figure 20. Illustration of Mie Coefficient for Extinction Efficiency Calculation (Cloud)

Figure 21 presents the absorption efficiency as a function of droplet radius (0.01 – 50 μm) for f = 82.5 GHz and T = 15 °C. As expected, the absorption efficiency increases as the droplet size approaches the EM wavelength. Also plotted is $|n\chi|$, which shows that $|n\chi| < 1$ even for r = 50 μm. Thus, even for particles with r = 50 μm, the Rayleigh approximation applies at this frequency. Additionally, the scattering efficiency for r = 50 μm was computed as ξ_s = 1.22e-04, which is a couple orders of magnitude less than the absorption efficiency.

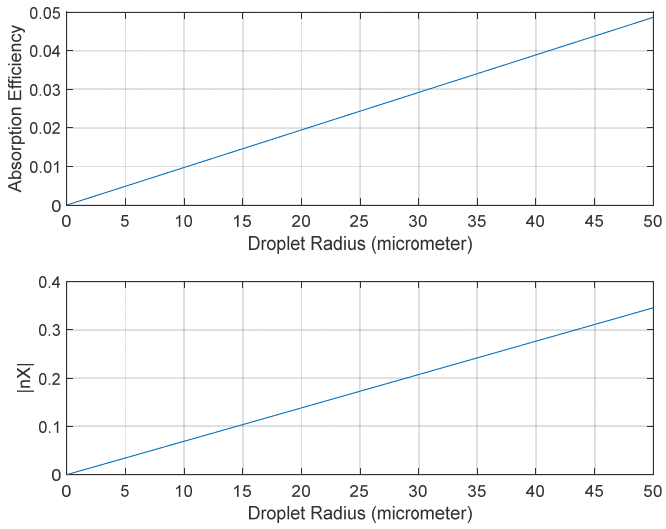

Figure 21. Absorption Efficiency and $|n\chi|$ as a Function of Droplet Radius (T = 15 °C, f = 82.5 GHz)

Figure 22 presents the absorption efficiency as a function temperature for both 72.5 GHz and 82.5 GHz (r = 10 μm). Above about -10 °C, the absorption efficiencies begin rolling off. As expected, the absorption is higher at higher frequency, where the wavelength is shorter and closer to the water particle size.

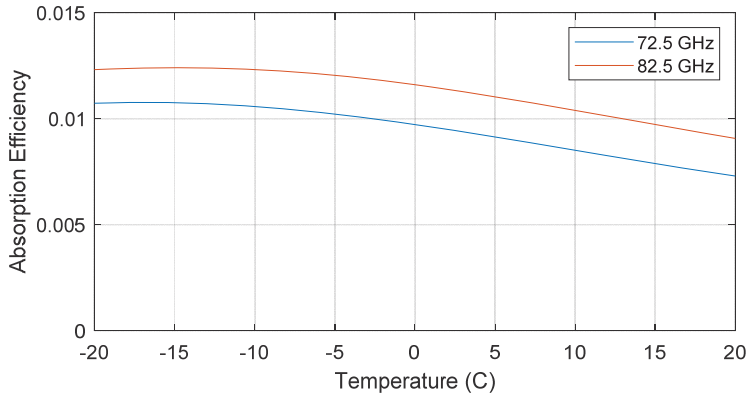

Figure 22. Absorption Efficiency as a Function of Temperature (r = 10 μm)

Figure 23 presents the scattering efficiency as a function of droplet radius for f = 82.5 GHz for three temperatures {-15, 0, 15}. As expected, the scattering efficiency is insignificant relative to the absorption coefficient. Further, there is little apparent impact from the temperature variation. This is due to the difference between the droplet size and the EM wavelength. In the case of rain and frozen precipitation, where the droplet radii are much more close to the wavelength, scattering will become more significant.

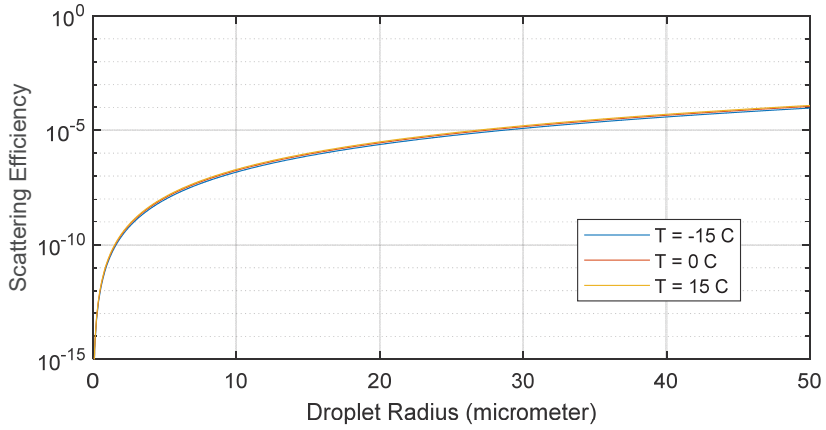

Figure 23. Scattering Efficiency as a Function of Droplet Radius (f = 82.5 GHz)

3.2.5.2 Extending to Many Particles

3.2.5.2.1 Cloud Specific Attenuation Coefficient

Now, we consider a cloud volume containing a mixture of dry air, water vapor, and many condensed particles (i.e., droplets). Recall that mass per unit volume of air is much greater than the mass per unit volume of water vapor[11]. Consequently, we can assume that when many particles exist in a unit volume of atmosphere, those particles do not interact with each other. We can also assume that "shadowing" of one particle by another does not occur. Thus, we conclude that the total scattering (or absorption) cross section of a unit volume of air is equal to the sum of the scattering (or absorption) cross section of all individual particles contained within that unit volume:

$$Q_{a_{Total}} = \sum_{i=1}^{N_v} Q_{a_i}(f, T, r), \tag{104}$$

where N_v is the number of hydrometeor particles in the unit volume, and the dependence of the absorption cross section Q_a on EM wave frequency, temperature, and particle radius is indicated. The range of sizes of particles contained in a cloud is described by a continuous function known as the ***drop size distribution***, denoted here as $p(r)$, which defines the partial concentration of particles per unit volume (m^{-3}) and per unit increment of radius (μm^{-1}) (i.e., the number of particles of size r per unit volume). Thus, in our case, $p(r)$ has units of $m^{-3}\mu m^{-1}$. It can be converted to m^{-4} if r is given in units of meters instead of μm. The ***cloud volume absorption coefficient*** is defined as:

$$\kappa_{a_{cl}} = \int_{r_{min}}^{r_{max}} p(r) Q_a(r)\, dr \quad \text{(Np/m)}, \tag{105}$$

where $\{r_{\min}, r_{\max}\}$ represent the minimum and maximum droplet radii. The cloud volume absorption coefficient is approximated as:

$$\kappa_{a_{cl}} = \sum_{i=1}^{N_v} Q_a(r_i) \quad \text{(Np/m)}, \tag{106}$$

where r_i is the radius of the i^{th} particle. Substituting from Eq. (64),

$$\kappa_{a_{cl}} = \pi \sum_{i=1}^{N_v} \xi_a(r_i) \cdot r_i^2 \quad \text{(Np/m)}. \tag{107}$$

Substituting from Eq. (84),

$$\kappa_{a_{cl}} = 4\pi \cdot \Im m\{-K\} \cdot \sum_{i=1}^{N_v} \chi(r_i) \cdot r_i^2 \quad \text{(Np/m)}. \tag{108}$$

Substituting from Eq. (70),

$$\kappa_{a_{cl}} = 4\pi \cdot \Im m\{-K\} \cdot \sum_{i=1}^{N_v} \left(\frac{2\pi r_i}{\lambda_0}\right) \cdot r_i^2 \quad \text{(Np/m)}, \tag{109}$$

or

$$\kappa_{a_{cl}} = \frac{8\pi^2}{\lambda_0} \cdot \Im m\{-K\} \cdot \sum_{i=1}^{N_v} r_i^3 \quad \text{(Np/m)}. \tag{110}$$

[11] From the Standard Atmosphere model, $\rho_{d0} = 1.225$ kg/m^3 and $\rho_{v0} = 0.0075$ kg/m^3.

The total mass of the liquid water droplets in the cloud is the product of the liquid water density (ρ_L = 1000 kg/m^3) and the sum of the volumes of each droplet:

$$m = \frac{4\pi\rho_L}{3}\sum_{i=1}^{N_v} r_i^3 \quad \text{(kg)}. \tag{111}$$

We can compute the mass density of liquid water of the mixture (i.e., cloud) by dividing m by a unit volume of air:

$$m_L = \frac{m}{V} \quad \text{(kg/m}^3\text{)}, \tag{112}$$

which is also referred to as the ***liquid water content*** (LWC) in many references.

So, we have two volumes in consideration. First is the volume of the mixture, V, which is referred to as a unit volume for convenience, and second is the particle volume(s), $\frac{4}{3}\pi r_i^3$. It is important to keep these clear in order for the units to work out correctly. By dividing both sides of Eq. (111) by a unit volume of mixture, we have:

$$m_L = \frac{4\pi\rho_L}{3}\sum_{i=1}^{N_v} r_i^3 \quad \text{(kg/m}^3\text{)}, \tag{113}$$

which can be solved for the summation and substituted into Eq. (110), which yields:

$$\kappa_{a_{cl}} = \frac{8\pi^2}{\lambda_0}\cdot \Im m\{-K\}\cdot\frac{3m_L}{4\pi\rho_L} \quad \text{(Np/m)}, \tag{114}$$

and simplifying:

$$\kappa_{a_{cl}} = \frac{6\pi}{\rho_L\lambda_0}\cdot \Im m\{-K\}\cdot m_L \quad \text{(Np/m)}. \tag{115}$$

Note that m_L does not include the mass of water vapor in the same unit volume. Care must be taken to insure that units are consistent – if m_L is given in g/m^3 (as often reported in the literature), then ρ_L must be converted to g/m^3 (i.e., 1e6 g/m^3).

The ***liquid extinction coefficient*** is defined from Eq. (115) as:

$$\kappa_L = \frac{6\pi}{\rho_L\lambda_0}\cdot \Im m\{-K\} \quad \text{(Np/m)/(g/m}^3\text{)}, \tag{116}$$

where ρ_L is the density of liquid water in g/m^3, and K is calculated using the dielectric constant of liquid water at the corresponding temperature and frequency.

In the event that particles are frozen, the ***ice extinction coefficient*** is defined as:

$$\kappa_I = \frac{6\pi}{\rho_i\lambda_0}\cdot \Im m\{-K\} \quad \text{(Np/m)/(g/m}^3\text{)}, \tag{117}$$

where ρ_i is the density of ice, and K is calculated using the dielectric constant of ice at the corresponding temperature and frequency. The density of ice is lower than the density of liquid water; the density of ice at T = -20 °C is approximately ρ_i = 920 kg/m^3.

The liquid extinction coefficient and ice extinction coefficient are also referred to as the ***cloud specific attenuation coefficient*** in the literature. This does not include the specific attenuation due to gases or water vapor.

Finally, to convert κ_L or κ_I from (Np/m)/(g/m^3) to (dB/km)/(g/m^3), we simply multiply by 4342.9 as shown in Eq. (20).

Figure 24 shows the cloud specific attenuation coefficient for liquid and frozen hydrometeor particles as a function of frequency for various temperatures. As expected, values increase with frequency as the wavelength approaches particle radii. The specific attenuation coefficients of frozen particles is about two order of magnitude less than the specific attenuation coefficients of liquid particles.

Note that for the liquid state, the value of the specific attenuation coefficients decrease with increasing temperature. This is consistent with Figure 22, which showed the absorption efficiency as a function of temperature. For frozen particles, the value of the specific attenuation coefficients increase with increasing temperature.

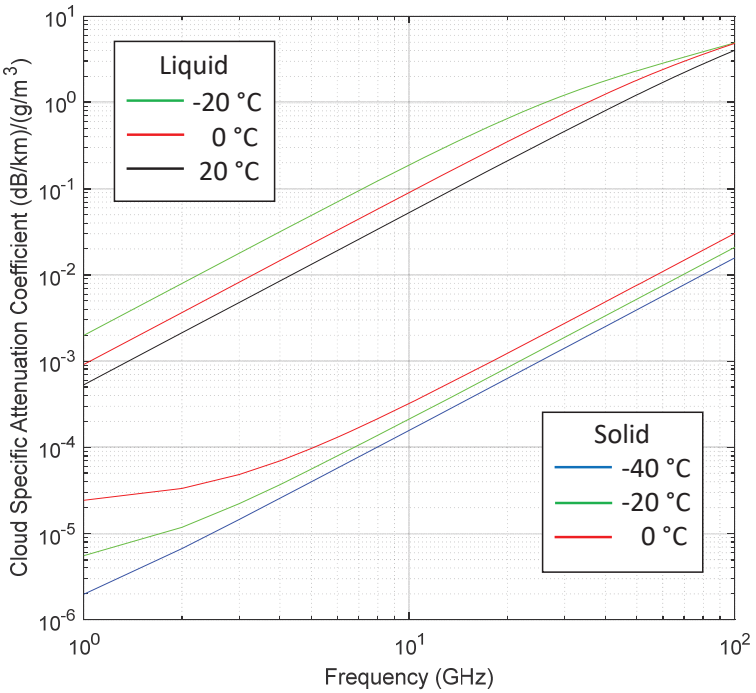

Figure 24. Liquid and Solid (Ice) Cloud Specific Attenuation Coefficients

Figure 25 plots the specific attenuation coefficients for liquid and solid particles at 72.5 GHz and 82.5 GHz as a function of temperature. The higher frequency has higher values of specific attenuation. There is about two orders of magnitude difference between the solid and liquid phases.

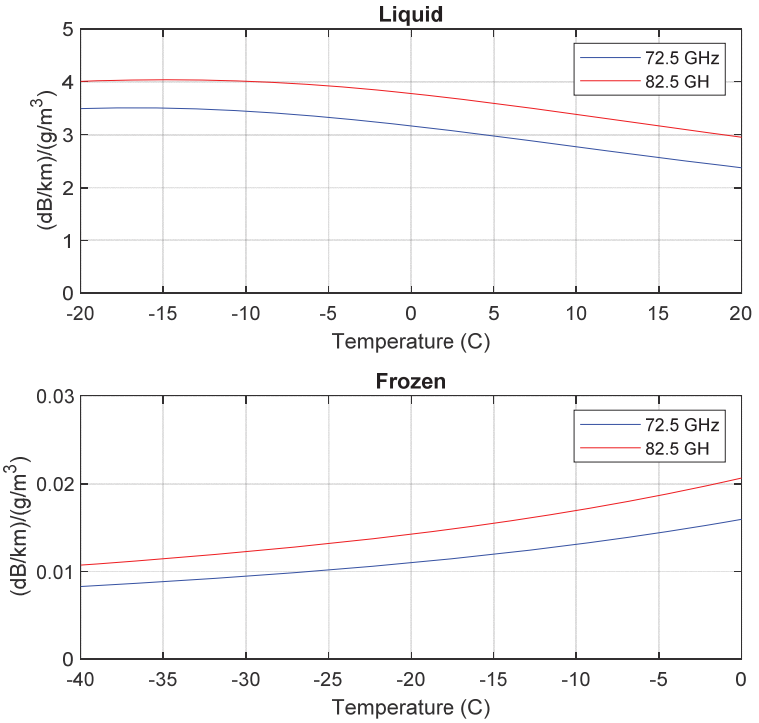

Figure 25. Liquid and Solid (Ice) Cloud Specific Attenuation Coefficients

3.2.5.2.2 Mixed Phase Clouds

Both solid and liquid particles can coexist in a cloud, referred to as mixed clouds, but the concentrations of each are not discernable and are dynamic, which introduces uncertainty into the estimated cloud attenuation. The temperature that a cloud top must reach in order to change its state from predominantly liquid water to predominantly ice (called the cloud glaciation temperature) can assume values between approximately -5 °C to -37 °C [28]. In mixed clouds, ice crystals grow preferentially with respect to the water droplets, because water vapor evaporates from the droplets and deposits onto the ice crystals. Thus, mixed clouds last for only short times before becoming all ice crystals (i.e., process called glaciation). Once the first ice crystals have formed, they can grow at the expense of evaporating droplets (i.e., Wegener-Bergeron-Findeisen process [29]) and/or induce ice multiplication processes [30], both of which may rapidly lead to a full glaciation of the cloud. Therefore, observed ice mass fractions (i.e., cloud ice divided by total cloud water) are typically either close to 0 or close to 1, with a low frequency of occurrence of intermediate values [31, 32].

3.2.5.3 Cloud Formation and Adiabatic Expansion

Ten basic cloud types were first characterized by Luke Howard in 1803 in an essay titled, *On the Modification of Clouds*[12] and are illustrated in Figure 26. Water droplets can, in theory, result from condensing upon each other under supersaturated conditions (i.e., (relative humidity) RH > 400%), a process called homogenous nucleation, but this is rare [33]. Typically, cloud droplets form by heterogeneous nucleation, where water droplets condense onto aerosols, such as dust, salt, pollen, or air pollutants. These aerosols are referred to as condensation nuclei and enable condensation at RH ~100%, i.e., saturation.

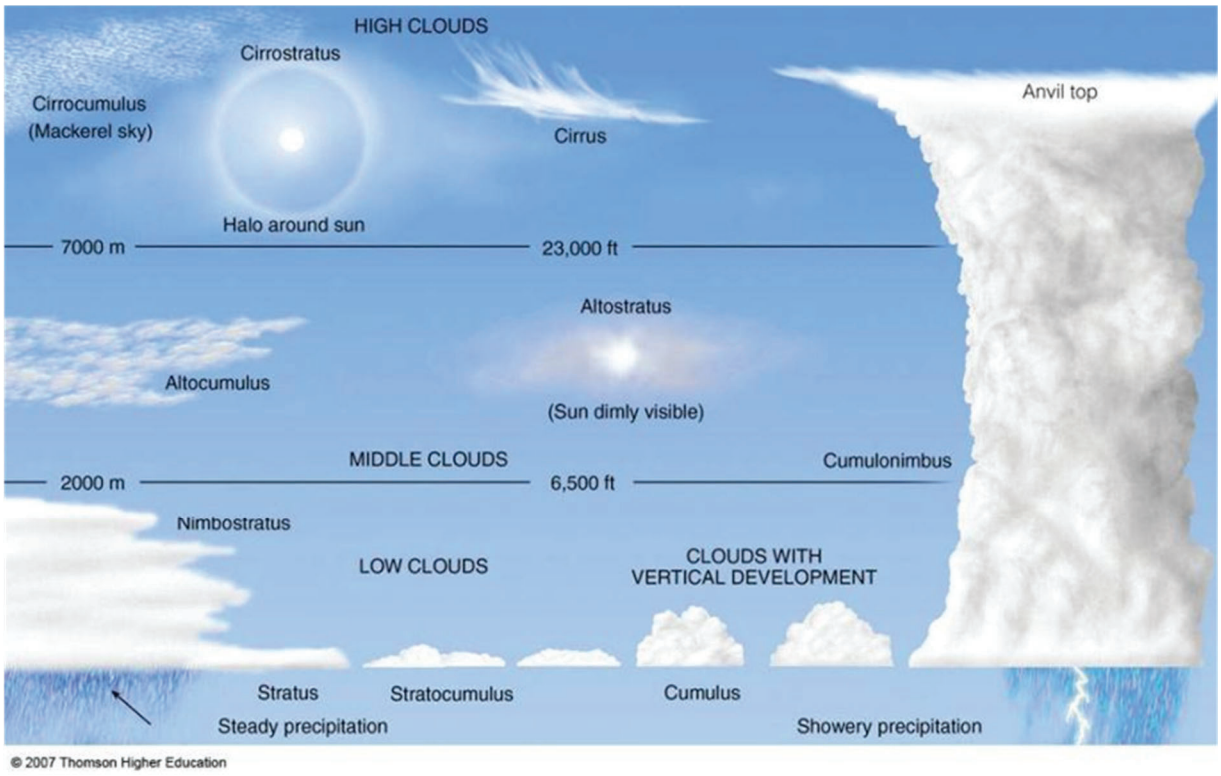

Figure 26. Basic Cloud Types and Altitudes

There are three mechanisms by which a parcel of air can be brought to saturation: (1) adding water vapor to the parcel, (2) decreasing the temperature of the parcel by removing heat, or (3) decreasing the temperature of the parcel through an adiabatic process (i.e., expansion). Adiabatic means that

[12] "In order to enable the Meteorologist to apply the key of Analysis to the experience of others, as well as to record his own with brevity and precision, it may perhaps be allowable to introduce a Methodical nomenclature, applicable to the various forms of suspended water, or, in other words, to the Modification of Cloud. By modification is to be understood simply the Structure or manner of aggregation, not the precise form or magnitude, which indeed varies every moment in most Clouds." – Howard, *On the Modification of Clouds*, John Churchill & Sons, London, 1803.

no heat is transferred to or from the parcel. The first two processes are effective close to the surface and can result in fog. Clouds mostly form from the third process.

Generally, air parcels can be lifted by orographic lifting (due to topography), convergence, frontal lifting, and by convection [33]. Also, if a parcel of air becomes warmer than its environment, then its density becomes lower than the surrounding environment, and it experiences a buoyant force that causes it to ascend.

Regardless, as an air parcel ascends, the volume of the parcel will expand, because the earth is spherical and pressure decreases with altitude (consider how a weather balloon expands as it rises through the atmosphere). The pressure adjustment is nearly instantaneous (i.e., the pressure of the parcel is equal to the pressure of the surrounding environment). However, the heat exchange process is much slower, so the temperature of the ascending parcel does not adjust as quickly to the temperature of the surrounding air. Thus, expansion of the ascending parcel is ***adiabatic*** -- no heat transfer[13].

Let's consider an unsaturated air parcel at surface altitude denoted as h_0 as illustrated in Figure 27. The parcel is a mixture of water vapor and dry air, with temperature T_p, pressure P_p, and density ρ_p. We will define the surrounding environment as having temperature T_{env}, pressure P_{env}, and density ρ_{env}. To start, we will assume that the temperature, pressure, and density of the parcel is equivalent to the temperature, pressure, and density of the surrounding environment. The parcel is comprised of dry air with mass m_d and water vapor of mass m_v. Both have temperature T_p. The partial pressures of the dry air and water vapor in the parcel are P_d and e, respectively, where:

$$P_d + e = P_p = P_{env}. \tag{118}$$

Let's define the ***mixing ratio*** as the ratio of the mass of water vapor to the mass of dry air in the parcel:

$$\varphi = \frac{m_v}{m_d} \ \text{(kg/kg)}. \tag{119}$$

Note that sometimes φ is expressed as grams of water vapor per kilograms of air (g/kg). We assume that there is no mass exchanged between the parcel and the surrounding environment. Therefore, mass is conserved, and φ is constant as the parcel ascends – at least, until condensation, deposition, or precipitation occurs, upon which water vapor mass leaves the parcel and φ decreases.

[13] Over time, there is heat exchange, which can cause cloud particles to evaporate.

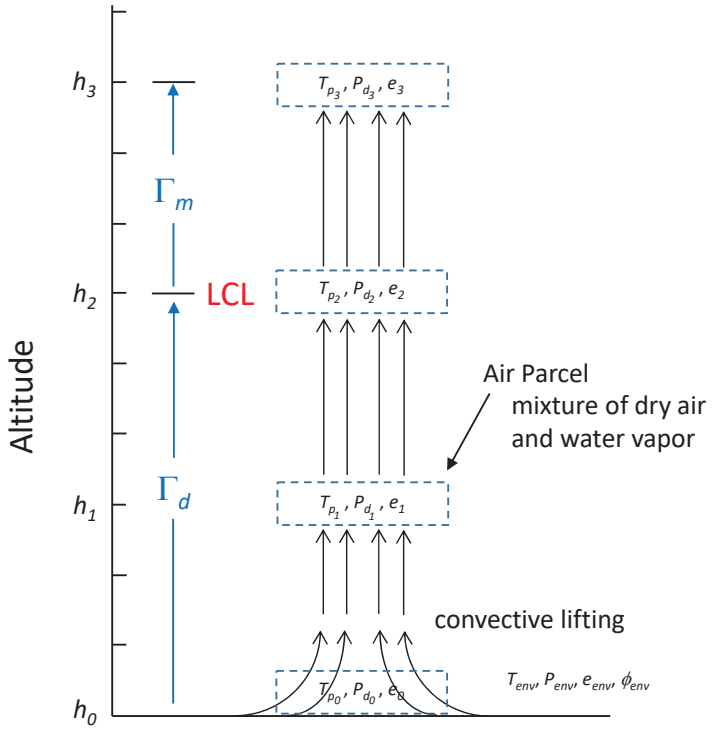

Figure 27. Illustration of an Air Parcel Being Lifted Adiabatically

Using the ideal gas law, we can write the mixing ratio as:

$$\varphi = \frac{m_v}{m_d} = \frac{\rho_v}{\rho_d} = \frac{\frac{e}{R_v T_p}}{\frac{Pd}{R_d T_p}} = 0.622\frac{e}{P_d} \quad , \tag{120}$$

where R_v = 461.51 J/(kg·K) and R_d = 287.0 J/(kg·K). Further, the density of the mixture in the parcel is:

$$\rho_p = \frac{m_d + m_v}{V} = \rho_d + \rho_v \quad (\text{kg/m}^3), \tag{121}$$

where V denotes a unit volume. Substituting from the ideal gas equation yields:

$$\rho_p = \frac{P_d}{R_d T_p} + \frac{e}{R_v T_p} \quad (\text{kg/m}^3), \tag{122}$$

which shows that the gas constant for the mixture is neither R_d or R_v, but an inconvenient varying combination. Substituting from Eq. (118), we have:

$$\rho_p = \frac{P_p - e}{R_d T_p} + \frac{e}{R_v T_p} \quad (\text{kg/m}^3). \tag{123}$$

This can be expressed in terms of R_d only by rearranging and substituting from Eq. (120):

$$\rho_p = \frac{P_p}{R_d T_p}\left(1 - \frac{e}{P_p}(1 - 0.622)\right) \quad (\text{kg/m}^3). \tag{124}$$

We can define a ***virtual temperature***, T_v, for the parcel in terms of only R_d as:

$$T_v = \frac{P_p}{\rho_p R_d} \quad \text{(K)}, \tag{125}$$

where, after substituting from Eq. (124):

$$T_v = \frac{T_p}{1-0.378\left(\frac{e}{P_p}\right)} \quad \text{(K)}. \tag{126}$$

Because moist air is less dense than dry air at the same temperature and pressure, the virtual temperature is always greater than the actual temperature of the parcel [34].

3.2.5.3.1 Dry Adiabatic Lapse Rate

The relative humidity of the parcel, as defined previously, is:

$$\phi = 100\left(\frac{e}{e_s}\right), \tag{127}$$

where e_s is the saturation pressure corresponding to the temperature of the parcel, T_p. As the parcel rises, it undergoes adiabatic expansion and the change of temperature of the parcel, T_p, as a function of altitude is:

$$\left(\frac{-dT_p}{dz}\right)_{dry} = \frac{g}{c_p} \stackrel{\text{def}}{=} \Gamma_d \quad \text{(K/m)}, \tag{128}$$

where g is the acceleration of gravity, c_p is the specific heat of air at constant pressure (1004 J/(kg·K)), and Γ_d is the ***dry adiabatic lapse rate*** [35]:

$$\Gamma_d = 9.8 \quad \text{(K/km)}. \tag{129}$$

Note that the temperature decrease of the air parcel is independent of the temperature of the surrounding environment and depends only on the change in altitude. Since we are considering a change in temperature, 9.8 K/km is equivalent to 9.8 °C/km, or 0.0098 °C/m.

Now, let's assume that the parcel is lifted to altitude h_1, where it remains unsaturated (i.e., $e(h_1) < e_s(h_1)$). The temperature of the parcel at h_1 is:

$$T_{p_1} = T_{p_0} - \Gamma_d(h_1 - h_0) \quad \text{(K)}, \tag{130}$$

which is not the same as the temperature of the surrounding environment. The pressure of the parcel, P_{p_1}, is equivalent to the pressure of the surrounding environment (obtained from a model, such as the Standard Atmosphere model, or measurements from a radiosonde). We know that the pressure decreases exponentially as the volume of the parcel expands. However, the ratio of the partial pressures remains constant because the mass of the water vapor and mass of the dry air remain constant (i.e., mass conservation):

$$\frac{e_1}{P_{d_1}} = \frac{\varphi_1}{0.622}, \tag{131}$$

and

$$P_{p_1} = P_{d_1} + e_1 \quad \text{(hPa)}. \tag{132}$$

Dividing both sides by P_{d_1}, substituting, and solving for P_{d_1} yields:

$$P_{d_1} = \frac{P_{p_1}}{1+\frac{\varphi_1}{0.622}} \quad \text{(hPa)}. \tag{133}$$

We can calculate P_{d_1} and then e_1. The saturation pressure, e_{s_1}, can be determined from T_{p_1}, which enables calculation of the relative humidity, ϕ_1. To calculate the change in volume of the parcel from h_0 to h_1, we recall that mass is conserved. Considering just the dry air mass:

$$m_{d_0} = m_{d_1}\ , \tag{134}$$

$$\rho_{d_0} V_0 = \rho_{d_1} V_1, \tag{135}$$

$$\frac{V_1}{V_0} = \frac{\rho_{d_0}}{\rho_{d_1}}. \tag{136}$$

As the air parcel rises, the partial pressure of the water vapor decrease, $e(h_i) < e(h_{i-1})$, and the saturation pressure decreases, $e_s(h_i) < e_s(h_{i-1})$.

Now, let's assume that the parcel is lifted to altitude h_2, at which $e_2 = e_{s_2}$ and therefore $\phi_2 = 100\%$. Any additional lifting of the parcel can result in water vapor condensation (or deposition) from the mixture to the liquid (or solid) phase, which may precipitate out of the parcel. In this case, mass is no longer conserved (specifically, m_v is no longer conserved – m_d does not change). This is the altitude of the cloud base and is referred to as the ***lifted condensation level*** (LCL).

3.2.5.3.2 Moist Adiabatic Lapse Rate

As previously discussed, the process of changing phase from a vapor to liquid (or solid) releases latent heat. This latent heat warms the air / water vapor mixture in the parcel. The net result is that the parcel cools at a slower rate than the dry adiabatic lapse rate. From the law of conservation of energy [36]:

$$dq = c_p dT + g dz \quad \text{(J/kg)}, \tag{137}$$

where dq is the heat provided by the change of phase. Note that if $dq = 0$, we obtain the dry adiabatic lapse rate given in Eq. (128). If water vapor condenses, then:

$$dq = -L_v dw_s \quad \text{(J/kg)}, \tag{138}$$

where L_v is the enthalpy of vaporization (or the latent heat of condensation), and dw_s is the change in the saturation mixing ratio, w_s:

$$w_s = \frac{m_{v_s}}{m_d} = 0.622\left(\frac{e_s}{P_d}\right) \quad \text{(kg/kg)}. \tag{139}$$

Substituting into Eq. (137), dividing by c_p and dividing by dz yields:

$$\frac{-L_v dw_s}{c_p dz} = \frac{dT}{dz} + \frac{g}{c_p} \quad \text{(K/m)}. \tag{140}$$

Rearranging terms yields:

$$\frac{dT}{dz} = \frac{-L_v}{c_p dz} dw_s - \frac{g}{c_p} \text{ (K/m).} \tag{141}$$

From Eq. (139), we observe that w_s is a function of both temperature (because e_s is a function of temperature) and pressure, P_d. Therefore, we can express the differential of the saturation mixing ratio as:

$$dw_s = \left(\frac{dw_s}{dP_d}\right)_T dP_d + \left(\frac{dw_s}{dT}\right)_{P_d} dT \text{ (kg/kg),} \tag{142}$$

where the variation of the saturation mixing ratio with respect to pressure is evaluated at constant temperature, and the variation of the saturation mixing ratio with respect to temperature is evaluated at constant pressure. Substituting Eq. (142) into Eq. (141) yields:

$$\frac{dT}{dz} = \frac{-L_v}{c_p dz}\left[\left(\frac{dw_s}{dP_d}\right)_T dP_d + \left(\frac{dw_s}{dT}\right)_{P_d} dT\right] - \frac{g}{c_p} \text{ (K/m)} \tag{143}$$

$$\frac{dT}{dz} = -\frac{L_v}{c_p}\left(\frac{dw_s}{dP_d}\right)_T \frac{dP_d}{dz} - \frac{L_v}{c_p}\left(\frac{dw_s}{dT}\right)_{P_d} \frac{dT}{dz} - \frac{g}{c_p} \text{ (K/m)} \tag{144}$$

$$\frac{dT}{dz} + \frac{L_v}{c_p}\left(\frac{dw_s}{dT}\right)_{P_d} \frac{dT}{dz} = -\frac{L_v}{c_p}\left(\frac{dw_s}{dP_d}\right)_T \frac{dP_d}{dz} - \frac{g}{c_p} \text{ (K/m)} \tag{145}$$

$$\frac{dT}{dz}\left[1 + \frac{L_v}{c_p}\left(\frac{dw_s}{dT}\right)_{P_d}\right] = -\frac{g}{c_p}\left[1 + \frac{L_v}{g}\left(\frac{dw_s}{dP_d}\right)_T \left(\frac{dP_d}{dz}\right)\right] \text{ (K/m).} \tag{146}$$

For an atmosphere in hydrostatic balance:

$$\frac{dP_d}{dz} = -g\rho_d \text{ (Pa/m),} \tag{147}$$

where pressure is in Pa, as opposed to hPa, so that units correctly cancel. Substituting and simplifying yields:

$$\frac{dT}{dz}\left[1 + \frac{L_v}{c_p}\left(\frac{dw_s}{dT}\right)_{P_d}\right] = -\frac{g}{c_p}\left[1 - \rho_d L_v \left(\frac{dw_s}{dP_d}\right)_T\right] \text{ (K/m)} \tag{148}$$

$$\frac{dT}{dz} = \frac{-\frac{g}{c_p}\left[1 - \rho_d L_v \left(\frac{dw_s}{dP_d}\right)_T\right]}{\left[1 + \frac{L_v}{c_p}\left(\frac{dw_s}{dT}\right)_{P_d}\right]} \text{ (K/m).} \tag{149}$$

We define the ***moist adiabatic lapse rate*** as:

$$\Gamma_m = -\frac{dT}{dz} \text{ (K/m).} \tag{150}$$

In the case of deposition, one should use L_s. We can numerically evaluate the derivatives:

$$\left(\frac{dw_s}{dP_d}\right)_T = \frac{w_s(P_d + \Delta P_d) - w_s(P_d)}{\Delta P_d} \text{ (Pa}^{-1}\text{)} \tag{151}$$

$$\left(\frac{dw_s}{dT}\right)_{P_d} = \frac{w_s(\mathrm{T} + \Delta \mathrm{T}) - w_s(T)}{\Delta \mathrm{T}} \text{ (K}^{-1}\text{),} \tag{152}$$

where w_s was defined in Eq. (139). Again, note that the units of Eq. (151) are in Pa, not hPa. We also note that evaluating the derivatives by interpolating e_s from the steam tables is problematic, so the equations for e_s (or e_{si}) given in Eq. (45) and Eq. (46) should be used instead.

Let's illustrate using values of pressure and temperature from the Standard Atmosphere model, using h_{min} = 0 m and h_{max} = 10000 m. Figure 28 plots the derivative of the saturation mixing ratio with respect to dry air pressure with temperature held constant, Eq. (151), and the derivative of the saturation mixing ratio with respect to temperature with dry air pressure held constant, Eq. (152). Both are plotted as a function of temperature (°C). Recall that the standard atmosphere temperature at h = 0 m is 15 °C, and drops to -50 °C at 10000 m. The variation with respect to pressure (left) is about three orders of magnitude less than the variation with respect to temperature (right). Figure 28 also shows the derivatives if deposition occurs, instead of condensation (at temperatures below 0 °C). In this case, L_s was used instead of L_v (both assumed constant for our temperature range). Values are very similar.

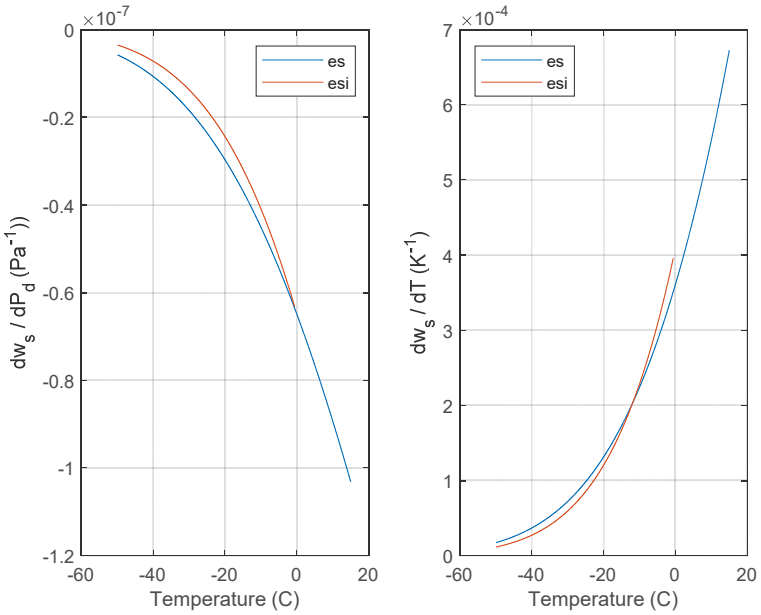

Figure 28. Derivatives of Mixing Ratio Using the Standard Atmosphere Model

Figure 29 plots the moist adiabatic lapse rate as a function of altitude. At lower altitudes, where the temperature is higher and therefore there is more water vapor that can condense and release latent heat, the lapse rate is much lower than the dry adiabatic lapse rate. At higher altitudes, where there would be less moisture and less latent heat produced, the lapse rate approaches the dry adiabatic lapse rate. The moist adiabatic lapse rate is also shown for the transition of vapor-to-solid (deposition). Temperature decreases below 0 °C at about 2400 m, so the curve starts there. At 2400 m, the moist adiabatic lapse rate for vapor-to-liquid is Γ_m = 6.0 K/km, while for vapor-to-solid is Γ_m = 5.4 K/km. This is reasonable, since $L_s > L_v$ (i.e., there is more latent heat released

from deposition than from condensation – therefore, less cooling from the adiabatic expansion). Finally, note that at 0 m (15 °C), Γ_m = 4.8 K/km. Thus, the rate of change of Γ_m from 0 – 2400 m is small; $d(\Gamma_m)/dz$ = 5.2e-4 (K/m)/km, or equivalently, $d(\Gamma_m)/dT$ = 8e-5 (K/m)/K – a smooth and slow variation with temperature, altitude, and consequently pressure.

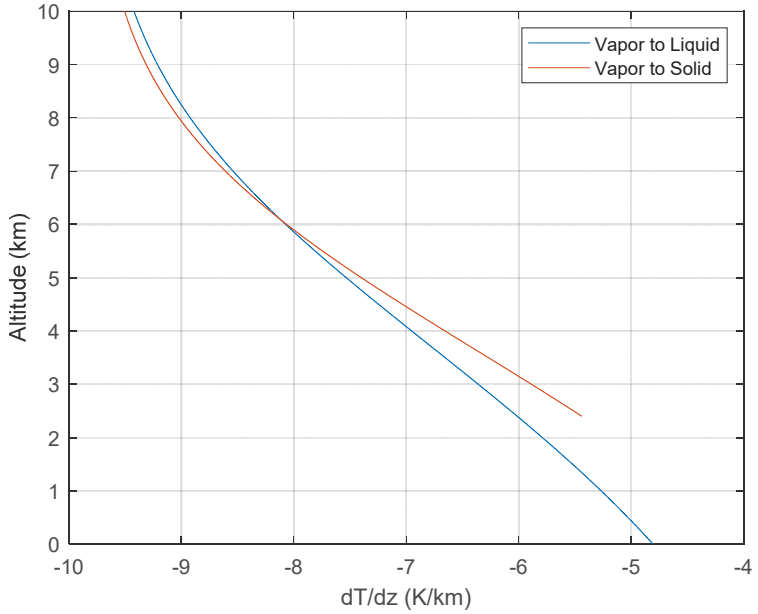

Figure 29. Moist Adiabatic Lapse Rate Using the Standard Atmosphere Model

Now, let's assume that the parcel is lifted to altitude h_3. The temperature of the parcel at h_3 is:

$$T_{p_3} = T_{p_2} - \Gamma_m(h_3 - h_2) \quad \text{(K)}, \tag{153}$$

and the parcel remains saturated (ϕ_3 = 100%). We can use T_{p_2} and P_{d_2} to estimate Γ_m if $h_3 - h_2$ is not too large, since we know that Γ_m varies slowly with temperature and pressure. We can then compute the saturation vapor pressure using the steam tables, Eq. (45) or Eq. (46), as appropriate, and compute the pressure of the parcel:

$$e_3 = e_{s_3} \text{ (Pa)}, \tag{154}$$

$$P_{d_3} = P_{p_3} - e_3 \text{ (Pa)}. \tag{155}$$

Density of the dry air, water vapor, and total density of the mixture are calculated as:

$$\rho_{d_3} = \frac{P_{d_3}}{R_d T_{p_3}} \text{ (kg/m}^3\text{)} \tag{156}$$

$$\rho_{e_3} = \frac{e_3}{R_v T_{p_3}} \text{ (kg/m}^3\text{)} \tag{157}$$

$$\rho_{p_3} = \rho_{d_3} + \rho_{e_3} \text{ (kg/m}^3\text{)}. \tag{158}$$

The change in volume of the parcel from h_2 to h_3 follows Eq. (134), Eq. (135), and Eq. (136) to yield:

$$V_3 = \left(\frac{\rho_{d_2}}{\rho_{d_3}}\right) V_2 \text{ (m}^3\text{)}. \tag{159}$$

Since the parcel is in a saturated state, water vapor may condense to liquid and leave the volume. Therefore, m_v is not constant, and neither is the total mass, $m_v + m_d$. So, we must use the densities of dry air, ρ_{d_2} and ρ_{d_3}.

It may be of interest to know how much mass has condensed out of the mixture as liquid (or solid) – although not necessarily precipitated out of the parcel. The condensed mass from h_2 to h_3 is given by:

$$\Delta m_v = m_{v_2} - m_{v_3} \text{ (kg)} \tag{160}$$

$$\Delta m_v = m_d \varphi_2 - m_d \varphi_3 \text{ (kg)} \tag{161}$$

$$\Delta m_v = m_d(\varphi_2 - \varphi_3) \text{ (kg)}. \tag{162}$$

The condensed mass per unit volume is simply:

$$\rho_{condensed} = \frac{\Delta m_v}{V_3} \text{ (kg/m}^3\text{)} \tag{163}$$

3.2.5.3.3 Stability

Atmosphere and lifting conditions may or may not support continued cloud development and the cloud may simply dissipate. The lifted air parcel may be ***stable***, ***neutrally stable***, or ***unstable***. The parcel is considered stable if the temperature of the parcel is lower than the temperature of the surrounding air (i.e., $T_p < T_{env}$), in which case there is a net downward buoyant force and the parcel will tend to sink back to its pre-lifted position. The parcel is considered neutrally stable if its temperature is similar to the surrounding air temperature ($T_p \approx T_{env}$), in which case there is no net buoyant force. This results in fair-weather cumulous clouds that are common on sunny days. The parcel is considered unstable if its temperature is greater than the temperature of the surrounding air ($T_p > T_{env}$), in which case there is a net upward buoyant force. At this point, the parcel will continue to ascend without the need of any other lifting force, which is called ***freely buoyant***. At this altitude, forced convection (i.e., lifting) gives way to free convection. This altitude is called the ***level of free convection*** and constitutes an important diagnostic of the state of the atmosphere when there is a possibility of thunderstorms. In this case, the air parcel will keep rising until it becomes colder than the environment, which might not occur until ~12 km, near the tropopause. This results in cumulonimbus clouds, which produce thunderstorms [33].

In real clouds, unsaturated ambient air is pulled into the cloud (i.e., entrained), which impacts development. Precipitation impacts cloud development. Also, real clouds are not homogenous – there are pockets of saturated air mixed among pockets of unsaturated air, producing a sponge or Swiss cheese effect [37]. Finally, cloud development relies on a continuous mass flow (lifting) of moist air from the surface by the convection process, i.e., one parcel following another. In general,

warm air rises and cool air sinks, unless there is a lifting process to push cool air upward, and such lifting processes varying with time. Consequently, there is much uncertainty regarding the development of clouds.

3.2.5.4 Adiabatic Lifting with Standard Atmosphere

It is informative if we quantitatively consider the states of an air parcel being lifted adiabatically. To do this, we make use of the Standard Atmosphere model again. We assume a unit volume parcel of air at h_0 at the standard atmosphere conditions. Next, we assume the parcel is lifted to 10000 m. States of the parcel and environment were calculated for Δh = 100 m.

Figure 30 (left) shows the temperature of the parcel and the surrounding environment. T_{env} exhibits the lapse rate of 6.5 °C/km that is characteristic of the Standard Atmosphere model. The lifted condensation level (i.e., cloud base height) was computed to be at about 1100 m (3,600 ft). This is the altitude at which the cloud starts. As the altitude continues to increase, $T_p < T_{env}$, which suggests a stable parcel – without a lifting force such as convection, the parcel will sink back to the surface and the cloud dissipates. For this simulation, vapor-to-liquid condensation was assumed if $T_p \geq$ -20 °C. Vapor-to-solid deposition was assumed for $T_p <$ -20 °C. Figure 30 (right) shows the adiabatic lapse rate for the parcel. The moist adiabatic lapse rate started at about 5.8 °C/km (equivalent to 5.8 K/km) just above the lifted condensation level and approached the dry adiabatic lapse rate with increasing altitude. The abrupt transition from condensation to deposition occurred at an altitude of about 4800 m, which corresponded to T_p = -20 °C. The impact to the value of Γ_m was minor, as expected from Figure 29. One final observation to note is the altitude within the cloud at which the 0 °C isotherm occurred. For this simulation, the 0 °C isotherm occurred at about 1800 m, which is 700 m above the LCL. Typically, any frozen precipitation from the upper part of the cloud begins melting below the 0 °C isotherm. The region around the 0 °C isotherm is often referred to as the melting layer in the literature. Rainfall distance is often estimated relative to the altitude of the 0 °C isotherm.

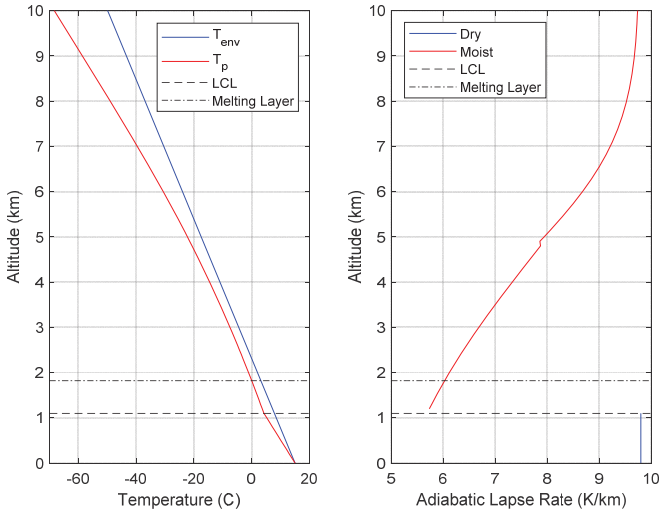

Figure 30. Quantitative Example of an Air Parcel Being Lifted Adiabatically Using the Standard Atmosphere Model (Temperature and Lapse Rate)

Figure 31 shows the corresponding mixing ratio (left) and volume expansion ratio (right) for the lifted parcel. The mixing ratio, φ, was constant (m_v = 7.5 g, m_d = 1.2252 kg, and φ = 0.0061 kg/kg or φ = 6.1 g/kg) up to the lifted condensation level. Above the LCL, m_v and φ approach 0, while m_d is constant throughout. The abrupt transition from e_s to e_{si} can be observed at about the 4800 m altitude. The expansion ratio (right) indicated a smooth exponential increase with altitude. At 10000 m, the volume ratio was 2.72 m^3/m^3.

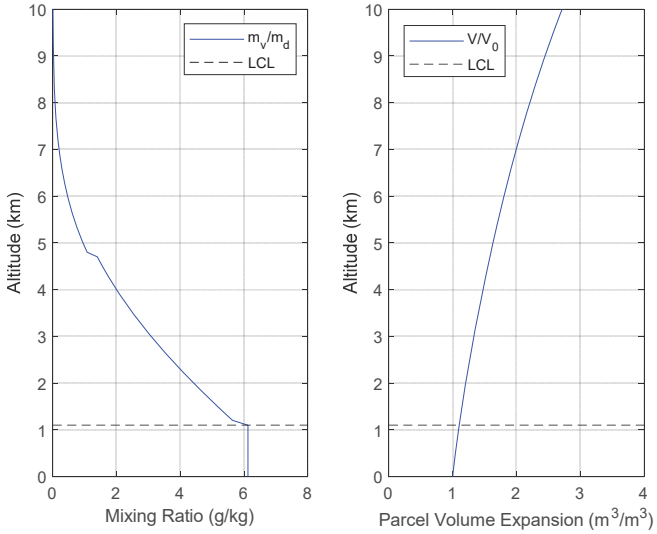

Figure 31. Quantitative Example of an Air Parcel Being Lifted Adiabatically Using the Standard Atmosphere Model (Mixing Ratio and Volume)

3.2.5.4.1 Comparison of Standard Atmosphere to Radiosonde - Cloudy

At this point, it is informative if we compare the Standard Atmosphere to the measured values provided by a radiosonde. The radiosonde data was measured from Albuquerque, NM (h_{min} = 1619 m) during an evening (5 PM – 6 PM) during January with ***cloudy*** (overcast) conditions. Figure 32 shows the temperature (left) and pressure (right). Surface temperature was 9.6 °C. The 0 °C isotherm was at about 2600 m. The LCL was at about 3356 m. Although the radiosonde necessarily ascended through clouds, the measurements in Figure 32 are indicated as being of the surrounding environment $\{T_{env}, P_{env}\}$, as opposed to the parcel $\{T_p, P_p\}$ as previously modeled. Surface pressure was 838 hPa, which is the barometric pressure, or total pressure (i.e., dry air pressure + water vapor pressure). The agreement between the radiosonde data and the Standard Atmosphere model is remarkable.

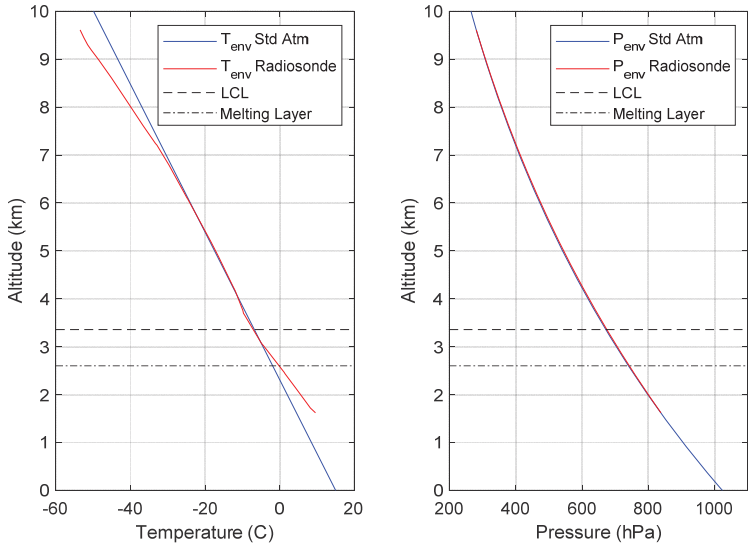

Figure 32. Comparison of Standard Atmosphere to Radiosonde Measurement (Temperature and Pressure) – Cloudy Conditions

Figure 33 shows the mixing ratio (left) and relative humidity (right). The mixing ratio measured by radiosonde was greater than the mixing ratio of the Standard Atmosphere model, which is reasonable since the data were measured during cloudy (overcast) conditions. At higher altitude, the mixing ratio tended toward zero as expected. Likewise, the relative humidity was greater than 50% from about 2250 m through 8750 m. The relative humidity at the surface was 37%. The maximum relative humidity was 88%, which occurred at the LCL. Unfortunately, we do not know the height of the cloud layer where the radiosonde ascended, therefore **we cannot correlate cloud layer thickness to the relative humidity measurements**.

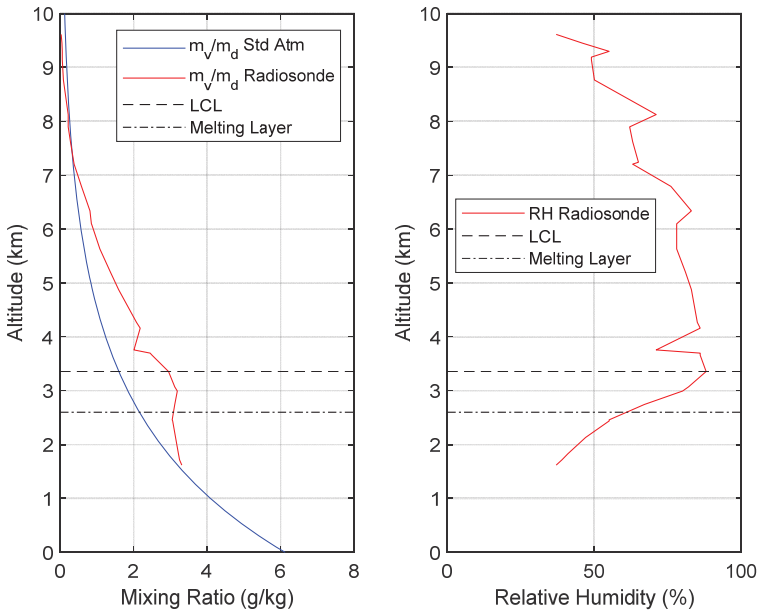

Figure 33. Comparison of Standard Atmosphere to Radiosonde Measurement (Mixing Ratio and Relative Humidity) – Cloudy Conditions

3.2.5.4.2 Comparison of Standard Atmosphere to Radiosonde - Clear

For comparison, the Standard Atmosphere model is compared to radiosonde data measured from Albuquerque, NM (h_{min} = 1619 m) during an evening (5 PM – 6 PM) during January with ***clear sky*** conditions. Figure 34 shows the temperature (left) and pressure (right). Surface temperature was 6.8 °C. The 0 °C isotherm was at about 2227 m. The LCL was at about 3185 m. Surface pressure was 842 hPa. Again, there is close agreement between the radiosonde data and the Standard Atmosphere model, despite the change of conditions (i.e., clear versus cloudy).

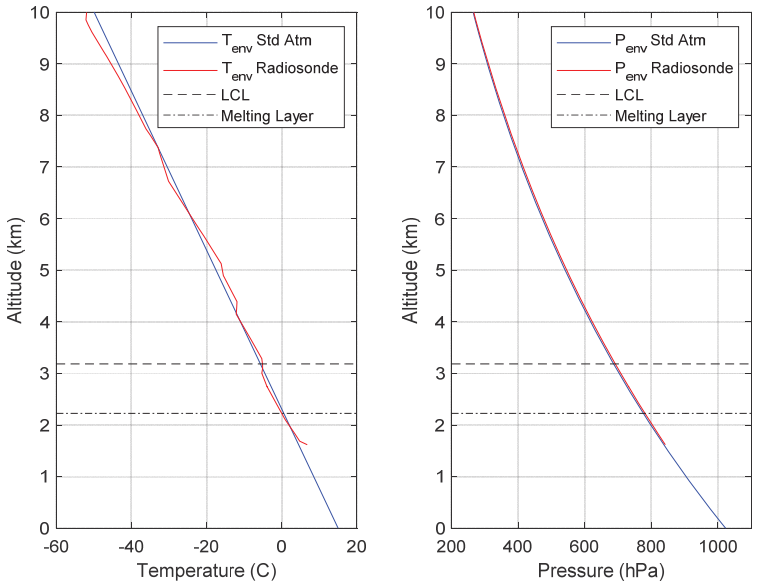

Figure 34. Comparison of Standard Atmosphere to Radiosonde Measurement (Temperature and Pressure) – Clear Conditions

Figure 35 shows the mixing ratio (left) and relative humidity (right). The mixing ratio measured by radiosonde was significantly less than the mixing ratio of the Standard Atmosphere model above the LCL and rapidly approached 0 g/kg. The relative humidity at the surface was 42%, which was greater than the surface measurement corresponding to a cloudy day. **This demonstrates that measurements of the relative humidity at the surface are not an accurate predictor of the presence of clouds.** The relative humidity was greater than 50% from about 2100 m through 2900 m, but decreased rapidly before the LCL, as did the mixing ratio. The maximum relative humidity was 58%. It is clear that there was much less water vapor in the atmosphere overall than on the cloudy day measurement.

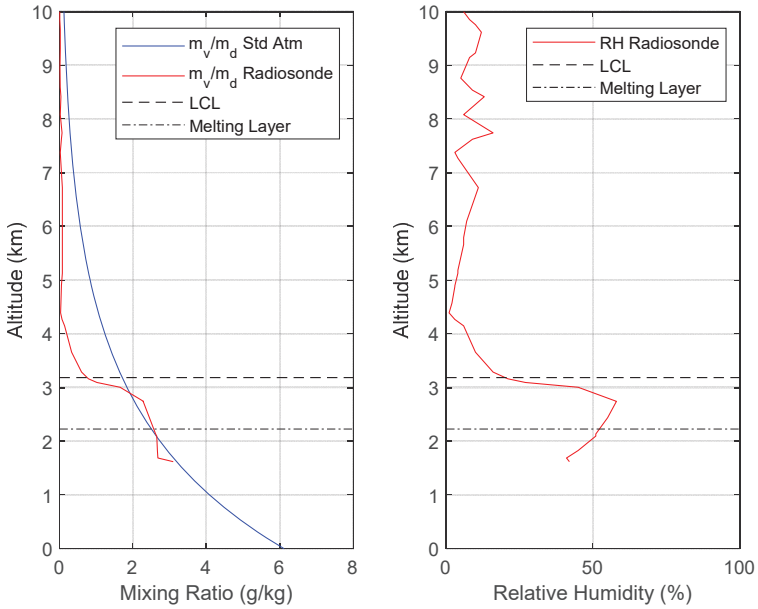

Figure 35. Comparison of Standard Atmosphere to Radiosonde Measurement (Mixing Ratio and Relative Humidity) – Clear Conditions

3.2.5.5 Adiabatic Lifting with Radiosonde Data - Cloudy

Next, we can use the measured surface conditions to define the states for an air parcel and then compute the temperature profile for adiabatic ascension. This can be compared to the measured radiosonde temperature profile to assess stability.

First, let's consider the cloudy day radiosonde measurements. Recall that the measured surface conditions were 9.6 °C, 838 hPa, and relative humidity of 37%. These define the initial conditions of the parcel. The parcel is then lifted at the dry adiabatic lapse rate to saturation, and subsequently at the moist adiabatic lapse rate. The results are shown in Figure 36. T_p tracked T_{env} up through the LCL, indicating neutral stability. Then, $T_{env} > T_p$, indicating a stable atmosphere. Therefore, any air parcel lifted to higher altitudes would be more dense than the surrounding air and would tend to sink back to the surface.

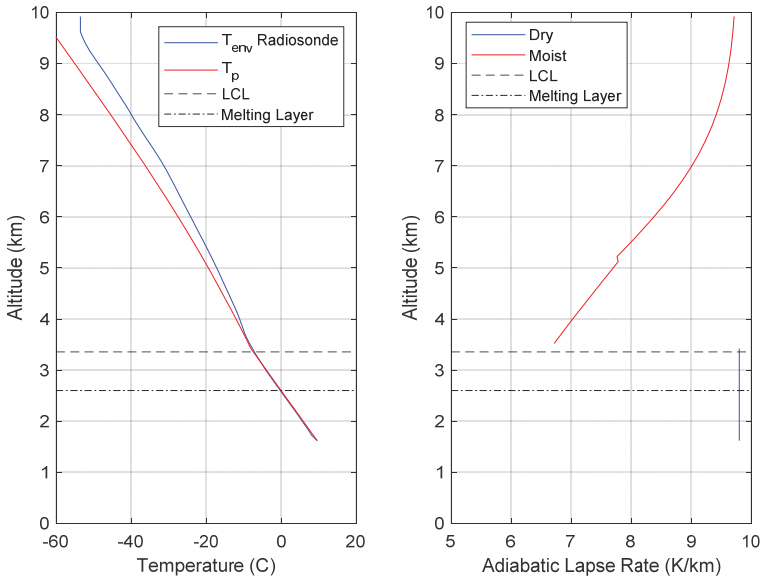

Figure 36. Comparison of an Air Parcel Being Lifted Adiabatically to Radiosonde Measurements (Temperature and Lapse Rate) – Cloudy Conditions

Figure 37 compares the mixing ratio and relative humidity data to the lifted parcel calculations. The radiosonde data tend to follow the adiabatic profile in both cases.

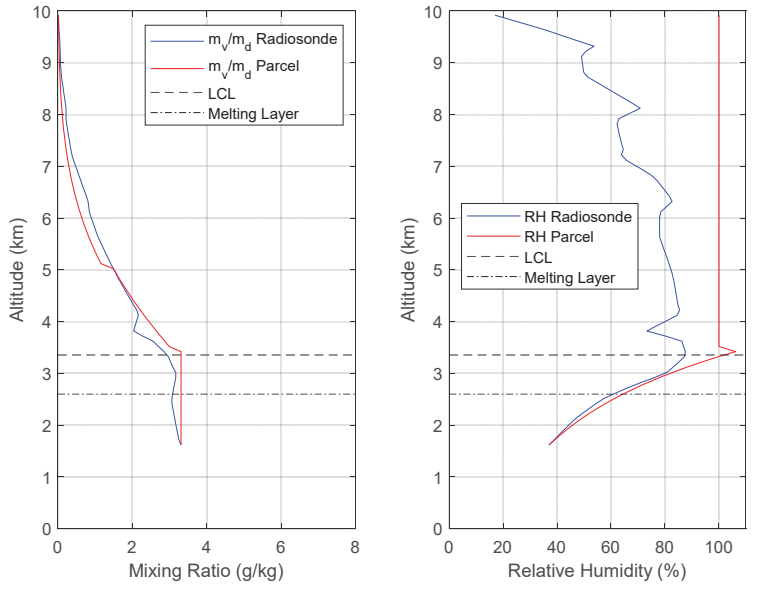

Figure 37. Comparison of an Air Parcel Being Lifted Adiabatically to Radiosonde Measurements (Mixing Ratio and Relative Humidity) – Cloudy Conditions

3.2.5.6 Adiabatic Lifting with Radiosonde Data - Clear

Now, let's consider radiosonde data for a clear day. Recall that the measured surface conditions were 6.8 °C, 842 hPa, and relative humidity of 42%. The results are shown in Figure 38. T_p tracked T_{env} up through ~2500 m (below the LCL), indicating neutral stability. Then, $T_{env} > T_p$, indicating a stable atmosphere.

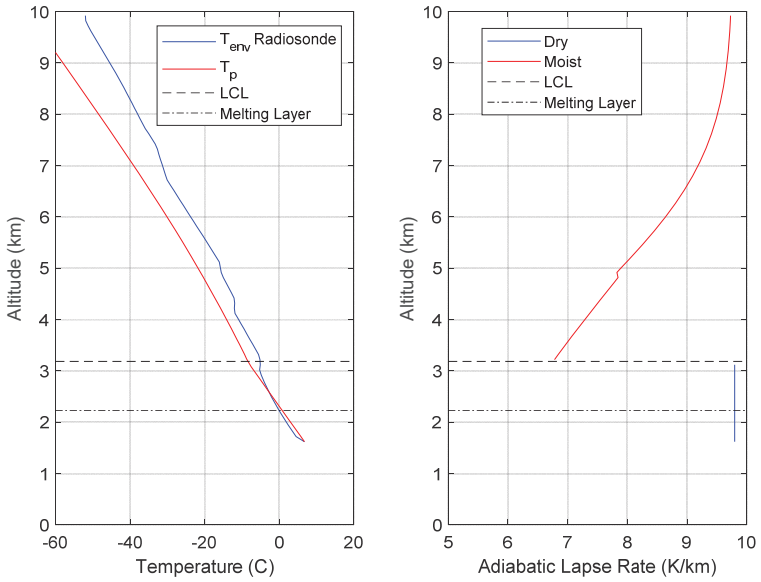

Figure 38. Comparison of an Air Parcel Being Lifted Adiabatically to Radiosonde Measurements (Temperature and Lapse Rate) – Clear Conditions

Figure 39 compares the mixing ratio and relative humidity data to the lifted parcel calculations. In this case, the radiosonde data did not follow the adiabatic profiles, as expected.

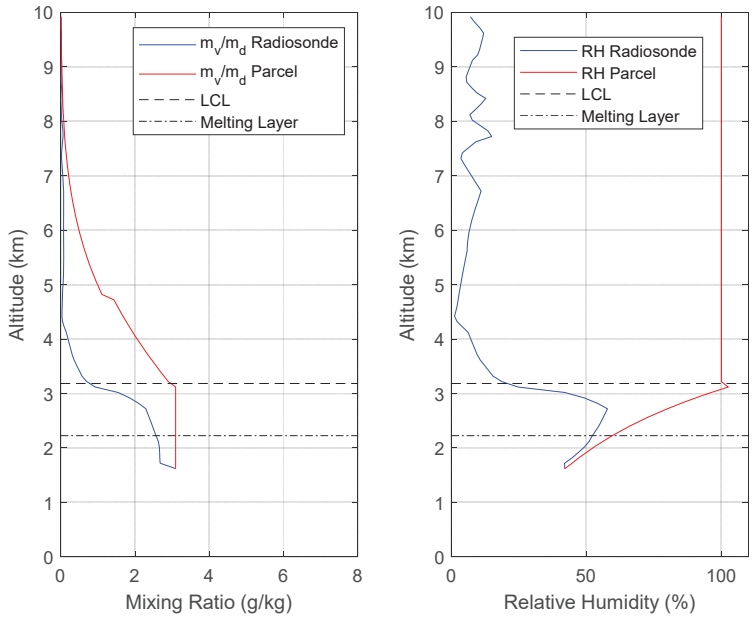

Figure 39. Comparison of an Air Parcel Being Lifted Adiabatically to Radiosonde Measurements (Mixing Ratio and Relative Humidity) – Clear Conditions

3.2.5.7 Cloud Extinction Coefficients

Now that we can estimate the temperature profile for a cloud that begins at the LCL and extends for an indeterminate thickness, we can calculate the liquid extinction coefficient, κ_L, (Eq. (116)) and/or ice extinction coefficient, κ_I, (Eq. (117)) as appropriate. To illustrate, let's start with the Standard Atmosphere model. Recall that initial conditions are T_{p_0} = 15 °C, P_{p_0} = 1023.2 hPa, and ϕ_{p_0} = 58.5%. The results are shown in Figure 40 (right) for f_1 = 72.5 GHz and f_2 = 82.5 GHz. The values of κ_L are about 3-4 (dB/km)/(g/m^3), and κ_I are about 0.01 (dB/km)/(g/m^3), which are consistent with the results in Figure 25. Note that the transition from κ_L to κ_I occurs at about 4800 m. Note that the difference in altitude between 4800 m and the LCL is about 3700 m.

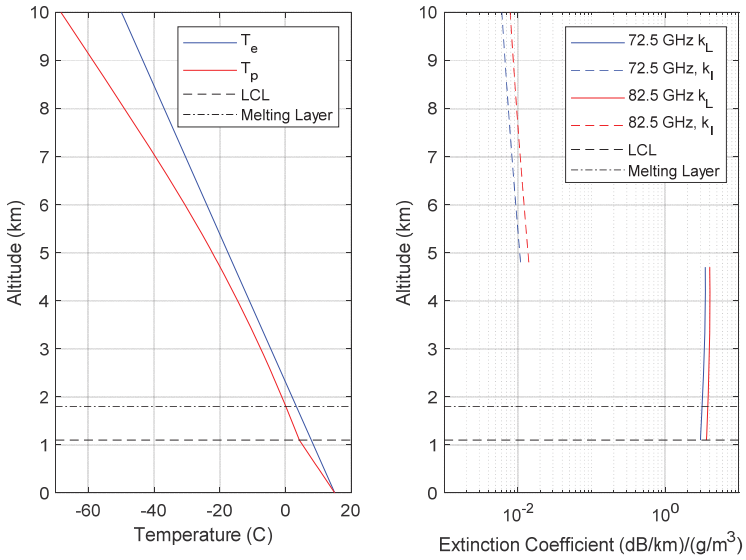

Figure 40. Extinction Coefficients Assuming Adiabatic Expansion Using Standard Atmosphere for 72.5 GHz and 82.5 GHz

Figure 41 shows the extinction coefficients computed using the radiosonde profile for a cloudy day. Values for κ_L are between 3-4 (dB/km)/(g/m^3), and κ_I are about 0.01 (dB/km)/(g/m^3), which is consistent with the Standard Atmosphere results. Recall that LCL is at about 3356 m. The abrupt transition to κ (i.e., T_p < 20 °C) is slightly higher (at 5000m) than for the Standard Atmosphere model (at 4700 m). Note that the difference in altitude between 5000 m and the LCL is about 1644 m, much less than in the case of the Standard Atmosphere model.

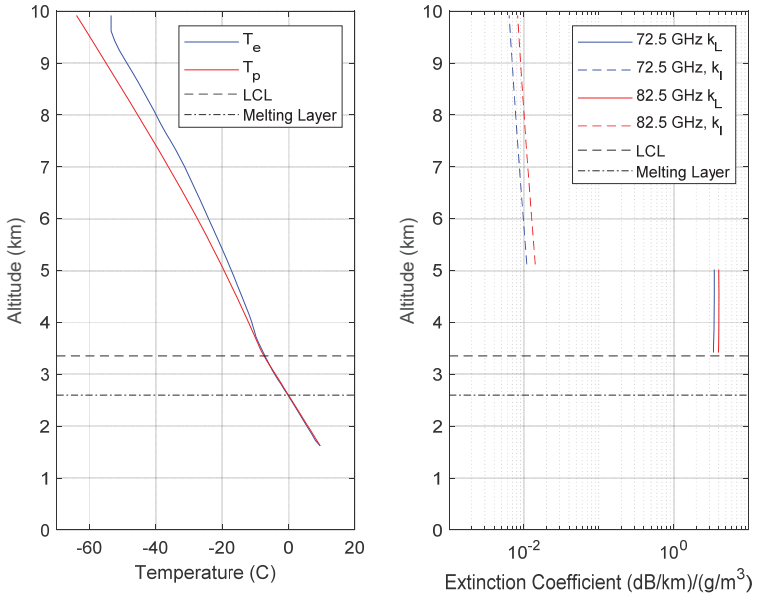

Figure 41. Extinction Coefficients Assuming Adiabatic Expansion Using Radiosonde Data for 72.5 GHz and 82.5 GHz

3.2.5.8 Liquid Water Content

Next, we consider the typical liquid water content (LWC), m_L, of various clouds as defined in Eq. (112). Data can be found in the literature for various cloud types and conditions [38 - 42]. Table 8 provides representative values for illustrative purposes. Cloud base is relative to the surface altitude (i.e., for Albuquerque, New Mexico, the surface altitude is approximately 1620 m above sea level, so fog would normally occur between 1620 m – 1670 m). Estimates of cloud characteristics have been derived over the years from sondings (i.e., weather balloons), radiometers, and satellites. Cloud data generally assumes non-precipitating clouds. The LWC varies both horizontally and vertically through clouds. Cloud thickness tends to follow a log-normal distribution, where thin clouds are common and the frequency-of-occurrence rolls off with increasing thickness.

Table 8. List of Cloud Type and Approximate Liquid Water Density

Cloud Type	Cloud Base	Thickness	LWC (g/m^3)	Mode Radius of Distribution (μm)
Haze	0 m	1500 m / 4921 ft	0.001	0.05
Thin Fog	0 m	50 m / 164 ft	0.05	20
Medium Fog	0 m	50 m / 164 ft	0.15	20
Heavy Fog	0 m	50 m / 164 ft	0.50	20
Low Lying Stratus	500 m / 1640 ft	100 m / 328 ft	0.25	10
Stratus	600 m / 1969 ft	100 m / 328 ft	0.25	10
Fair Weather Cumulus	700 m / 2297 ft	200 m / 656 ft	0.50	10
Cumulus Congestus	700 m / 2297 ft	400 m / 1312 ft	0.80	20
Cumulonimbus	700 m / 2297 ft	8000 m / 26247 ft	1.00	20
Nimbostratus	700 m / 2297 ft	1000 m / 3281 ft	1.10	20
Altostratus	2000 m / 6562 ft	100 m / 328 ft	0.25	10
Altocumulus	2000 m / 6562 ft	200 m / 656 ft	0.30	20
Cirrostratus	7000 m / 22966 ft	1000 m / 3281 ft	0.10	40
Cirrus	8000 m / 26247 ft	1000 m / 3281 ft	0.10	40
Cirrocumulus	9000 m / 29528 ft	1000 m / 3281 ft	0.10	40

3.2.5.8.1 Decker Model

In this section, we consider the Decker model to estimate the cloud LWC [43]. The Decker model was developed about 1977 to improve the correlation of radiometer retrieval algorithms to measured radiosonde data. It was developed for thin (less than 600 m), non-precipitating clouds. It assumes that the LWC is constant throughout the cloud layer. Figure 42 presents three LWC models / profiles. The profile on the left varies from 0.05 – 0.2 g/m^3, seemingly for cirrus clouds. The middle profile varies from 0.1 – 0.4 g/m^3, which would correlate to status clouds. The profile on the right varies from 0.2 – 0.8 g/m^3, which would seem reasonable for cumulous clouds. The presence of clouds and cloud thickness are inferred from profiles of the relative humidity generated by microwave radiometer measurements. The Decker model assumes that a cloud is present in the atmosphere if the measured radiometer profile indicates a relative humidity of 95% or more at some altitude. Some studies showed improved results by modifying this threshold parameter to

90%. The cloud thickness is determined by the altitude at which the relative humidity drops below the threshold. To illustrate, if the profile of a stratus cloud indicated RH ≥ 95% from 600 m to 900 m above the surface, then cloud thickness would be 300 m and the LWC would be ~0.25 g/m^3 (blue dashed line in Figure 42).

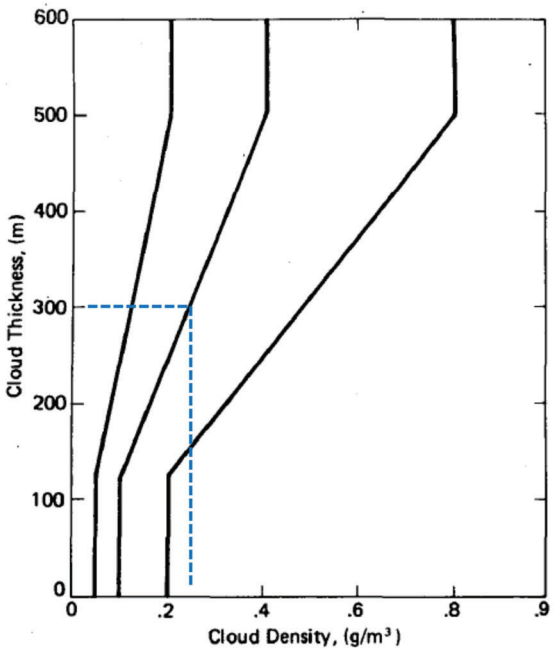

Figure 42. Decker Cloud Thickness / Liquid Water Content Estimation Models

3.2.5.8.2 Salonen Model

The Salonen model also provides an estimate of the LWC [44]. The Salonen model identifies the presences of clouds based a "critical" relative humidity function, RH_c, given as:

$$RH_c = 1 - \alpha\sigma(1-\sigma)[1+\beta(\sigma-0.5)], \tag{164}$$

where

$$\sigma = \frac{p_t(h)}{p_0} \text{ (hPa/hPa)}, \tag{165}$$

where p_t is the total atmospheric pressure as a function of altitude and p_0 is the pressure at the surface. The two empirical parameters are defined as $\alpha = 1.0$ and $\beta = \sqrt{3}$, and determined by curve-fitting measured data. For reference, RH_c is plotted in Figure 43 for the Standard Atmosphere. This model can be tuned using local profile measurements. Studies documented in published literature suggest that this model provides more accurate predictions of the occurrence of a cloud (i.e., fewer false positives and fewer missed detections relative to the Decker model).

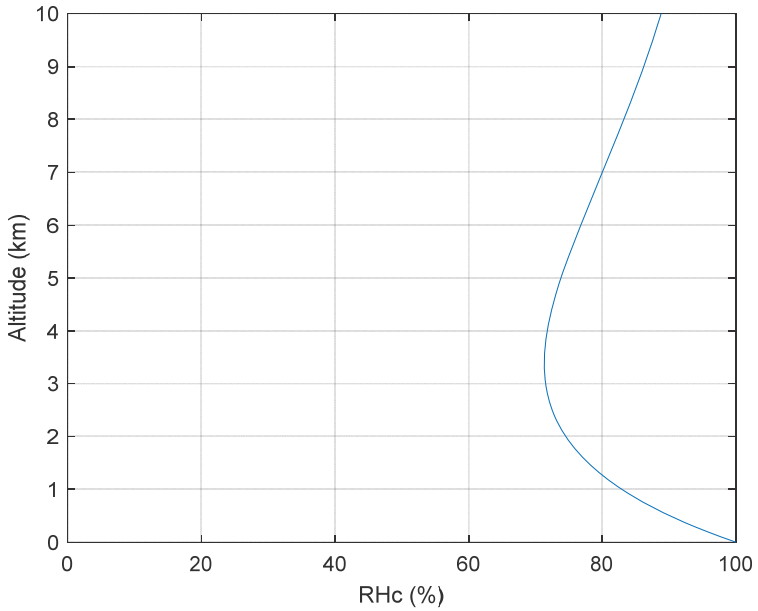

Figure 43. Illustration of RH_c for Salonen Model Using the Standard Atmosphere Model

If the measured relative humidity at a given altitude is greater than the corresponding value of the critical relative humidity, then the LWC for that altitude is estimated as:

$$LWC = TWC(h,T) * f_w(T), (\text{g/m}^3) \tag{166}$$

where *TWC* is the total water content (as opposed to ice content) and is a function of altitude and temperature, given as:

$$TWC(h,T) = \begin{cases} w_0 \left(\frac{h-h_b}{h_r}\right)^a (1+cT) & T \geq 0\ ^\circ\text{C} \\ w_0 \left(\frac{h-h_b}{h_r}\right)^a (\exp(cT)) & T < 0\ ^\circ\text{C} \end{cases} (\text{g/m}^3) \tag{167}$$

and f_w is the fraction of cloud liquid estimated based on temperature as:

$$f_w(T) = \begin{cases} 1, & T \geq 0\ ^\circ\text{C} \\ 1 + {}^{T}/_{20}, & -20 \leq T < 0\ ^\circ\text{C} \\ 0, & T < -20\ ^\circ\text{C} \end{cases}. \tag{168}$$

This model provides four tunable parameters (w_0, a, c, h_r). Values documented in the literature are $w_0 = 0.14$ g/m^3, $a = 1.4$, $c = 0.041$ °C^{-1}, and $h_r = 1500$ m. The cloud base height is denoted as h_b, and h denotes altitude. Published studies suggest that the Salonen model identifies low clouds better than the Decker model, but provides poorer results in the middle troposphere.

To illustrate the Salonen model, let's consider our prior radiosonde measurements for a cloudy day in January measured in Albuquerque, NM. Figure 44 (left) plots the critical humidity, RH_c, and the measured relative humidity profile. The measured relative humidity exceeded RH_c at 3000 m, which is above the melting layer but below the lifted condensation level. Thus, the assumed cloud

base, h_b, is taken to be 3000 m. Then, $RH > RH_c$ until ~6900 m, with the exception of a dip at 3800 m. Thus, the cloud thickness is about 3900 m. Figure 44 (center) plots the weighting function, f_w, which is intended to account for the liquid-to-ice transition, -20 °C ≤ T < 0 °C. Figure 44 (right) plots the estimated LWC (g/m^3) profile. The LWC varies with altitude and was non-zero if the measured RH > RH_c and if f_w > 0. Note that the maximum value of the LWC profile was 0.024 g/m^3, which is about an order of magnitude less than typical cloud LWC values given in Table 8 and less than values estimated by the Decker model. The parameters can easily be adjusted if a reasonable optimization metric is defined.

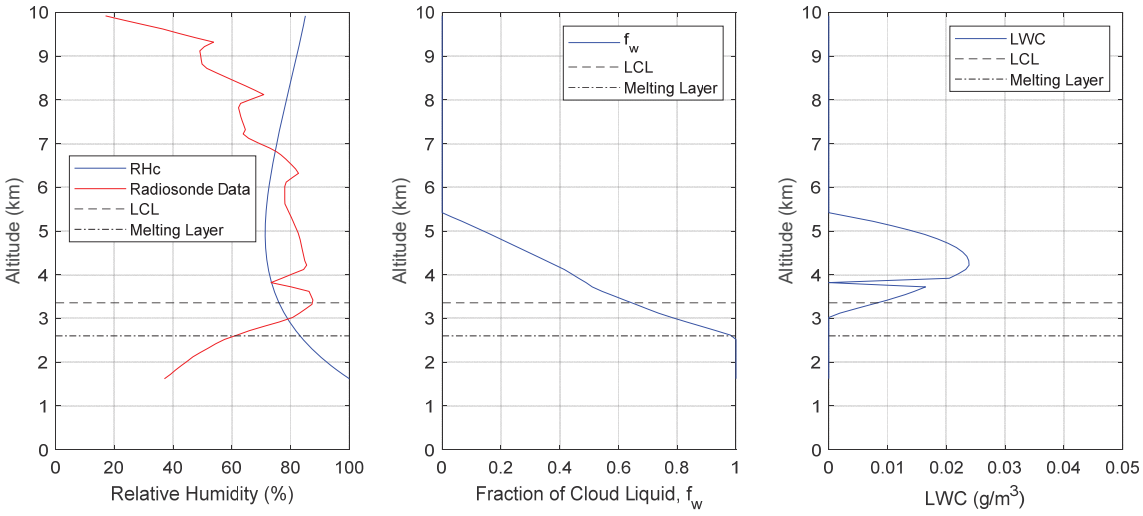

Figure 44. Illustration of LWC for Salonen Model Using Radiosonde Measurement

3.2.5.8.3 Mattioli Model

Mattioli *et al.* introduced variations to the Salonen model that attempted to account for entrainment of dryer air, mixing, precipitation fallout, and radiative heating/cooling [45]. First, coefficients for the critical humidity function were re-computed using new ceilometer data to identify the cloud base height, and a nonlinear curve-fit to match vertical profile data from radiosondes, which yielded α = 0.59 and β = 1.37. For reference, the revised RHc is plotted in Figure 45 for the Standard Atmosphere. The Mattioli curve for RH_c is more conservative than the Salonen threshold.

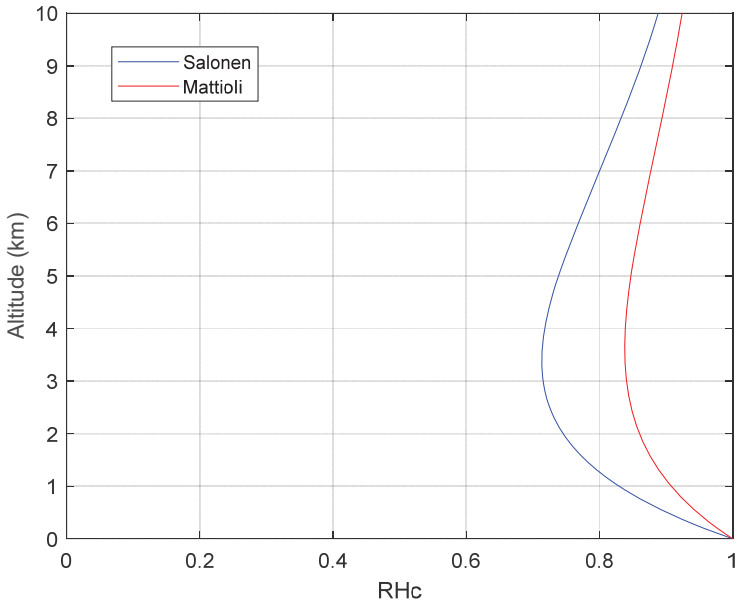

Figure 45. Comparison of RH_c for the Salonen Model and Mattioli Model Using the Standard Atmosphere Model

Additionally, the Mattioli model included revised expressions and parameters for the LWC:

$$LWC = c \cdot z^a \cdot (1 - z^{a+1})^b \cdot p_w(T), \ (\text{g/m}^3), \tag{169}$$

where

$$z = \frac{h - h_b}{\Delta h_{cl}} \ (\text{km/km}) \tag{170}$$

is the altitude above the cloud base, h_b, normalized by the estimated cloud thickness, Δh_{cl}. Parameters $\{a, b, \text{c}\}$ are calculated as:

$$a = \frac{z}{1.5} \ (\text{unitless}) \tag{171}$$

$$b = 1.5 + \frac{z}{1.5} \ (\text{unitless}) \tag{172}$$

$$c = \begin{cases} 0.8 \cdot \frac{RH(z)}{100} \cdot \Delta h_{cl} & \Delta h_{cl} \leq 0.1\ km \\ 1.46 \cdot \frac{RH(z)}{100} \cdot \Delta h_{cl} & 0.1\ km < \Delta h_{cl} \leq 0.6\ km \\ 0.74 \cdot \frac{RH(z)}{100} \cdot \Delta h_{cl} & \Delta h_{cl} > 0.6\ km \end{cases} \ (\text{g/m}^3). \tag{173}$$

Here, the relative humidity must be divided by 100 to convert from a percent to decimal, and Δh_{cl} is defined in units of km. For example, if RH = 85% and Δh_{cl} = 1300 m, then c = 0.74(0.85)(1.3) = 0.82 g/m^3. The fraction of cloud liquid, p_w, is calculated as:

$$p_w(T) = \begin{cases} 1, & T \geq 0\ ^\circ\text{C} \\ 1 - \left(T/35\right)^2, & -35 \leq T < 0\ ^\circ\text{C} \\ 0, & T < -35\ ^\circ\text{C} \end{cases}. \quad (174)$$

where the range for mixed liquid/ice particulates has been expanded from {-20 – 0 °C} to {-35 – 0 °C}.

To illustrate the Mattioli model, let's consider our prior radiosonde measurements for a cloudy day in January measured in Albuquerque, NM. Figure 46 (left) plots the critical humidity, RH_c, and the measured relative humidity profile. The measured relative humidity exceeded RH_c at 3300 m, which is consistent with the lifted condensation level. Thus, the assumed cloud base, h_b, is taken to be 3300 m. The estimated cloud thickness is taken to be Δh_{cl} = 1300 m based on the altitudes at which $RH > RH_c$. Figure 46 (center) plots the weighting function, p_w, which is intended to account for the liquid-to-ice transition -35 °C ≤ T < 0 °C. Figure 46 (right) plots the estimated LWC (g/m^3) profile. Note that although there were fewer points (i.e., altitudes) for which $RH > RH_c$, the LWC at those points was much greater than in the case of the Salonen model. The maximum value of the LWC profile was 0.8074 g/m^3, which is more consistent with typical cloud LWC values given in Table 8 and those predicted by the Decker model.

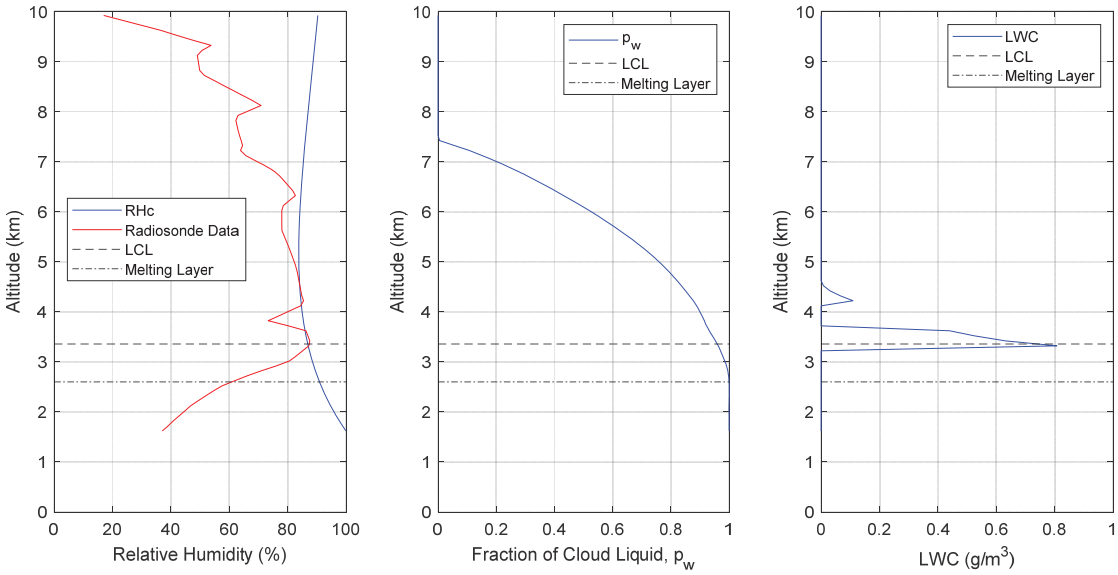

Figure 46. Illustration of LWC for Mattioli Model Using Radiosonde Measurement

3.2.5.9 Cloud Zenith Optical Thickness

Given the liquid and ice extinction coefficients and assuming a value for LWC, we can now calculate the zenith optical thickness (i.e., power attenuation or power absorption) of a cloud as a function of thickness. To illustrate, let's begin with the Standard Atmosphere model (LCL = 1100

m) and assume a cumulous cloud with m_L = 0.5 g/m^3. The cloud volume absorption coefficient was defined in Eq. (115). Figure 47 plots the zenith optical thickness as a function of cloud thickness (staring from LCL). The zenith optical thickness for such a cloud with thickness of 100 m is 0.15 dB at 72.5 GHz and 0.18 dB at 82.5 GHz. These values increase in proportion to layer thickness, since we assumed m_L to be constant. In the event that our cumulous cloud achieves a depth (thickness) of 1000 m, the power attenuation resulting from the cloud would be about 1.56 dB at 72.5 GHz and 1.87 dB at 82.5 GHz.

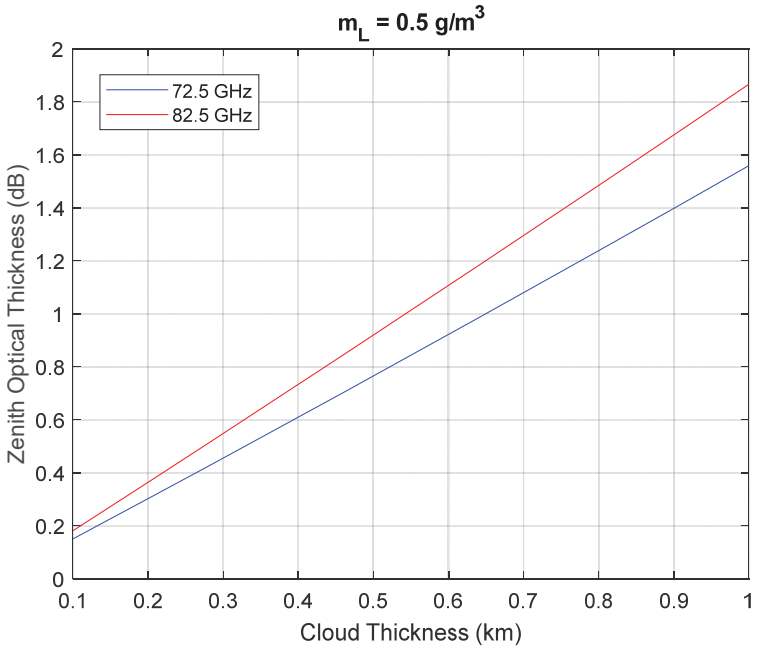

Figure 47. Cloud Zenith Optical Thickness Using Standard Atmosphere for 72.5 GHz and 82.5 GHz (Cumulous)

Now, let's consider a non-precipitating cumulonimbus cloud that extends from the LCL to the troposphere (~10000 m) with m_L = 1.0 g/m^3. The zenith optical thickness is given in Figure 48. The total zenith optical thickness of the cloud for the entire ~ 9 km was computed to be 12.23 dB at 72.5 GHz and 14.35 dB at 82.5 GHz. The abrupt transition between liquid droplets and frozen droplets is noticeable at 3700 m. There is no significant contribution to the zenith optical thickness above the transition. Note that in real clouds, the transition is less abrupt because there is potentially a mixed liquid / frozen layer between -40 °C < T_p < 0 °C.

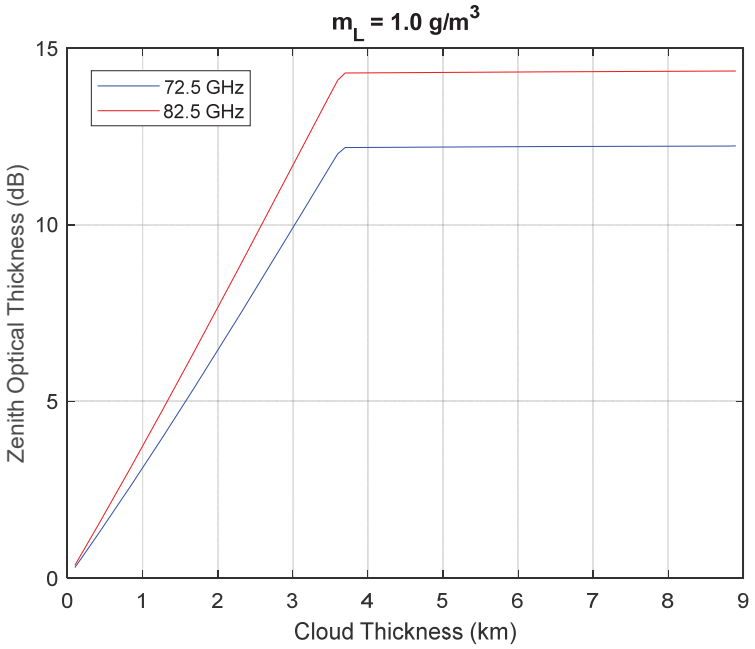

Figure 48. Cloud Zenith Optical Thickness Using Standard Atmosphere for 72.5 GHz and 82.5 GHz (Cumulonimbus)

It is reasonable to use a constant value for the LWC, although we know that the actual LWC varies throughout the cloud layer. This is illustrated in Figure 49. Recall from Figure 40 and Figure 41 that the liquid extinction coefficient, κ_L, is relatively constant through a cloud layer. Therefore, the optical thickness simply depends on the integrated value of the liquid water content for the cloud.

$$\tau_{cl} = \int_0^{h_{cl}} \kappa_{cl}\, dh \quad \text{dB}$$

$$\tau_{cl} = \int_0^{h_{cl}} (\kappa_L \cdot m_L)\, dh \quad \text{dB}$$

$$\tau_{cl} = \kappa_L \int_0^{h_{cl}} m_L\, dh \quad \text{dB}$$

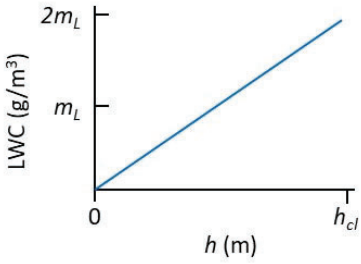

$$\tau_{cl} = \kappa_L m_L h_{cl} \quad \text{dB}$$

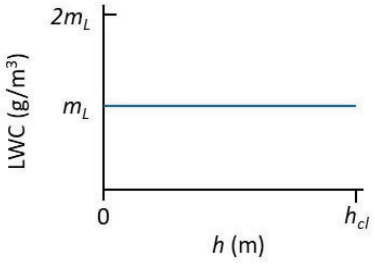

$$\tau_{cl} = \kappa_L m_L h_{cl} \quad \text{dB}$$

Figure 49. Illustration of Optical Thickness Calculation for Variable and Constant Liquid Water Content

Let's now consider the zenith optical thickness of a cumulus and cumulonimbus cloud using measured radiosonde data from the cloud day condition. Figure 50 presents the zenith optical thickness as a function of cloud thickness for the cumulous cloud $m_L = 0.5$ g/m^3. The zenith optical thickness for such a cloud with thickness of 100 m was computed to be 0.17 dB at 72.5 GHz and 0.20 dB at 82.5 GHz, slightly higher than computed for the Standard Atmosphere (simply the result of the variation of temperature). For a depth (thickness) of 1000 m, the zenith optical thickness was 1.73 dB at 72.5 GHz and 2.01 dB at 82.5 GHz, which is very close to the results from the Standard Atmosphere model.

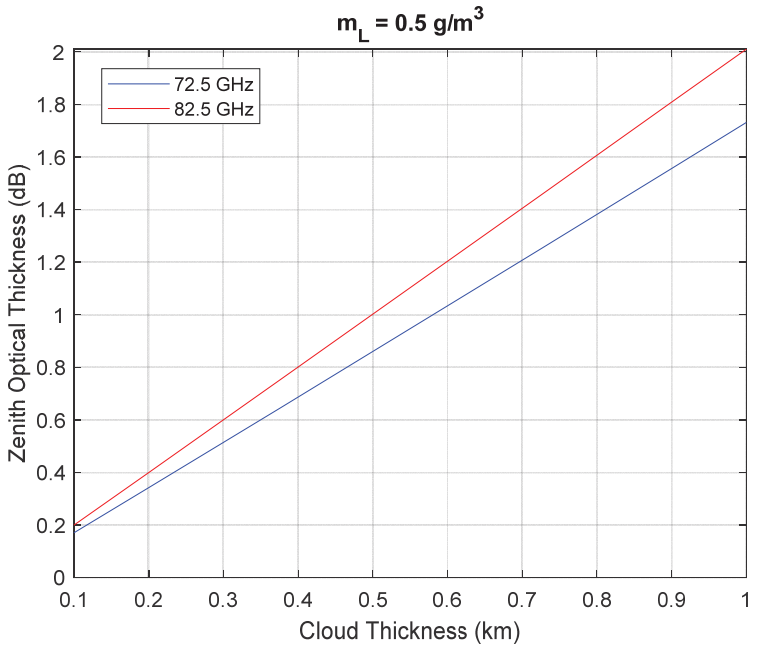

Figure 50. Cloud Zenith Optical Thickness Using Radiosonde Data for 72.5 GHz and 82.5 GHz (Cumulous)

Figure 51 shows the computed zenith optical thickness for a cumulonimbus cloud, $m_L = 1.0$ g/m^3. It is apparent that the transition from κ_L to κ_I occurs at about 1644 m – much sooner than in the case of the Standard Atmosphere model. Since the contribution from frozen cloud droplets is much less, the total zenith optical thickness (i.e., attenuation) was significantly reduced. The total zenith optical thickness of the cloud for the entire ~ 6.5 km was computed to be 5.78 dB at 72.5 GHz and 6.69 dB at 82.5 GHz.

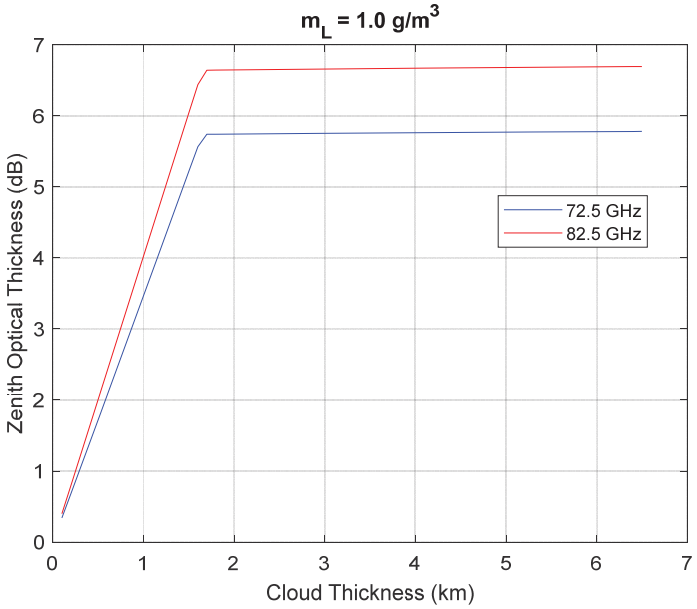

Figure 51. Cloud Zenith Optical Thickness Using Radiosonde Data for 72.5 GHz and 82.5 GHz (Cumulonimbus)

For reference, Figure 52 shows the cloud volume absorption coefficient (dB/km) as a function of LWC (g/m^3) for T_p = {-10, 0, 10} °C. Results are compared for f = 20 GHz and f = 72.5 GHz. Cloud volume absorption (i.e., specific attenuation) is more than an order of magnitude greater at 72.5 GHz than at 20 GHz over the range of LWC.

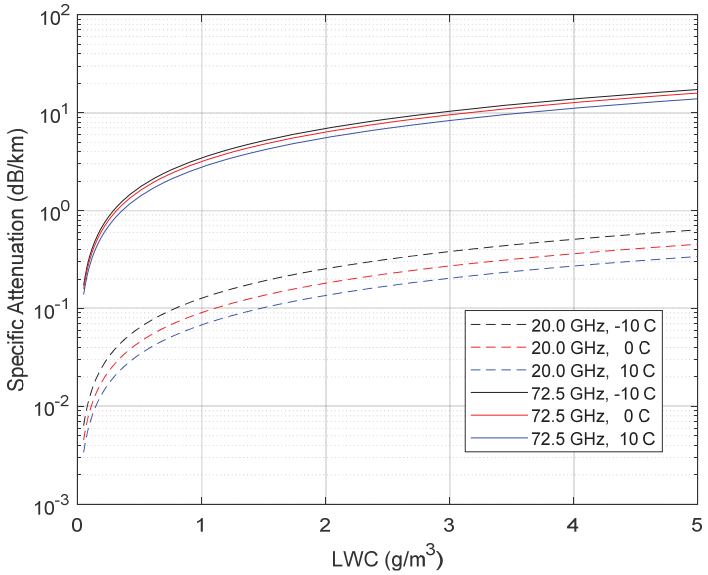

Figure 52. Cloud Volume Absorption Coefficient as a Function of LWC, Temperature, and Frequency

3.2.5.10 Non-Zenith Propagation Path Length

The propagation path length through a cloud layer will depend on the type of cloud and the angle of arrival of the signal to and from the satellite. To illustrate, let's first consider a cloud with a very large base area and relatively small depth, such as a stratus cloud as depicted in Figure 53 (left). For an angle of arrival denoted as θ, the propagation path length, R, is calculated as:

$$R = (\Delta h_{cl})\sec\theta \text{ (m)}, \tag{175}$$

where Δh_{cl} is the cloud thickness (i.e., depth). In this case, the propagation path is greater than the cloud thickness. On the other hand, let's consider a taller cloud, such as a cumulonimbus type cloud, which typically have much less base area than stratus clouds, as depicted in Figure 53 (right). In this case, the propagation path length is calculated as:

$$R = (\text{Base})\csc\theta \text{ (m)}, \tag{176}$$

where "Base" is the diameter of the cloud base, which is on the order of 5 km for a cumulonimbus cloud, but may vary greatly. In this case, the propagation path is less than the cloud thickness for $\theta > 0°$. Figure 53 (right) depicts the worse-case geometry, where R is maximum – the propagation path transverses the entire cloud width. Signal attenuation due to the cloud will vary as the cloud drifts across the propagation path. Thus, path length and attenuation will fluctuate over time.

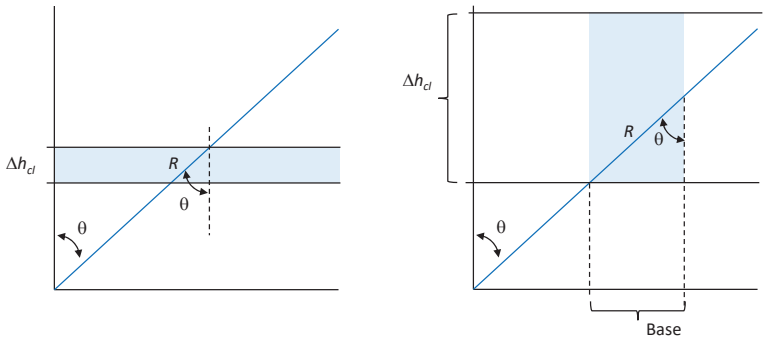

Figure 53. Illustration of Non-Zenith Propagation Path Through a Cloud

Figure 53 shows the physical propagation path, but since clouds are not homogeneous, an effective propagation path is often reported in the literature. There is significant variability and uncertainty in the effective cloud propagation path, since cloud development is dynamic and clouds are constantly moving. Further, we know that the liquid water content varies throughout the cloud, as does the temperature. As will be shown later, estimating cloud attenuation as a function of time is problematic. Therefore, cloud attenuation effects must be modeled statistically – more specifically, using mean, maximum value, and probability of exceedance curves.

3.2.6 Precipitation

As noted in the introduction, link availability is directly dependent upon rain-fade and will drive the necessary power / aperture requirements. Rain attenuation (absorption and scattering) is the dominant source of signal fading and L_{atm} at W/V-band. Raindrops are typically two orders of magnitude larger in diameter than cloud droplets. In general, Mie scattering theory should be used for computing absorption and scattering in a rain volume. The solutions for the scattering and extinction efficiencies were given in Eq. (72) and Eq. (73).

3.2.6.1 Drop Size Distribution

Drop-size distributions for rain have been reported by serval investigators, including Laws and Parsons [46], Wexler [47], Marshall and Palmer [48], and Best [49]. Among these, the most widely used in the literature are the Law-Parsons and Marshall-Palmer distributions. Marshall-Palmer developed the following expression for the distribution of drop sizes (assuming spherical droplets):

$$p(d) = N_0 \exp(-bd) \text{ (m}^{-4}\text{)}, \tag{177}$$

where $p(d)$ is the number of drops of diameter d per unit volume of atmosphere, per unit drop-diameter interval, N_0 = 8.0e6 m^{-4}, and b is related to the rainfall rate, R_r (mm/hr) as:

$$b = 4100 \cdot R_r^{-0.21}. \tag{178}$$

For a given droplet diameter, d_i, we can calculate the total volume occupied by $p(d_i)$ drops:

$$V_i = p(d_i)\left(\frac{4}{3}\pi r^3\right) = p(d_i)\left(\frac{\pi}{6}d^3\right) \quad \text{(m}^3\text{)}. \tag{179}$$

The total volume of all water droplets, N, in a unit volume of atmosphere is the sum over each diameter:

$$V_T = \sum_{i=1}^{N} V_i \quad \text{(m}^3\text{)}. \tag{180}$$

We can estimate the frequency-of-occurrence of each diameter by calculating the ratio V_i/V_T, which is presented in Figure 54. Figure 54 suggests that drizzle (0.25 mm/hr) and light rain (2.5 mm/hr) conditions produce rain drops of smaller diameter than heavy rain (50 mm/hr) and tropical downpour (150 mm/hr) conditions. Figure 54 also suggests that there is less variability of drop size at low rain-rates in comparison to higher rain rates. Figure 54 shows that drop size diameters for rain vary from ~0.1 mm up to ~5 mm.

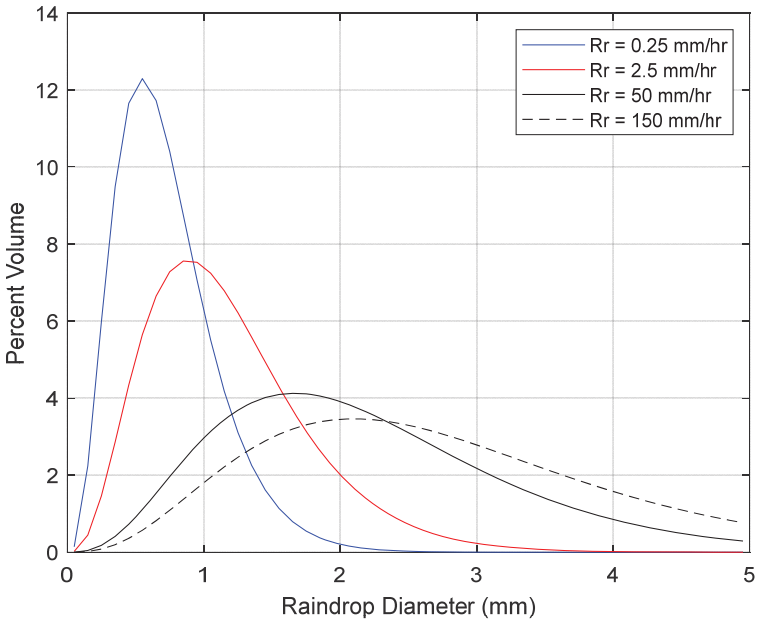

Figure 54. Illustration of Rain Drop Size Distributions for Various Rain Rates

There are problems with this model as noted by de Wolf [50]. Olsen *et al.* suggested that it is not consistent with evaluation of the rain-rate (experimental error) [51]. Additionally, this model gives a maximum value for droplets of zero diameter. There have been revisions to the model. Prior research demonstrates that raindrop size distributions exhibit large variations for the same location, rain type, and rain rate. Consequently, drop size distribution models should be regarded as representative of average, rather than individual, rainfall conditions [52].

3.2.6.2 Mie Solution for Absorption and Scattering

Now that we understand reasonable diameters for rain drops, let's consider the absorption, scattering, and extinction coefficients. Let's assume a rain drop with T = 15 °C and radius r = 0.5 mm or diameter d = 1 mm (typical for light rain conditions), and an EM plane wave with frequency f = 82.5 GHz. The corresponding wavelength is λ_0 = 3.6e-3 m (3.6 mm). The normalized circumference is χ = 0.8639. The dielectric constant is ε = 8.1994 – j13.7605 and n = 3.4798 – j1.9772. The value of $|n\chi|$ = 3.4577. Since $|n\chi| > 1$, the Rayleigh approximation does not apply to this frequency range and particle size.

The first five Mie coefficients were computed and are shown in Figure 55. The Mie solution yields ξ_a = 1.5918, ξ_s = 1.4023, and ξ_e = 2.9941. This demonstrates that scattering cannot be ignored for this frequency range and particle size (i.e., since ξ_a is very similar in value to ξ_s).

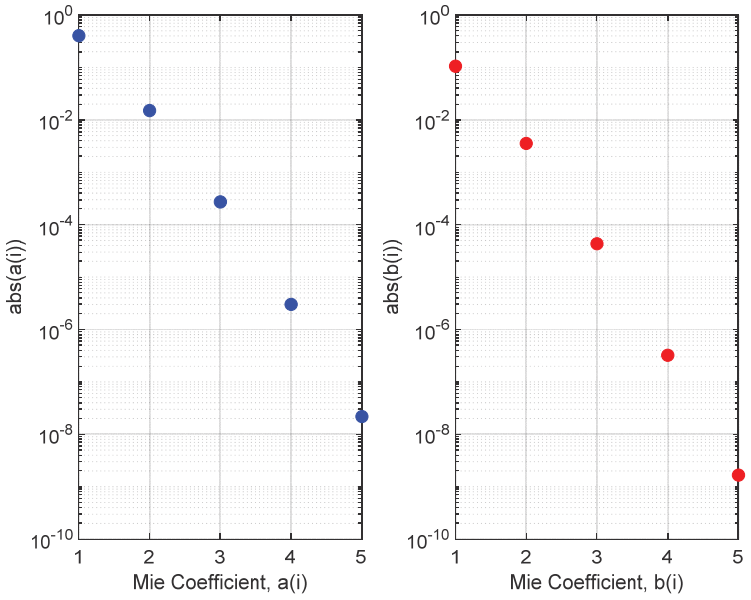

Figure 55. Illustration of Mie Coefficient for Extinction Efficiency Calculation (Rain)

3.2.6.3 Extending to Many Drops

3.2.6.3.1 Rain Volume Extinction Coefficient

Now, we consider a volume containing a mixture of dry air, water vapor, and many rain drops. For modeling purposes, we will assume that when many rain drops exist in a unit volume of atmosphere, those drops do not interact with each other and shadowing does not occur. Thus, the total extinction cross section of a unit volume of air is equal to the sum of the extinction cross section of all individual droplets contained within the unit volume:

$$Q_{e_{Total}} = \sum_{i=1}^{N_v} Q_{e_i}(f,T,r), \tag{181}$$

where N_v is the number of rain drops in the unit volume, and the dependence of the extinction cross section Q_e on EM wave frequency, temperature, and drop radius is indicated. The ***rain volume extinction coefficient*** is defined as:

$$\kappa_{e_{rn}} = \int_{r_{min}}^{r_{max}} p(r) Q_e(r)\, dr \quad \text{(Np/m)}, \tag{182}$$

where $\{r_{\min}, r_{\max}\}$ represent the minimum and maximum droplet radii, which is analogous to the definition of cloud volume absorption coefficient in Eq. (105). Substituting $Q_e(r) = \pi r^2 \xi_e(r)$ yields:

$$\kappa_{e_{rn}} = \pi \int_{r_{min}}^{r_{max}} r^2 p(r) \xi_e(r)\, dr \quad \text{(Np/m)}. \tag{183}$$

For a given rain rate, R_r, we can estimate r_{min} and r_{max} from Figure 54. The Marshall-Palmer model (or a revised version) can be used to calculate $p(r)$. For a given temperature and frequency (which determine n and χ), we can calculate ξ_e over the range of r following Eq (73). Figure 56 shows the

rain volume extinction coefficients as a function of frequency assuming $T = 0$ °C for various rain-rates – drizzle (0.25 mm/hr), light rain (2.5 mm/hr), and heavy rain (50 mm/hr).

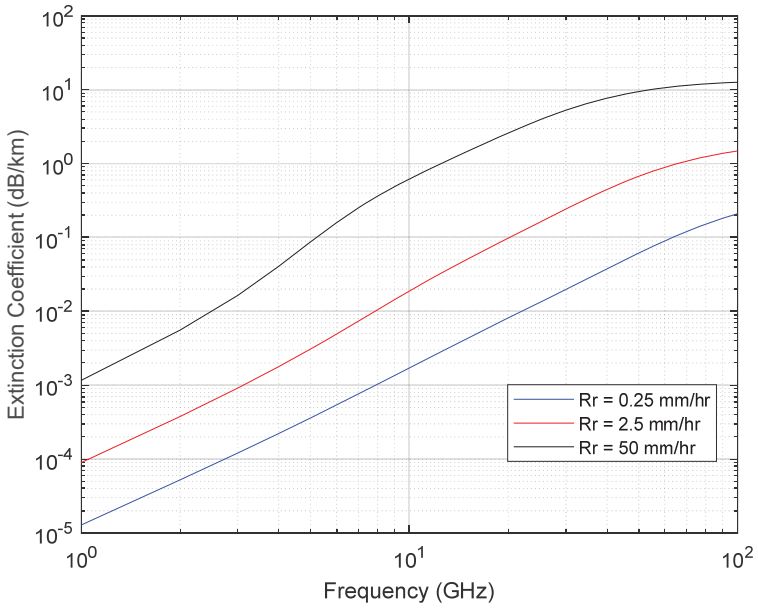

Figure 56. Rain Volume Extinction Coefficient Calculated Using Mie Solution and Marshall-Palmer Drop Size Distribution

3.2.6.3.2 ITU Model

The International Telecommunications Union (ITU) provides a power-law model for the rain volume extinction coefficient (dB/km) given as [53]:

$$\kappa_{e_{rn}} = k \cdot {R_r}^{\alpha} \text{ (dB/km)} \tag{184}$$

where

$$k = \frac{[k_H + k_V + (k_H - k_V)\cos^2\theta \cos 2\psi]}{2} \tag{185}$$

and

$$\alpha = \frac{[k_H\alpha_H + k_V\alpha_V + (k_H\alpha_H - k_V\alpha_V)\cos^2\theta \cos 2\psi]}{2k}. \tag{186}$$

Subscripts "*H*" and "*V*" denote horizontal and vertical polarizations, respectively. Angles θ and ψ are the path elevation relative to the horizon and the polarization tilt angle relative to the horizontal, where $\psi = 45°$ for circular polarization. Expressions for k_H, k_V, α_H, and α_V are parameterized functions of frequency given as:

$$k_{H/V} = 10\text{^}\left[\sum_{j=1}^{4}\left(a_j \exp\left[-\left(\frac{\log_{10} f - b_j}{c_j}\right)^2\right]\right) + m_k \log_{10} f + c_k\right] \quad (187)$$

$$\alpha_{H/V} = \sum_{j=1}^{5}\left(a_j \exp\left[-\left(\frac{\log_{10} f - b_j}{c_j}\right)^2\right]\right) + m_\alpha \log_{10} f + c_\alpha \quad (188)$$

where f is in GHz, and k and α are defined for horizontal and vertical polarizations. Parameters a_j, b_j, c_j, m_k, c_k, m_α, and c_α were determined from curve-fitting and provided in ITU P.838-3 and given in Table 9, Table 10, Table 11, and Table 12 for reference. The calculated rain volume extinction coefficients are provided in Figure 57 along with the coefficients computed with the Mie solution with the Marshall-Palmer drop size distribution superimposed for comparison.

Table 9. Coefficients for k_H

j	a_j	b_j	c_j	m_k	c_k
1	-5.33980	-0.10008	1.13098	-0.18961	0.71147
2	-0.35351	1.26970	0.45400		
3	-0.23789	0.86036	0.15354		
4	-0.94158	0.64552	0.16817		

Table 10. Coefficients for k_V

j	a_j	b_j	c_j	m_k	c_k
1	-3.80595	0.56934	0.81061	-0.16398	0.63297
2	-3.44965	-0.22911	0.51059		
3	-0.39902	0.73042	0.11899		
4	0.50167	1.07319	0.27195		

Table 11. Coefficients for α_H

j	a_j	b_j	c_j	m_α	c_α
1	-0.14318	1.82442	-0.55187	0.67849	-1.95537
2	0.29591	0.77564	0.19822		
3	0.32177	0.63773	0.13164		
4	-5.37610	-0.96230	1.47828		
5	16.1721	-3.29980	3.43990		

Table 12. Coefficients for α_V

j	a_j	b_j	c_j	m_α	c_α
1	-0.07771	2.33840	-0.76284	-0.053739	0.83433
2	0.56727	0.95545	0.54039		
3	-0.20238	1.14520	0.26809		
4	-48.2991	0.791669	0.116226		
5	48.5833	0.791459	0.116479		

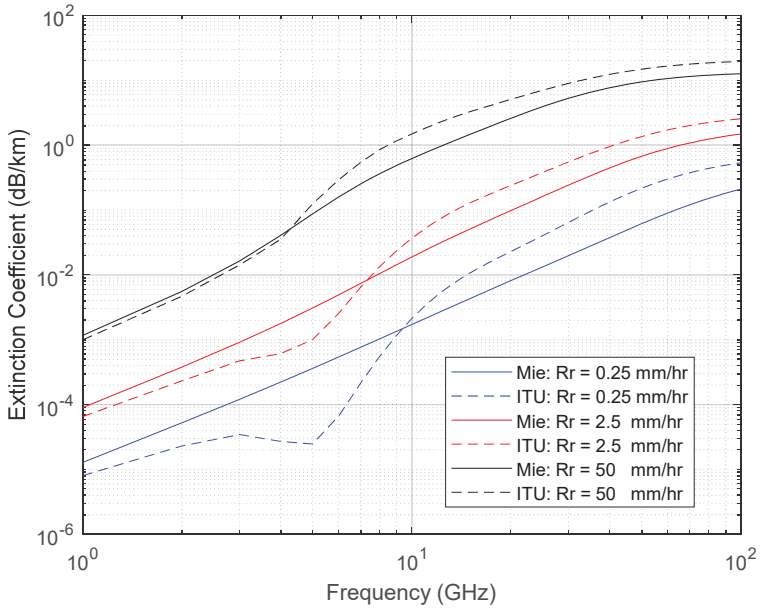

Figure 57. Comparison of Rain Volume Extinction Coefficient Calculated Using Mie Solution and Marshall-Palmer Drop Size Distribution to the Coefficients Calculated with ITU P.838-3 Model

3.2.6.3.3 Olsen Model

Finally, let's consider the Olsen model for rain volume extinction coefficients [51, 54]. It too is a power-law model generated by regression analysis, but more simple to calculate than the ITU model. It is expressed as:

$$\kappa_{e_{rn}} = k \cdot {R_r}^{\alpha} \text{ (dB/km)} \tag{189}$$

where

$$k = \begin{cases} (6.39e-5)f^{2.03} & f < 2.9 \text{ GHz} \\ (4.21e-5)f^{2.42} & 2.9 \le f < 54 \text{ GHz} \\ (4.09e-2)f^{0.699} & 54 \le f < 180 \text{ GHz} \\ (3.38)f^{-0.151} & f \ge 180 \text{ GHz} \end{cases} \tag{190}$$

and

$$\alpha = \begin{cases} 0.851f^{0.158} & f < 8.5 \text{ GHz} \\ 1.41f^{-0.0779} & 8.5 \leq f < 25 \text{ GHz} \\ 2.63f^{-0.272} & 25 \leq f < 164 \text{ GHz} \\ 0.616f^{0.0126} & f \geq 164 \text{ GHz} \end{cases} \quad (191)$$

with R_r in mm/hr and f in GHz. The calculated rain volume extinction coefficients are provided in Figure 58 along with the coefficients computed with the Mie solution with the Marshall-Palmer drop size distribution superimposed for comparison. Trends among the models are clear, as is the uncertainty in the rain volume extinction coefficient.

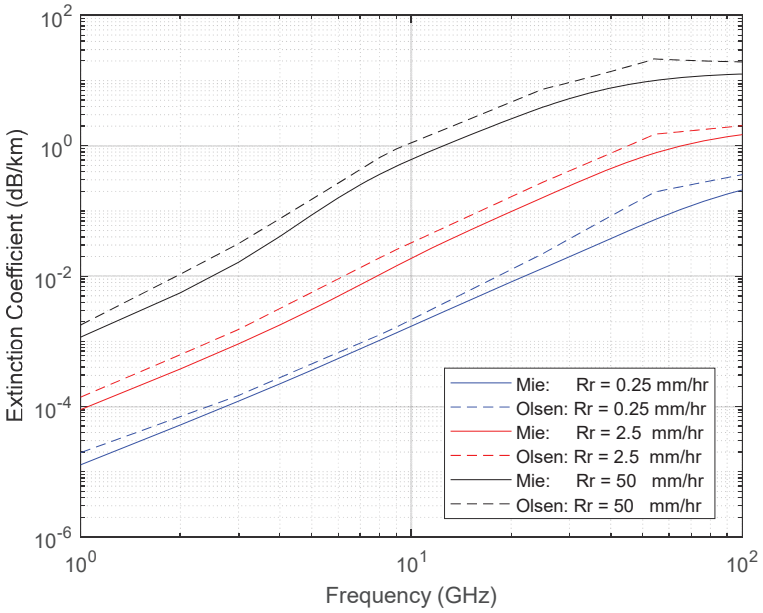

Figure 58. Comparison of Rain Volume Extinction Coefficient Calculated Using Mie Solution and Marshall-Palmer Drop Size Distribution to the Coefficients Calculated with the Olsen Model

3.2.6.4 Propagation Path Length

Rain occurs in two broad categories: (1) stratiform rain, and (2) convective rain. These two separate atmospheric mechanisms have different effects on satellite paths. Stratiform rain is generated in cloud layers containing ice, and results in widespread rain or snow at rainfall rates of less than 10 mm per hour. Convective rain is generated by vertical air currents that can be very powerful, leading to thunderstorms and high rainfall rates. Convective rain is very important for satellite communication systems because it is the major cause of link outages. Stratiform rain consists of a generally constant rainfall rate over a very large area while convective rain is generally confined to a narrow, but tall column of rain [55].

Clouds can be characterized as warm or cold. In warm clouds, the temperature throughout the cloud layer is above freezing ($T = 0$ °C). Rain does form in warm clouds. In cold clouds, the 0 °C isotherm (i.e., melting layer) occurs within (or below) the cloud layer. Thus, the cloud can be a mixed phase cloud, consisting of super-cooled liquid droplets and frozen particles. Cirrus clouds, which are very high in the atmosphere, consist only of ice (i.e., glaciated).

Rain characteristics along the propagation path are dynamic. Precipitation can change phase during descent – evaporating (i.e., virga) or freezing. Also, the size of a precipitation cell can be a much smaller, time varying, fraction of the size of the cloud structure.

Figure 59 (left) illustrates the slant path through a rain event for a cloud with a very large base area and relatively small depth, such as a stratus cloud. In this figure, the melting layer is above the cloud top, which indicates a warm cloud. For an angle of arrival denoted as θ, the propagation path length, R, is calculated as:

$$R = \left(h_{base} - h_{surface}\right)\sec\theta \text{ (m)}. \tag{192}$$

Typically, the rain rate is not constant along R. Rain-rate sensors located at the ground terminal location may not accurately represent the actual rain-rate along the path. Figure 59 (right) illustrates the slant path through a rain event for a taller cloud, such as a cumulonimbus type cloud, which typically have much less base area. The horizontal distance of the rain cell is denoted as L_{cell}. Typically, L_{cell} is less than the horizontal distance of the cloud formation. In this case, the propagation path length is calculated as:

$$R = L_{cell}\csc\theta \text{ (m)}. \tag{193}$$

Figure 59 (right) depicts the worse-case geometry, where R transverses the entire rain cell width. As the rain cell moves over time (i.e., left to right), the bottom of the propagation path clears, but the top of the link passes through the cloud layer. The melting layer is indicated as occurring within the cloud, so this is a mixed phase cloud. Below the melting layer, liquid precipitation can occur on the propagation path. Above the melting layer, a mixture of liquid and frozen precipitation can occur on the propagation path. Signal attenuation due to precipitation will vary greatly as the cloud and rain cell drift across the propagation path.

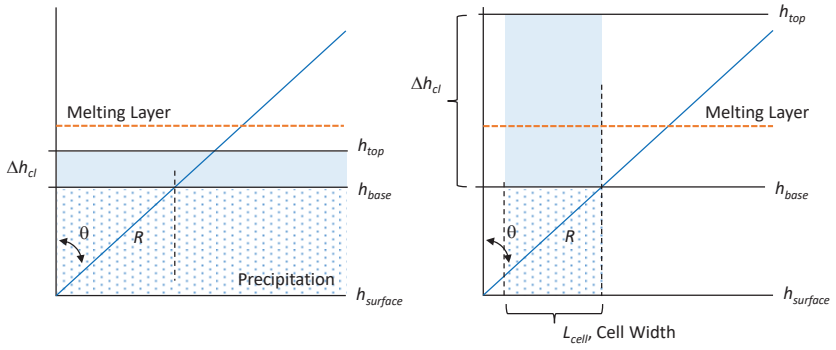

Figure 59. Illustration of Propagation Path Through Rain

3.2.6.5 Optical Thickness

It is informative to calculate the optical thickness for the two scenarios depicted in Figure 59. First, let's assume a precipitating stratus cloud with h_{base} = 600 m and $h_{surface}$ = 0 m, light rain conditions, R_r = 5 mm/hr, θ = 45°, ψ = 45° (i.e., circular polarization), and f = 82.5 GHz. Using the ITU model to calculate the rain volume extinction coefficient gives $\kappa_{e_{rn}} = 3.7$ dB/km. Using Eq. (192) to calculate the propagation path through the rain yields R = 0.85 km. Therefore, the optical thickness for the rain event is about τ = 3.1 dB.

For the second scenario, let's assume a precipitating cumulonimbus cloud with L_{cell} = 1 km, heavy rain conditions, R_r = 50 mm/hr, θ = 45°, ψ = 45°, and f = 82.5 GHz. Using the ITU model to calculate the rain volume extinction coefficient gives $\kappa_{e_{rn}} = 18.7$ dB/km. Using Eq. (193) to calculate the propagation path through the rain yields R = 1.4 km. Therefore, the optical thickness for the rain event is about τ = 26.2 dB.

Given the variability of cloud and precipitation losses and the uncertainty of modeling tools, the effects from clouds and precipitation are typically assessed statistically for a given time period and a given location. The ITU provides a procedure to estimate long-term statistics of slant-path rain attenuation at a given location for frequencies up to 55 GHz [56].

Tarasenko presented modeling and experimental results using the W/V-band Terrestrial Link Experiment (WTLE), which is discussed in a later section [57]. Tarasenko developed an innovative method for distributed sensing of the rain-rate along a propagation path using NEXRAD (Next Generation Weather Radar) weather radar.

3.2.6.6 Depolarization

Rain and frozen precipitation also causes depolarization. Depolarization is the loss of signal energy from the intended (i.e., the co-polarized) channel into the unintended (i.e., the cross-polarized) channel. Under ideal conditions, depolarization will not occur. When depolarization does occur, it can cause co-channel interference and cross-talk between dual-polarized satellite links [58].

Depolarization is more difficult to quantify than attenuation. All signals have a polarization orientation that is defined by the electric field vector of the signal. In general, signals are never purely polarized. The direction of the electric field will never be perfectly oriented or constant. Successful orthogonal polarization frequency sharing – usually called dual polarization frequency re-use – requires that there be sufficient isolation between two orthogonal polarization states to permit the separation of the wanted polarization from the unwanted polarization at the receiving antenna. The difference between the co-polarized and the cross-polarized signal energy will determine the cross-polarization discrimination (XPD) at the receiver, and hence the level of interference between two orthogonally polarized signals [59].

If there are asymmetric rain or ice crystal particles along the propagation path, then depolarization will occur. The measure of depolarization that is most useful for analyzing communications systems is the cross-polarization isolation (XPI), which is the decibel ratio of wanted power to unwanted power in the same channel. The larger the XPI, the less interference there is, and the better the communications channel will perform. XPI is difficult to measure. In most transmission

situations encountered in practice, the values calculated for XPI and XPD are the same and they are simply called the isolation.

In practice, real antennas do not transmit polarization pairs that are exactly orthogonal, nor does the isolation remain the same over the 3 dB beamwidth of the antenna. Receiving antennas can also introduce cross-polarization. There is therefore a residual XPD component present even in clear-sky conditions.

3.2.7 W/V-band Terrestrial Link Experiment – Description and Link Budget

The W/V-band Terrestrial Link Experiment (WTLE) was established in 2015 in Albuquerque, NM, to enable W/V-band propagation studies. It was developed by scientists and engineers from the Air Force Research Laboratory, the University of New Mexico, and NASA Glenn Research Center. WTLE consists of a single tone transmitter located on Sandia Crest and a companion receiver unit located at the UNM COSMIAC[14] facility. Figure 60 presents the geometry of the WTLE test range. The propagation path between the transmitter and receiver is 24.3 km. The propagation path slant angle is 4.16°, which yields a vertical altitude change of about 1763 m.

The WTLE transmitter unit is shown in Figure 61. It provides a circularly polarized tone at 72 GHz. The transmit power is ~5 mW. It uses an 8.9-cm (~3.5-inch) diameter Gaussian lens antenna. The transmitter site includes weather sensors and an optical disdrometer that measures precipitation. Weather sensors measure temperature, pressure, and relative humidity. A visibility sensor is also included to detect the presence of clouds. Data are sampled and stored for analysis.

Early in the program, WTLE also transmitted a W-band tone. However, the W-band receiver was re-purposed for a short-link experiment in 2019.

[14] Configurable Space Microsystems Innovations and Applications Center

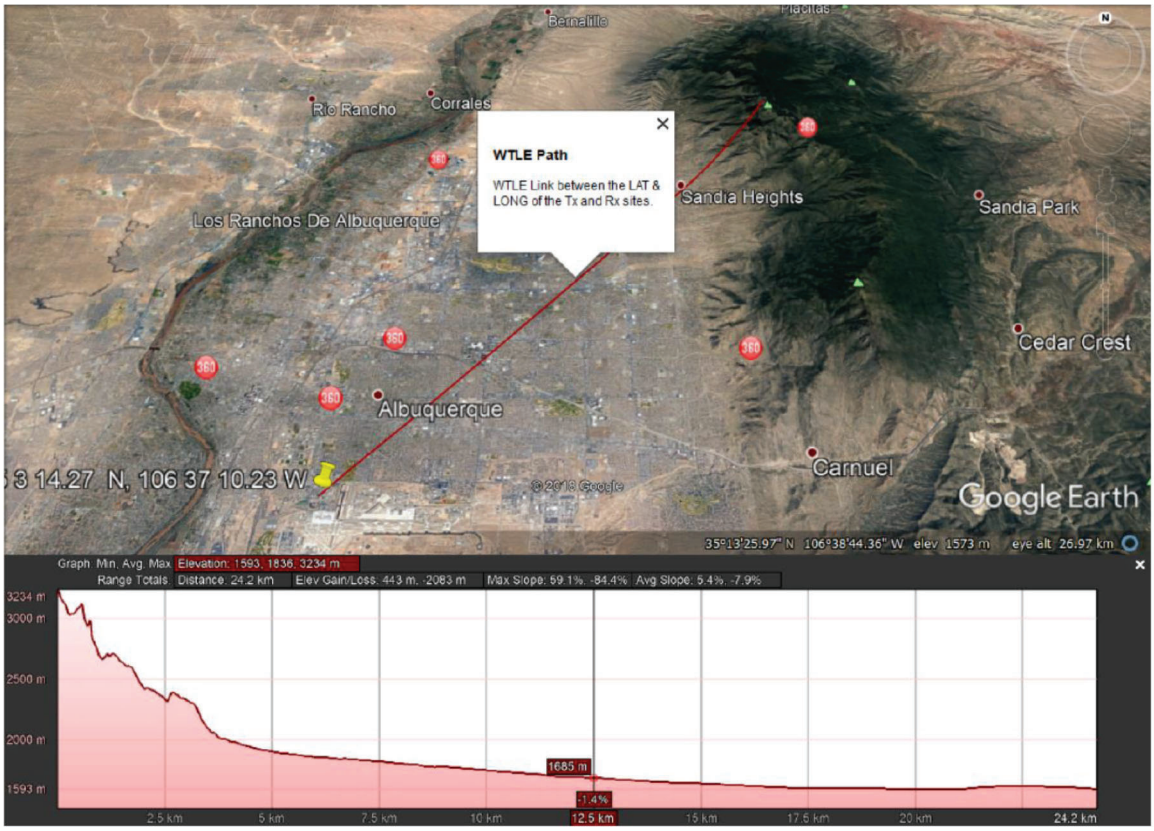

Figure 60. WTLE Geometry and Elevation Profile

Figure 61. WTLE Transmitter, Weather Station, and Disdrometer

Figure 62 shows the receiver site. The receiver uses a 0.61-m (24-inch) diameter Cassegrain reflector antenna. The WTLE receiver is capable of measuring co-polarization and cross-polarization signal power. The receiver uses a two-stage down-conversion process to bring the V-band tone down to an intermediary frequency, f_{IF}, for sampling by the analog-to-digital converter. The receiver site includes weather sensors, an optical disdrometer, and a multi-frequency radiometer. Data are sampled and stored for analysis.

Table 13 provides a simple link budget based on component values measured early in the program. Atmosphere losses are not included, because they are addressed later in the results section.

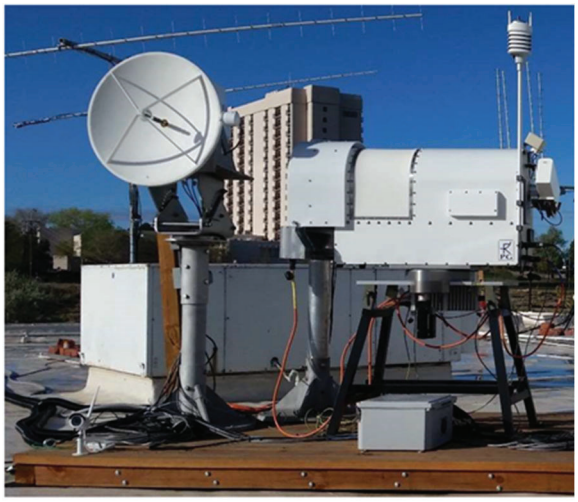

Figure 62. WTLE Receiver Site at COSMIAC

Table 13. WTLE Link Budget

Parameter	Value	
Frequency	72 GHz	
Transmit Power (5 mW)	-23 dB	7 dBm
3.5-inch Antenna Gain	34.7 dBi	
Free Space Propagation Loss (24.3 km)	-157.3 dB	
24-inch Antenna Gain	50.9 dBi	
Low Noise Amplifier Gain	32.53 dB	
2nd Stage Amplifier Gain	9.3 dB	
Received Signal Power	-52.9 dB	-22.9 dBm

3.3 Rectangular Waveguide Antenna Array

In this section, the focus is on designing, fabricating, and testing antennas that are suitable for operating within the W and V frequency bands. In particular, the emphasis was on the design of slotted ***rectangular waveguide antenna arrays*** and ***cross-slotted waveguide fed horn antennas***. These structures are known for their high efficiency and highly circular polarized gain that can be implemented in satellite and terrestrial communication links. In addition, such designs can be implemented in radar applications that operate in frequency bands around 72 GHz or 84 GHz. Such antenna structures are inexpensive to fabricate, since they can simply be machined using high precision conventional methods (like milling) and laser cutting when suitable. A new type of *z*-arm shaped cross slots is introduced that fits on the broad-wall of a conventional rectangular waveguide. The feeding network was also optimized to regulate the power and the phase of each rectangular waveguide element in order to increase the gain of the antenna array.

3.3.1 Design of Z-Shaped Cross-Slot

In this section, the design of a *z*-shaped cross-slot along the broad-wall of a WR-10 rectangular waveguide operating in the TE_{10} mode is investigated. For the fundamental mode, and along the broad-wall of the waveguide, the magnetic field has two components: H_x and H_z, where:

$$H_x = -\frac{A}{Z_{10}} \sin\frac{\pi x}{a} e^{-j\beta z} \tag{194}$$

$$H_z = \frac{j\pi A}{\beta a Z_{10}} \cos\frac{\pi x}{a} e^{-j\beta z}. \tag{195}$$

The two components of the magnetic field are 90° out-of-phase at all times. At a certain range of positions *s*, far from the narrow wall of the waveguide, the magnitudes of the magnetic field components are equal for certain frequencies. These positions are given by:

$$s = \pm\frac{a}{\pi}\tan^{-1}\frac{1}{\sqrt{\left(\frac{2fa}{c}\right)^2 - 1}}. \tag{196}$$

Circularly polarized waves can therefore be radiated by having a slot centered at a position *s*. For each frequency, there are two positions *s* where circular polarization is achieved. Also, by changing the *z*-direction in which the wave is propagating, the radiated wave can be changed from right hand circular polarization (RHCP) to left hand circular polarization (LHCP). This is physically done by changing the feeding in the waveguide from one port to the other port.

In order to radiate the maximum amount of power, a cross-slot is usually adopted. Figure 63 depicts a conventional cross-slot placed at a distance *s* away from one of the waveguide narrow walls. The cross-slot has two arms with length $L_a \approx \lambda/2$ and width $W_a \approx \lambda/10$. At certain frequencies, the slot arm projection on the *x*-axis (A_p) is larger than the position *s*. This causes the slot to overlap with the narrow wall of the rectangular waveguide. Figure 64 shows the difference *X* between A_p and *s* for a span of frequencies from 75 GHz up to 110 GHz for a WR-10 waveguide. From this plot, one can conclude that, for a WR-10 waveguide, the design of a cross-slot is feasible only for

frequencies less than or equal to 84 GHz. Thus, for our frequency range of interest (84-86 GHz), the conventional cross-slot cannot be adopted.

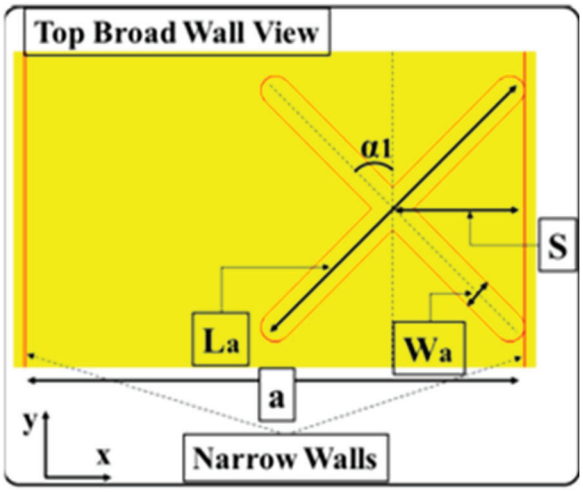

Figure 63. Conventional Cross-slot Dimensions

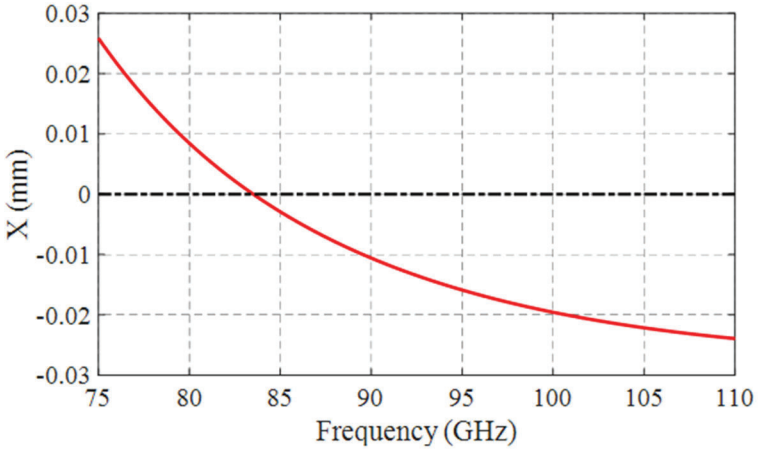

Figure 64. Difference Between the Arm Projection and Slot Position

To solve this problem, the position *s* can be increased to accommodate the arms within the broad wall. By increasing *s*, the isolation between the co- and cross-polarization in the direction of the highest gain is reduced. This is due to the fact that the magnitudes of the components of the magnetic field are not equal at these positions.

Another solution is to use *z*-shaped arms for the cross-slot by bending the tips of the arms as shown in Figure 65. The new arms will fit within the borders of the broad wall for frequencies beyond 84 GHz while maintaining the same positions *s*. By optimizing the dimensions of the *z*-shaped arms,

the slot is able to radiate at the same frequencies as the cross-slot while having a shorter arm projection on the *x*-axis.

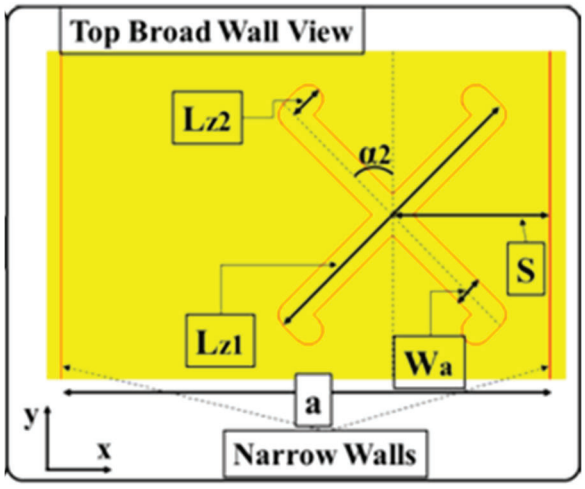

Figure 65. *z*-shaped Arm Cross-slot Structure

To investigate the effect of changing the shape of the slot, a WR-10 rectangular waveguide (a = 2.54 mm × b = 1.27 mm) was first designed with the cross-slot shown in Figure 63. The cross-slot had dimensions L_a = 1.83 mm, W_a = 0.15 mm and was at a distance s = 0.67 mm from the narrow wall. At 84 GHz, the slot radiates 73.5% of the power. Figure 66 shows that the gain was 4 dB with an isolation of 28 dB between LHCP and RHCP at the direction of maximum gain.

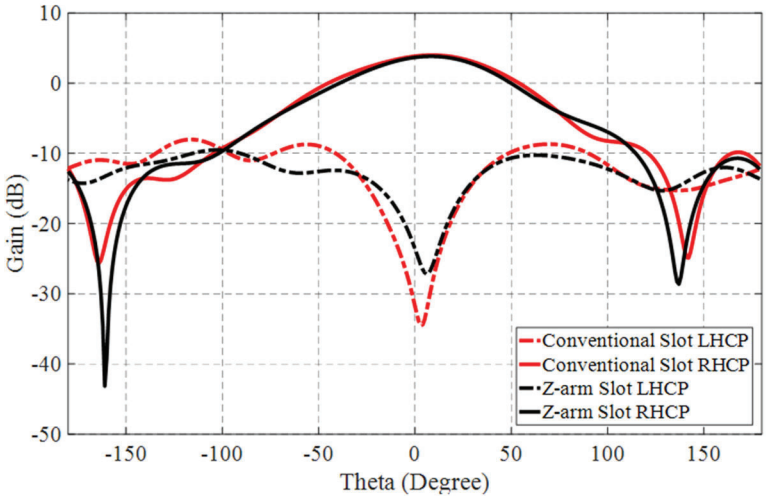

Figure 66. Co- and Cross-polarization Radiation Patterns for the Conventional and *z*-arm Slots in the XZ Plane

The next step was to replace the cross-slot by the one shown in Figure 65. The new corresponding dimensions were L_{z1} = 1.61 mm with the short arm length L_{z2} = 0.38 mm. The slot width was W_a = 0.15 mm and centered at s = 0.82 mm from the narrow wall of the WR-10 waveguide. At 84 GHz, 70.5% of the power is radiated by the slot. The achieved gain was 4 dB with an isolation of 28 dB between the co- and cross-polarized radiations at the direction of maximum gain, as shown in Figure 66.

The comparison between the two designs at 84 GHz shows that the *z*-shaped slot preserved the same polarization isolation as the conventional slot. However, the *z*-shaped arm cross-slot ensures that the full slot topology fits on the broad wall without any overlap with the narrow wall for all frequencies of the W-band.

3.3.2 Design of a Waveguide Array

To improve antenna gain, we consider an array of slots along the WR-10 waveguide broad walls.

3.3.2.1 Single Waveguide with Multiple Slots

The number of *z*-shaped arm cross-slots determine the maximum gain that can be produced from a single WR-10 waveguide element. Thus, it is essential to determine the optimal number of slots that can produce the maximum achievable gain levels. Figure 67 shows the corresponding structure with 4 and 16 slots. For the different scenarios, the *z*-shaped arm cross-slots have the same "long arm" length L_{z1} = 1.67 mm and the same "short arm" length L_{z2} = 0.433 mm. The slot width was chosen to be W_a = 0.15 mm and centered at a distance s = 0.715 mm from the wall of the WR-10 waveguide. The mutual coupling resulting from introducing several slots in close proximity to each other necessitated a change in the dimensions of the slots. At first, the waveguide was designed with 4 slots. The gain exhibited was 8.5 dB at 85 GHz. Doubling the number of slots resulted in a gain increase of 2 – 3 dB across the frequency range 84 – 86 GHz. This can be seen in Figure 67. The gain reached 13.5 – 14 dB with N=16 slots. If the number of slots increases to 32, the increase in gain is only about 0.5 – 1 dB. Thus, it was found that N=16 slots was a good tradeoff between array size and maximum achievable gain. For this number of slots, the length of the waveguide was 39.3 mm.

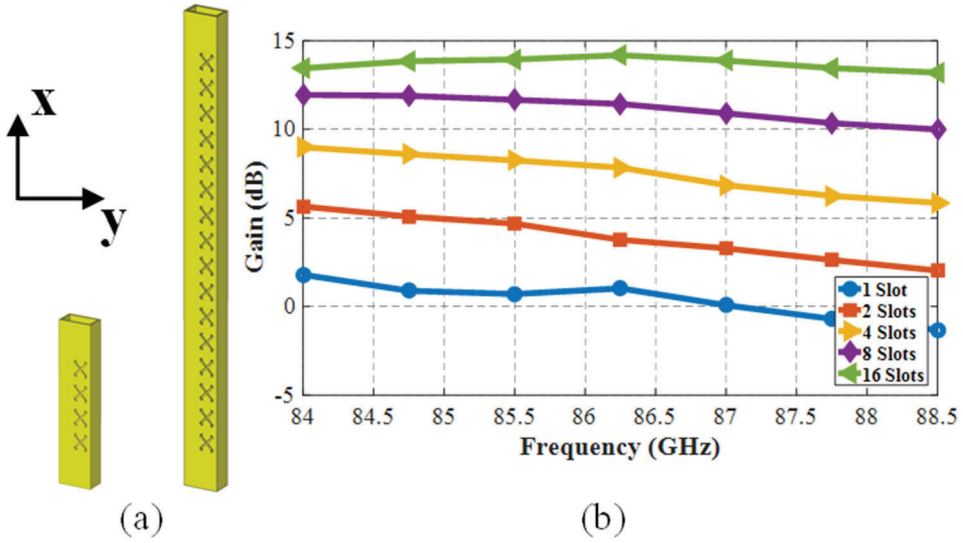

Figure 67. (a) A Single WR-10 Waveguide Element with 4 and 16 Slots; (b) The Gain Variation as a Function of the Number of Slots

The feeding phase difference between the various slots can cause high sidelobe levels if not designed appropriately. Thus, by optimizing the separation distance between slots, the sidelobe level can be minimized. A separation distance of D_x = 2.05 mm ≈ λ/2 was determined to be the optimal choice through an iterative analysis. The phase difference causes the main beam to switch from θ = 0° (one slot) to θ = 40°. Figure 68(a) shows the antenna gain pattern for N=16 slots at f = 85.5 GHz. It is noted that the half power beam-width (HPBW) in the elevation plane (XZ plane) was 8.7° with an isolation of more than 18 dB between the co- and cross-polarized gain patterns. A drop in the HPBW was achieved as compared to a single slot due to the increase in the gain levels. The HPBW and isolation values varied slightly over the entire bandwidth.

The increase in the number of slots in one direction (x-direction) while preserving the same number in the other direction (y-direction) makes the main beam narrower in one plane and wider in the other. For example, the HPBW in the azimuthal plane (θ = 40°) increases to 55° as shown in Figure 68(b). One possible solution to maintain almost the same HPBW along both planes is to transform the proposed structure into a two dimensional array as described next.

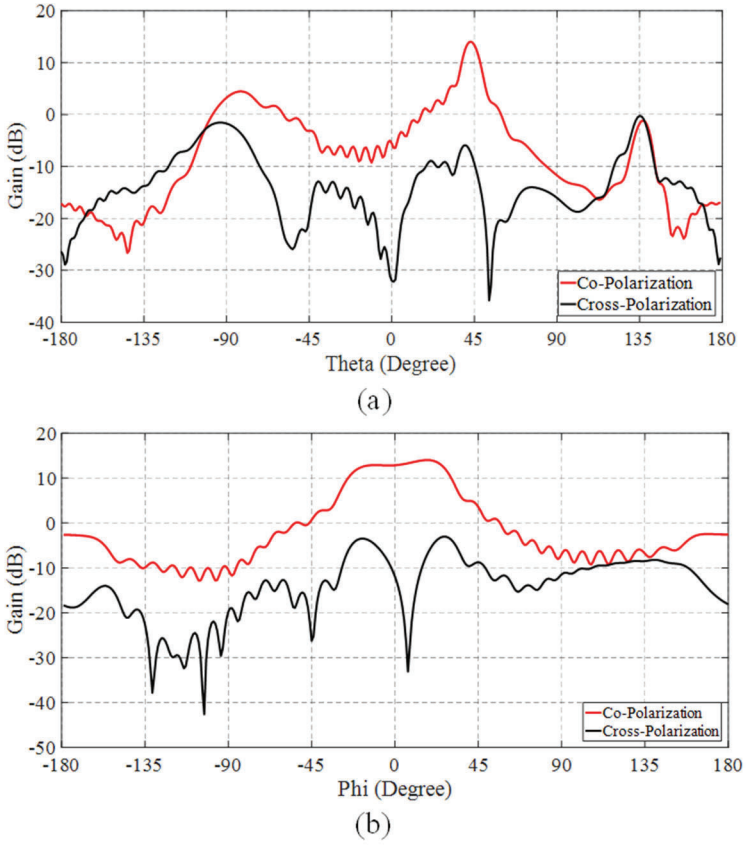

Figure 68. The Co- and Cross-polarized Radiation Patterns at 85.5 GHz with *N*=16 Slots in the (a) Elevation (XZ) Plane, and (b) Azimuthal (θ=40°) Plane

3.3.2.2 2-D Waveguide Array with 16 Slots

A 2-D array was designed by increasing the number of WR-10 waveguides having 16 slots. The new structure with 8 waveguide elements is shown in Figure 69(a). The same slots used in a single waveguide array were used for the 2-D array. The waveguides of the 2-D array were placed next to each other. All of the waveguides had the cross-slots on the same side of the wall. The separation between the slots of the same waveguide was kept the same as in the case of a single waveguide D_x = 2.05 mm. The separation between the slots of the same row in adjacent waveguides was taken to be D_x = 3.04 mm. This separation was limited by the WR-10 waveguide width (a = 2.54 mm) as well as the thickness (t_{w1} = 0.5 mm) of the walls between any two adjacent waveguides.

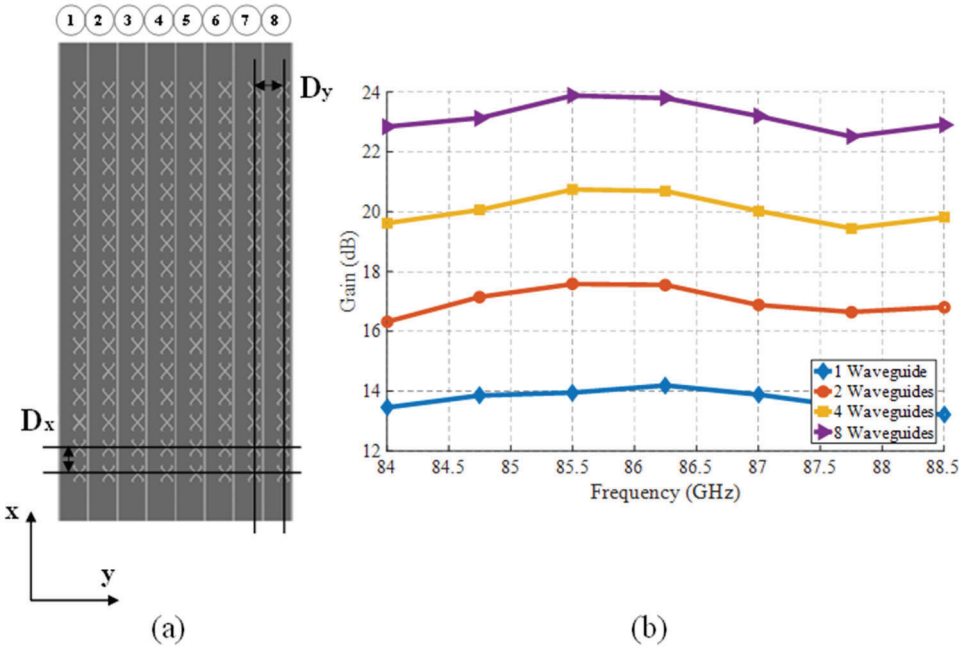

Figure 69. (a) Proposed 8x16 Cross-slotted Rectangular Waveguide Array, and (b) Gain Variation with the Number of Waveguides

The change in the array gain with the increase in the number of the waveguide elements is plotted in Figure 69(b). The gain of the array improved by 2.5 – 3.5 dB as the number of waveguides was doubled. An increase from around 14 dB to around 24 dB was obtained for the case of eight waveguides. These results were obtained by forcing all the waveguides in the simulation environment to be fed in-phase and with the same amount of power.

Feeding the various waveguides in-phase across the entire frequency band of operation (84-86 GHz) was a challenging task. The phase effect on the performance of the array is analyzed with 8 waveguides. If the consecutive waveguides are fed with a constant phase difference $\Delta\phi_{in} \neq 0°$ and with the same amount of power, then the main beam of the array becomes directed in a plane $\phi \neq 0°$. The following four scenarios are investigated.

3.3.2.2.1 Case 1

If the phase difference is $0° < \Delta\phi_{in} < 20°$ between the waveguide elements, then the main beam is entirely circularly polarized and exhibits a gain of 24 dB with an isolation between the co- and cross-polarized components of more than 22 dB. The main beam direction is in a plane $0° < \phi < 5°$ as shown in Figure 70.

3.3.2.2.2 Case 2

If the phase difference is $20° < \Delta\phi_{in} < 45°$, then the array produces a main beam with a gain of 23.5 dB and the isolation between the co- and cross-polarized components is 15 – 20 dB. This phase causes circular polarization to be lost across some parts of the HPBW as shown in Figure 70.

3.3.2.2.3 Case 3

If the phase difference is $\Delta\phi_{in} \geq 45°$, then the array does not produce circularly polarized radiation at the main beam. The direction of the main beam is in a plane $\phi > 14°$ as shown in Figure 70. In the case of a single slot, the main beam is circularly polarized along the *z*-axis. The further away from the *z*-axis, the less the radiated E-fields are circularly polarized. The phase difference discussed in this case causes the electric fields far from the *z*-axis to add up. It causes the circularly polarized fields close to the *z*-axis to cancel each other. This effect causes the main beam to be elliptically polarized and directed in a plane $\phi > 14°$.

3.3.2.2.4 Case 4

In order to direct the main beam in the plane $\phi = 0°$, the phase differences between the consecutive waveguides should be $0° < \Delta\phi_{in} < 20°$. The various waveguides must also be fed with the same amount of power. In addition, if the pairs of waveguides (1, 8), (2, 7), (3, 6) and (4, 5), shown in Figure 69(a), have the same phase at their input, then the main beam is directed in the desired plane.

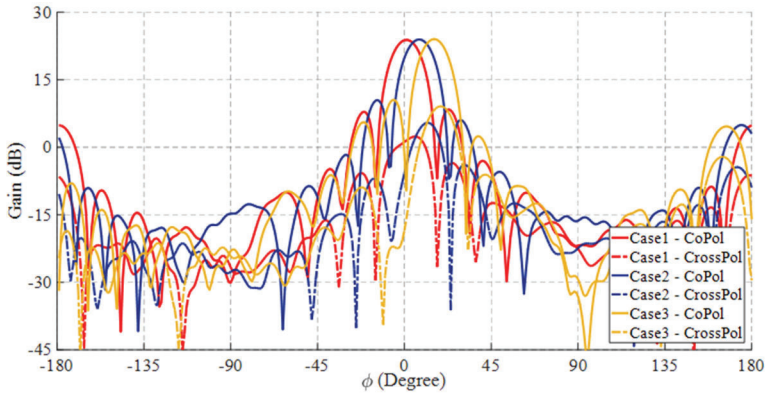

Figure 70. The Radiation Pattern of the Array in the Azimuthal (θ=40°) Plane for Scenarios 1, 2 and 3

Figure 71 compares the gain of the array when the various elements are fed in-phase to the case when the phase difference between the elements is 20º. It was found that the same gain response was obtained. The isolation between the co- and cross-polarized gain patterns was preserved and

the gain was higher than 22 dB in the direction of the highest gain and over the frequency band of operation. More specifically, the array had the main beam directed in the plane $\phi = 0°$ and at an angle $\theta = 40°$. The array's HPBW was $\Theta_{ep} = 8°$ in the elevation plane ($\phi = 0°$), and $\Theta_{ep} = 12.5°$ in the azimuthal plane ($\theta = 40°$). The maximum gain achieved was 24 dB over the frequency span of 84-86 GHz.

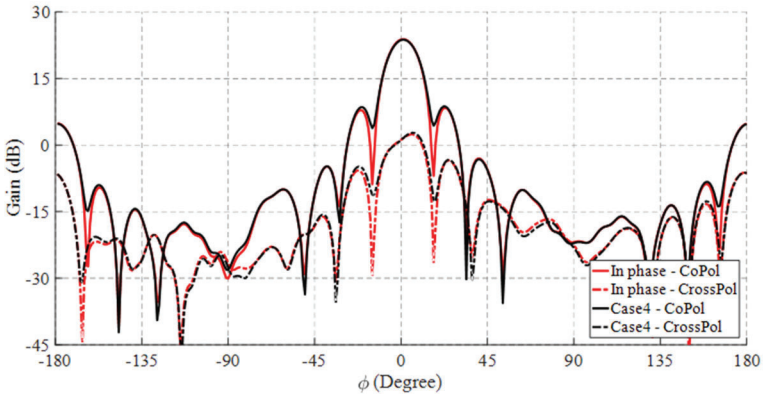

Figure 71. Gain Patterns of the Array in the Azimuthal ($\theta = 40°$) Plane for the Case Where All Waveguides Are Fed In Phase and For Case 4

3.3.3 Feeding Network Design

In the previous section, it was found that the optimum way to feed the different waveguide elements was by either having them all fed in-phase, or by allowing the symmetrical pairs of waveguides to be fed in-phase and the consecutive waveguides to have a small phase difference ($0° < \Delta\phi_{in} < 20°$). To achieve this, a separate feeding network was needed.

The first feed network investigated is depicted in Figure 72. It was composed of one feeding waveguide that connected directly to the eight WR-10 waveguide elements. The connection was achieved by introducing rectangular slots on the narrow wall of the feeding waveguide and shorting its other end. These slots were centered at the centerline of the narrow wall and radiated the same power into the eight waveguide elements of the array. The distance of separation between the slots was very crucial to the array performance, since such distance sets the phase difference between the various eight waveguide elements.

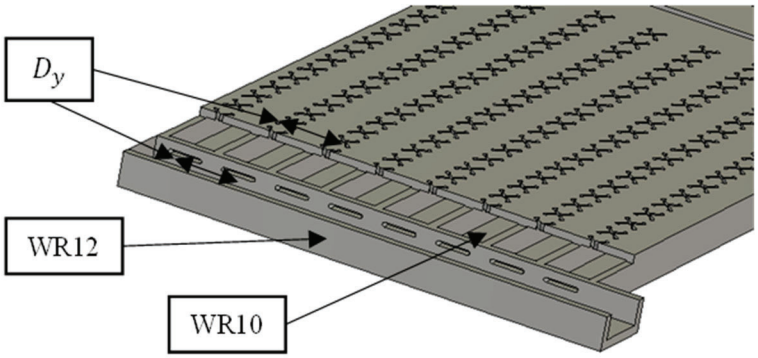

Figure 72. Proposed Feeding with Direct Connection Between the Feeding Waveguide and the Eight Elements WR-10 Waveguides

The eight waveguide elements had a center-to-center separation of D_y = 3.04 mm. If a WR-10 rectangular waveguide is used directly as the feeding waveguide, then the separation between the rectangular slots (3.04 mm) results in a $\Delta\phi_{in}$ = 223° phase difference between the consecutive waveguide elements at 85 GHz. This phase difference causes the main beam to be in the plane ϕ = 32°. The gain of the array was reduced to 22 dB and the circular polarization was lost as shown in Figure 73. The same behavior is obtained if the feeding waveguide is a WR-12 rectangular waveguide and the distance of separation between the rectangular slots is kept to be 3.04 mm. In this case, the phase difference is $\Delta\phi_{in}$ = 254.5° at 85 GHz. The main beam is directed in the plane ϕ = 37° and the array is no longer circularly polarized. The gain patterns for this case are also incorporated in Figure 73. Based on these results, it is concluded that a transition must exist between the eight rectangular slots and the opening of the eight WR-10 waveguides.

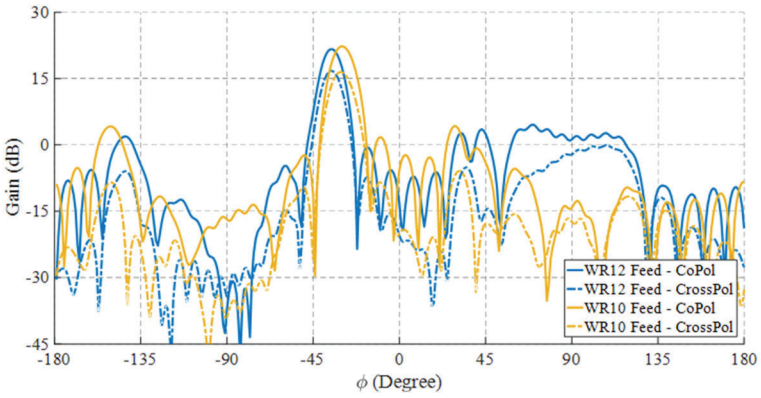

Figure 73. The Gain Pattern of the Array Fed Directly by a WR-10 or WR-12 Rectangular Waveguide in the Azimuthal (θ = 40°) Plane

The modified layout of the proposed feeding network is depicted in Figure 74. For this case, a WR-12 feeding waveguide with wall thickness t_{w2} = 0.5 mm was adopted, since during

measurements, the feeding source had a WR-12 rectangular waveguide output. In order to achieve a phase difference of $\Delta\phi_{in} = 0° + 360°$ between the consecutive waveguide elements at 85 GHz, the separation between the rectangular slots of the feeding waveguide was increased from D_y = 3.04 mm to D_{yf} = 4.22 mm. The feeding waveguide was shorted at its other end with a separation of S_{short} = 1.71 mm between the last slot center and the shorting plate. The rectangular slots have a length L_{sf} = 1.91 mm and a width W_{sf} = 0.25 mm. These slot dimensions ensure that the feeding network has a good input match between 84-86 GHz as shown in Figure 75. The insertion loss, $|S_{i1}|$, between the input of the feeding waveguide and each of the rectangular slots is also shown in Figure 75. These results show that each waveguide element of the array was able to receive approximately an equal amount of power from the rectangular slots at the frequency bands of operation. The phase difference between the input of the feeding network and the eight rectangular slots is plotted in Figure 75. A phase difference in the range $0° < \Delta\phi_{in} < 20°$ was maintained.

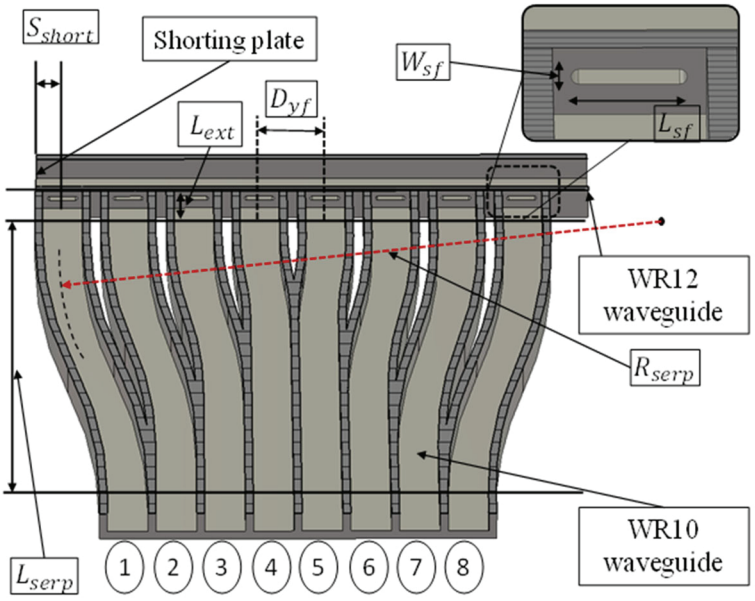

Figure 74. The Proposed Transition to Achieve the Required Phase Difference Between the Various Elements

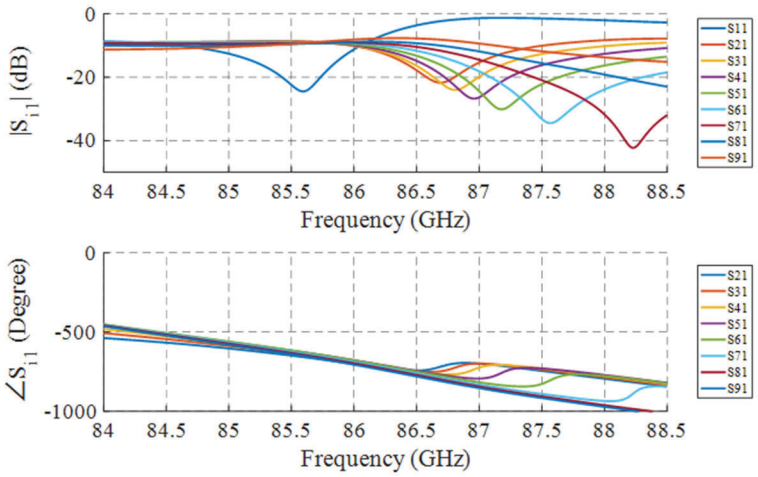

Figure 75. The Feeding Network S-parameters Magnitude in dB and Phase in Degrees

Since the separation distances between the feeding rectangular slots D_{yf} and the radiating cross-slots D_y were different, serpentine WR-10 rectangular waveguides were used as shown in Figure 74. The serpentine waveguides were symmetrical for the pairs of waveguides (1, 8), (2, 7), (3, 6) and (4, 5). This design ensured that the same phase at the output of each pair of waveguides and a small phase difference between the consecutive waveguides. These waveguides were connected to the feeding slots by WR-10 waveguide sections of length L_{ext} = 5 mm in order to minimize the wave reflection caused by the curvature of the serpentine shape. The serpentine waveguides had a curvature radius R_{serp} = 50 mm and a total length L_{serp} = 58.15 mm.

3.3.4 Full Array Design

Two feeding networks, as the one detailed in the previous section, were used to feed the two sides of the eight-element WR-10 waveguide array. The various parts of the full array design are detailed in Figure 76. Two WR-12 waveguides (parts 1 and 1a) constitute the input and the output ports of the whole array structure. A metallic sheet (parts 2 and 2a) with eight rectangular slots connected each of the WR-12 waveguide to the input of the serpentine-shaped connections of the feeding network. Part 3 was composed of the eight rectangular WR-10 waveguides along with the serpentine-shaped connections. A metallic sheet with the 8×16 *z*-shaped arm cross-slots constituted part 4. The last part (part 5) was used as a metallic enclosure around the *z*-shaped arm cross-slots in order to ensure a bound connection between the various parts of the array and to hold the array together. The metallic sheet (part 4) had a thickness t_{w3} = 0.4 mm. It is noticed that for t_{w3} = 0.5 mm, the best isolation between the co- and cross-polarized gain patterns was attained. However, t_{w3} = 0.4 mm was the limit imposed by the fabrication process that was implemented for this particular array. The antenna assembly technique is also highlighted in Figure 76 and the physical layout of the assembled array is shown in Figure 76.

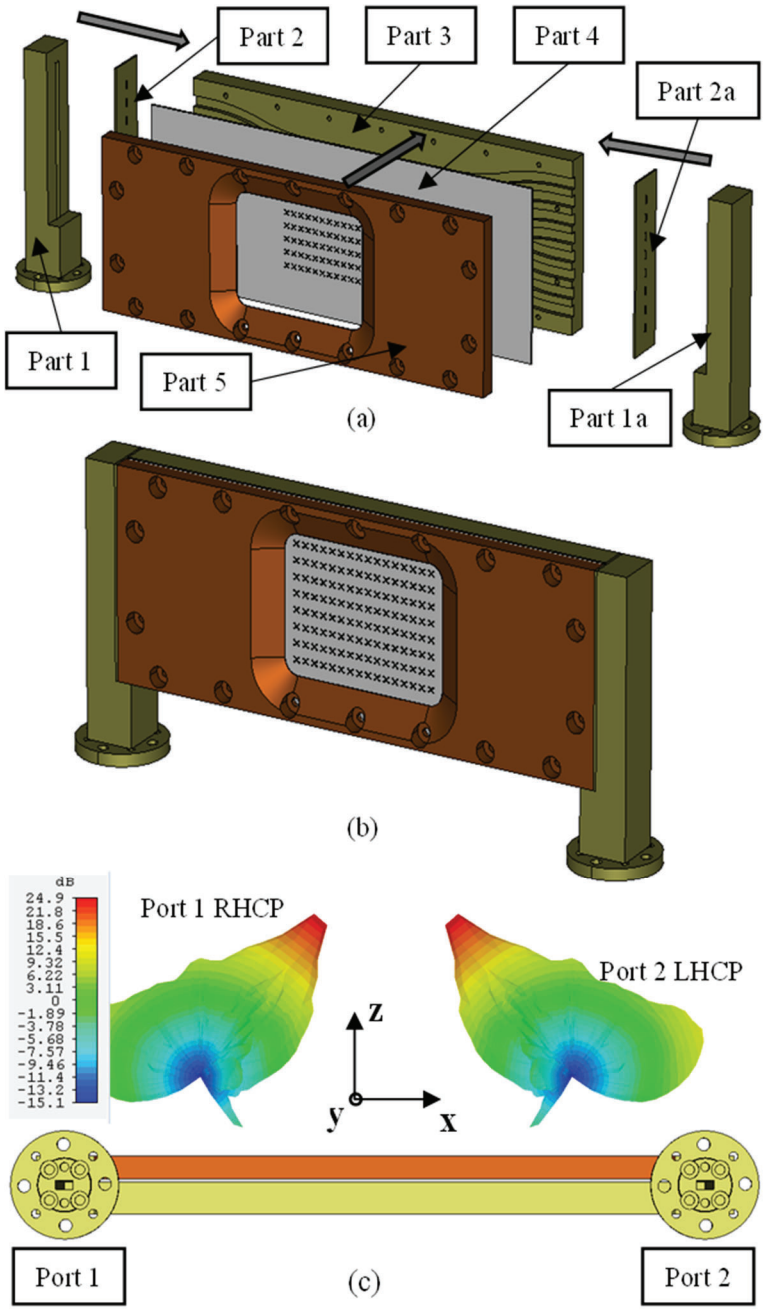

Figure 76. The Full Array Design (a) Disassembled, (b) Assembled, and (c) Radiation Pattern for Each Port

The final design dimensions were optimized using the CST Studio Suite[15] built-in optimization tool in order to deliver a gain of 23 – 24 dB over the frequency band of operation (84 – 86 GHz). The main beam in the elevation plane was directed in $\theta = 40°$ when fed through port 1, and θ

[15] CST Studio Suite is a computational electromagnetics tool developed by Dassault Systèmes Simulia.

= -40° when fed through port 2 as shown in Figure 76. The final design parameters are shown in Table 14. It is essential to note that the feeding network and the metallic enclosure have no effect on the radiation pattern of the array.

Table 14. Dimensions of the Different Parameters of the Array

z-shaped Arm Cross-slot Parameters		
Parameter	**Description**	**Value**
L_{z1}	long arm length	1.65 mm
L_{z2}	short arm length	0.433 mm
W_a	arm width	0.15 mm
S	slot center position	0.7 mm
α_2	arm angle with y-axis	43°
D_x	slots separation along x-axis	2.05 mm
D_y	slots separation along y-axis	3.05 mm
t_{w3}	slot thickness	0.4 mm
Feeding Network Parameters		
Parameter	**Description**	**Value**
L_{sf}	feeding slot length	1.914 mm
W_{sf}	feeding slot width	0.25 mm
D_{yf}	feeding slots separation	4.22 mm
S_{short}	last slot center separation with shorting plate	1.71 mm
R_{serp}	serpentine waveguide curvature radius	50 mm
L_{serp}	serpentine waveguides length	58.15 mm
t_{w2}	feeding slot thickness	0.5 mm

3.4 Cross-Slotted Waveguide-Fed Horn Antenna

In this section, the theoretical analysis of a cross-slotted waveguide polarizer is presented and discussed. The polarizer achieves a right-hand or left-hand circular polarization by altering the feeding ports. The polarizer feeds different conical horns or pyramidal horns without affecting their characteristics. The efficiency of the polarizer is improved by combining the power of different crossed slots using square waveguide combiners. Other modes of operation of the cross-

slot polarizer have also been investigated for multiband operation. An antenna system operating at 72 GHz and 84 GHz (simultaneously) was designed.

3.4.1 Single Slot Feeding a Conical Horn Antenna

3.4.1.1 Horn Antenna Design

The antenna used to test the polarizer was symmetrical in nature, which allowed it to support a circularly polarized wave. A polarizer was used to excite two TE_{11} (transverse electric) modes[16] with orthogonal electric fields at the feeding waveguide input with a phase difference of 90°.

The design of conical horns followed guidelines set by A. P. King [60]. These guidelines determine an optimum horn line that leads to the best gains of the horn. This line identifies the best gain that can be achieved as a function of different horn aperture diameters for different horn lengths, L. The horn parameters L and d_m, along with the optimum gain achieved, are illustrated in Figure 77. A numerical equation relating the optimum directivity of the horn to its geometrical dimensions was also derived, and a relationship between directivity, D_c, horn length, L, and aperture diameter, d_m, was established, leading to the following equations:

$$(\mathrm{D_c})_{\mathrm{opt}} \approx 15.9749\left(\frac{\mathrm{L}}{\lambda}\right) + 1.7209 \tag{197}$$

and

$$\mathrm{L} \approx 0.3232\left(\frac{\mathrm{d_m}}{\lambda}\right)^2 - 0.0475\left(\frac{\mathrm{d_m}}{\lambda}\right) + 0.0052. \tag{198}$$

Since the intended applications are for satellite communications, point-to-point terrestrial links, and radar systems, and since the free-space path loss at these frequencies is very high, a minimum gain of 20 dB is required for the horn. As shown in Figure 77, for a conical horn to have a gain (G_h) more than 20 dB, the length of the horn (L) should be around 10λ (i.e., 10 wavelengths). This makes the gain curve for the different diameters well above 20 dB. The aperture diameter (d_m) should be between 5λ and 6λ. These dimensions, at 72 GHz, translate to L = 41.67 mm and d_m = 25 mm.

[16] TE_{11} means that during propagation through waveguide, the electric field and magnetic field are perpendicular to the direction of propagation. The electric field is λ/2 across the broad dimension, and the magnetic field is also λ/2 across the narrow dimension.

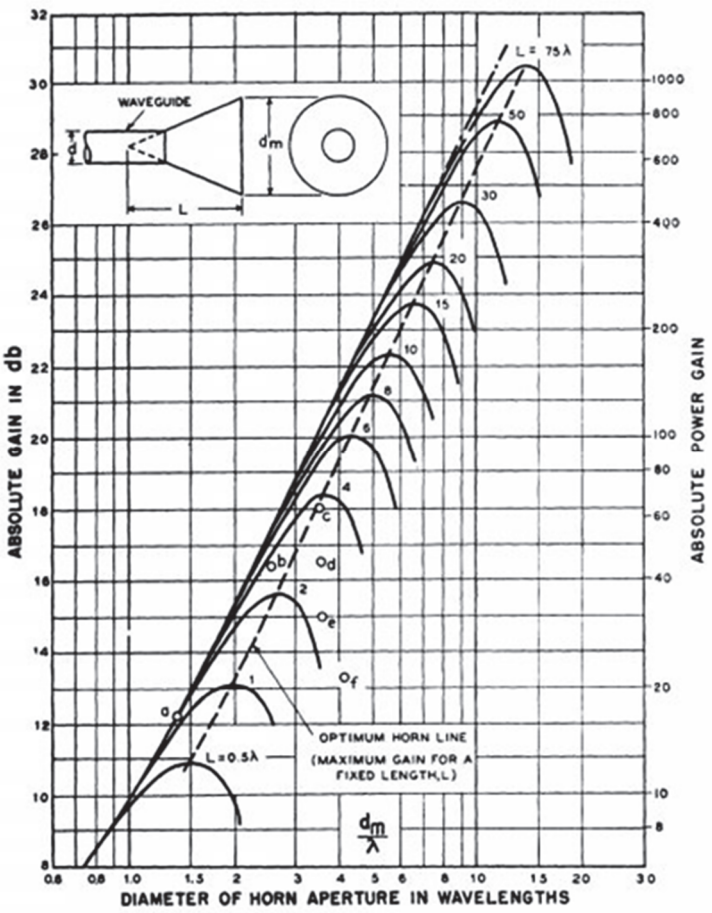

Figure 77. The Absolute Gain of a Conical Horn as a Function of Aperture Diameter (d_m/λ) for a Series of Axial Lengths, *L*

An "off the shelf" conical horn with dimensions close to the ones derived earlier was used to test the polarizer. The horn had dimensions $L = 42$ mm and $d_m = 25$ mm. The circular waveguide feed of the horn had a diameter $d = 3.175$ mm in order for the horn to be operational over the desired frequency range. Due to the dimensions of the circular waveguide, the cutoff frequency for TE_{11} inside the waveguide was:

$$f_{c,TE_{11}} = \frac{1.841 \times c}{d\pi} = 55.37 \text{ GHz.} \tag{199}$$

At the same time, the cutoff frequency of (transverse magnetic wave) TM_{01} is:

$$f_{c,TM_{01}} = \frac{2.405 \times c}{d\pi} = 72.33 \text{ GHz.} \tag{200}$$

This cutoff frequency is very close to the frequency of operation of the system being designed. When the design is fabricated, the fabrication errors might cause the TM_{01} mode to be excited. If the antenna is directly connected to the cross-slot, then the excited TM_{01} causes the output wave to lose its circular polarization and causes the entire design to have low efficiency. In order to avoid that, a circular waveguide with narrower diameter is used to feed the horn. The design details are

explained in the next section. The horn's input is well-matched from 60 – 90 GHz, if fed without adding the extra waveguide as shown in Figure 78.

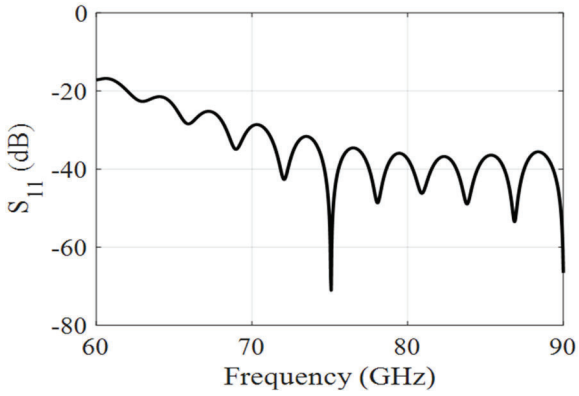

Figure 78. Conical Horn Reflection Coefficient (S_{11})

3.4.1.2 Full System Design

The conical horn was fed using the cross polarizer as shown in Figure 79. In order to suppress higher order modes and only propagate the fundamental TE_{11} mode inside the circular waveguide feed of the horn, another circular waveguide with a narrower diameter was added between the cross-slot and the horn system. This new waveguide played a dual role of making the extraction of power from the rectangular waveguide more efficient and limiting the modes being fed to the conical horn.

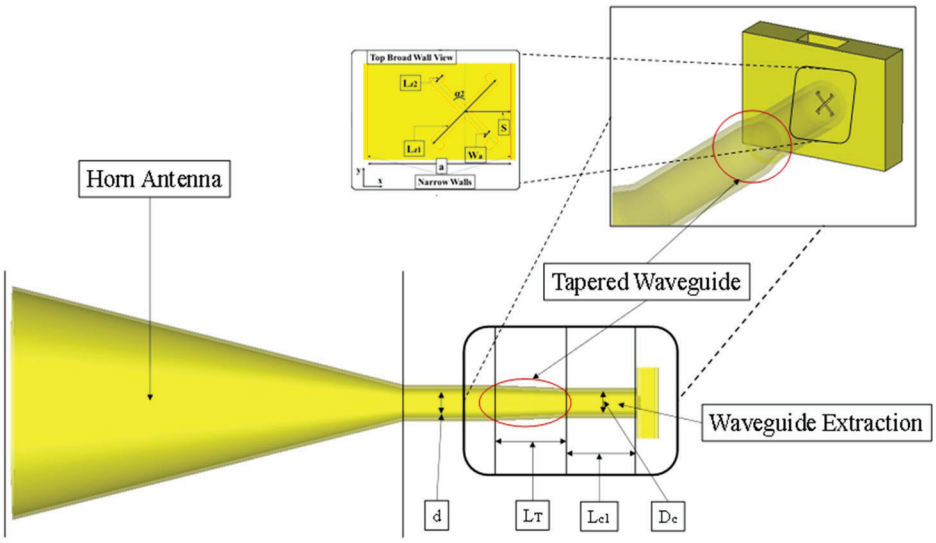

Figure 79. Single Slot Feeding a Conical Horn Antenna

To have good matching in the system and good efficiency, a transition between the two circular waveguides was added. The transition was made of a tapered circular waveguide. Two different designs, one at 72 GHz and one at 84 GHz were developed. The 72 GHz design had a cross-slot on the broad wall of a WR-12 waveguide (a = 3.1 mm and b = 1.55 mm), while the 84 GHz design had the cross-slot on the broad wall of a WR-10 waveguide (a = 2.54 mm and b = 1.27 mm). The different design dimensions for both frequencies are indicated in Table 15.

Table 15. Design Dimensions for the Polarizer at 72 GHz and 84 GHz

Parameter	Description	Value at 72 GHz	Value at 84 GHz
L_{z1}	long arm length	1.85 mm	1.65 mm
L_{z2}	short arm length	0.46 mm	0.36 mm
W_a	arm width	0.15 mm	0.15 mm
S	slot center position	0.69 mm	0.69 mm
α_2	arm angle with y-axis	43.5°	43.5°
t_{w3}	slot thickness	0.4 mm	0.4 mm
D_c	circular waveguide diameter	2.5 mm	2.2 mm
L_{c1}	circular waveguide length	8 mm	8 mm
L_T	tapered waveguide length	2 mm	8 mm
d	diameter of the horn input waveguide	3.175 mm	3.175 mm

3.4.1.3 72 GHz Model

The system designed at 72 GHz had an input reflection coefficient of S_{11} < -15 dB over the frequency range 70 – 86 GHz for both feeding ports. The isolation, S_{21}, between ports 1 and 2 reached -20 dB at 71.8 GHz, which is the main resonance frequency of the slot. Another resonance for the slot caused by the different design components was at ~73 GHz, where the isolation was $|S_{21}| = 9.5$ dB as shown in Figure 80. The two resonances in the design resulted in wider bandwidth over which the efficiency of the design exceeded 70%.

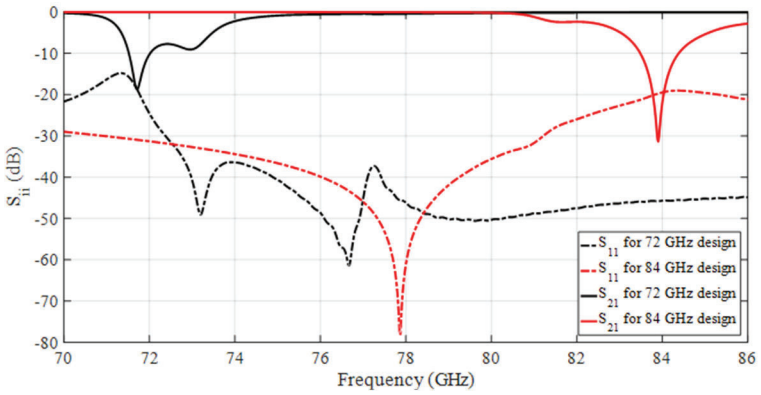

Figure 80. Reflection Coefficient and the Isolation Between Both Ports for Both 72 and 84 GHz Models

The system produced a LHCP gain if fed through port 1, and a RHCP gain if fed through port 2. The system had a total circularly polarized (CP) gain between 21.25 dB – 21.8 dB over the frequency range 71.6 GHz – 73.2 GHz for both LHCP and RHCP. In this frequency range, the total efficiency of the system $70\% < \varepsilon_h < 80\%$. Efficiency ε_h reached its peak of 80% at 71.8 GHz and 73 GHz, which were the two resonant frequencies of the slot. The system gain was 21.8 dB at these frequencies, as shown in Figure 81. The axial ratio (AR_{72}) of the system in the direction of the maximum gain, $\theta = 0°$, was $AR_{72} < 2$ dB over the frequency range 71.6 – 74 GHz, and it reached a minimum of $AR_{72} = 0.125$ dB at 73 GHz, as shown in Figure 82. These results show that the system had a good efficiency, gain, and axial ratio over the frequency range 71.6–73.2 GHz – giving it a 1.6 GHz bandwidth of operation as a polarizer that can produced both LHCP and RHCP.

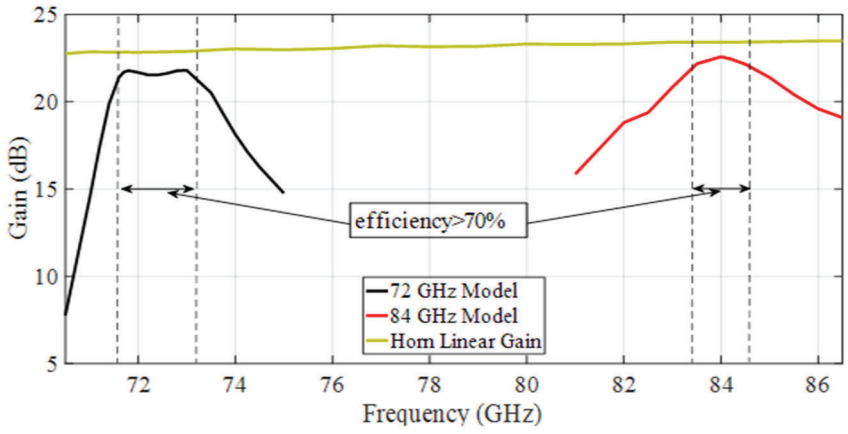

Figure 81. The Maximum Gain of the 72 and 84 GHz Designs versus Frequency Compared to the Linear Gain of the Horn

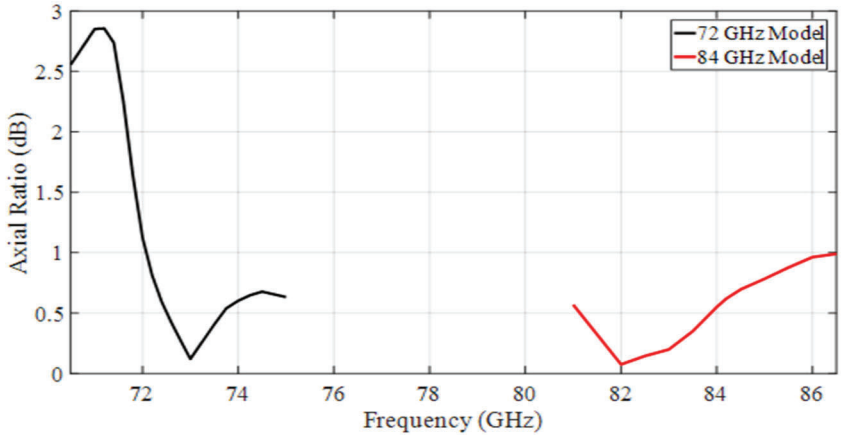

Figure 82. The Axial Ratio of the 72 GHz and 84 GHz Designs versus Frequency

The system produced a half power beam-width (HPBW) of 11.5° in both planes, $\phi = 0°$ and $\phi = 90°$. The entire HPBW of the system was circularly polarized with an AR < 3 dB for the frequency range 71.8 – 73.2 GHz. At 73 GHz, the system produced an AR < 2 dB for the entire HPBW. The cross-polarization discrimination was higher than 18 dB for the entire HPBW, as can be seen in Figure 83 for both planes, $\phi = 0°$ and $\phi = 90°$. Note that the polarizer did not affect the HPBW of the horn. In addition, in the plane $\phi = 90°$, the system reduced the reflection coefficient (S_{11}) of the horn from -19 dB to -23.9 dB.

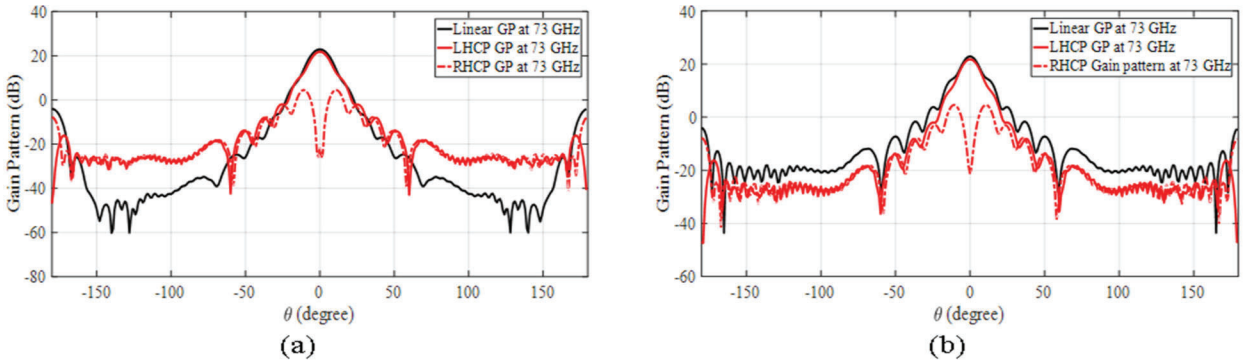

Figure 83. Gain Pattern at 73 GHz, (a) in $\phi = 0°$, (b) in $\phi = 90°$

3.4.1.4 84 GHz Model

The system design for 84 GHz had an input reflection coefficient S_{11} < -19 dB for all frequencies between 70 GHz – 86 GHz for both feeding ports. The isolation was $|S_{21}| > 20$ dB for a bandwidth of 250 MHz over the frequency range of 83.78 – 84.03 GHz. The maximum isolation between ports 1 and 2 reached $|S_{21}| = 33$ dB at 83.906 GHz, where the resonant frequency of the slot is shown in Figure 80. By having one resonance for the slot, the system had a narrower bandwidth

where the efficiency, ε_h > 70%, but the isolation between the ports was improved for a wider frequency range.

The system efficiency, ε_h, in this case was higher than 70% for the frequency band 83.4 – 84.65 GHz as shown in Figure 81. The maximum efficiency of the system was ε_h = 83% at 84 GHz with a circular polarization gain of 22.57 dB. The axial ratio (AR_{84}) of the system in the direction of the maximum gain, $\theta = 0°$, was $AR_{84} < 1$ dB over the frequency range 83 – 85 GHz. It reached a minimum of AR_{84} = 0.2 dB at 83 GHz as shown in Figure 82. These results show that the system had good efficiency, gain, and axial ratio over the frequency range of 83.4 – 84.65 GHz, giving it a 1.25 GHz bandwidth of operation as a polarizer that can produce both LHCP and RHCP. In this case, the bandwidth of operation was less than in the case of the 72 GHz polarizer, due to the system having only one resonant frequency.

3.4.2 Dual Slot Polarizer Using Serpentine Power Combiner

In order to combine the power extracted by the two cross slots, a serpentine power combiner was used. The serpentine power combiner had two circular waveguide inputs and one circular waveguide output. Each section of the input waveguides had a convex curvature followed by a concave curvature, or vice versa, as shown in Figure 84. These curvatures were arcs of a circle smoothly connected. These two sections intersected at the output of the waveguide. The radius of all waveguides used in the serpentine design was optimized to be R_{ws} = 1.25 mm with a cutoff frequency, f_c = 70.33 GHz, for the fundamental mode TE_{11} and a cutoff frequency for TM_{01}, f_c = 91.9 GHz, ensuring that only the fundamental mode was traveling inside the waveguide at 84 GHz.

The curvatures of the serpentine waveguides had a radius R_{serp} = 45 mm as shown in Figure 84. The curvature radius ensured that at the intersection plane of the two sections of the serpentine, the geometry was smooth with respect to the operating wavelength. Smoothness ensured that the wave was not scattered when it hit the intersection plane and that the phase of each TE_{11} mode was preserved. This ensured that the 90° phase difference was intact and that the orthogonal components of the electric field had close magnitudes.

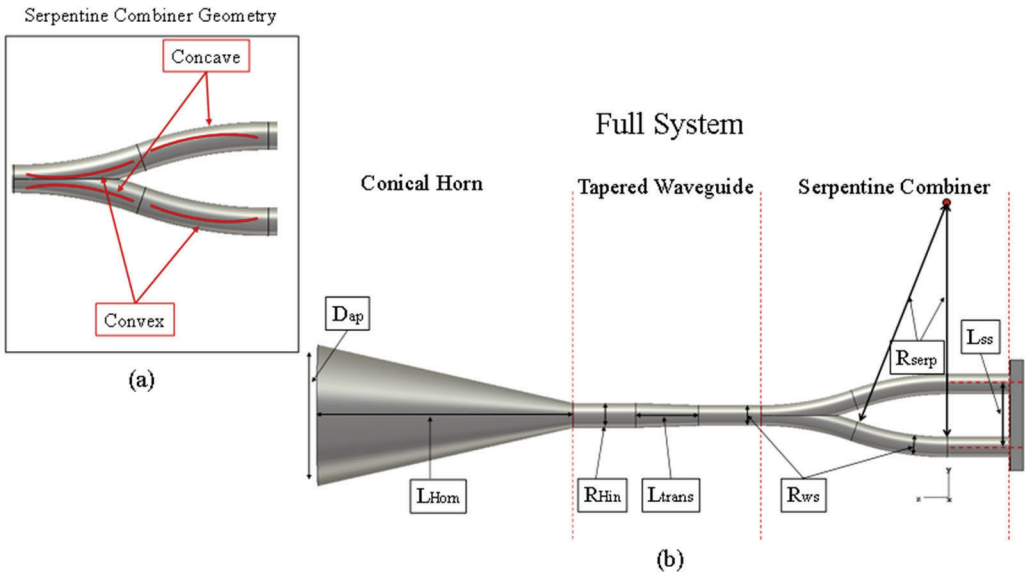

Figure 84. (a) Illustration of the Serpentine Combiner Geometry, (b) Illustration of the Different Parts of the System Combined

The separation between the slots L_{ss} along with R_{serp} is shown in Figure 84. They were chosen in a way that made each section of the serpentine input waveguides well-matched with the serpentine output waveguide. If this matching was not done correctly, a standing-wave is seen in the section of the waveguide that extracts the least power, causing the efficiency of the combiner to drop. In this design, the separation between the slots was optimized to be L_{ss} = 10 mm for R_{serp} = 45 mm. All these factors were essential in making sure that the wave extracted from the rectangular waveguide was circularly polarized and that the extraction process had minimal losses.

3.4.3 Dual Slot Polarizer Using A Square Waveguide Power Combiner

In this section, an improvement to the performance of a single-slot polarizer with a square waveguide extraction is presented. The improvement relies on the use of two slots in the rectangular waveguide with their powers combined using square waveguide combiners. The design and improvements are discussed in what follows.

3.4.3.1 Dual Slot Design

Same as in the case of the serpentine combiner, the first step in designing this system was the design of the cross slots. By determining the right configuration of the slots, the bandwidth and efficiency of the system were improved. Two different scenarios were considered for this matter and explained below.

3.4.3.1.1 Scenario 1. Slots Have the Same Resonant Frequency

For this scenario, the slots had the same dimensions, which led to the same resonant frequency. The aim of this design was to increase the isolation between ports 1 and 2 to very high values and to have the best axial ratio values between the different components of the electric field. The slots used in this design had dimensions given in Table 16.

Table 16. Dimensions of the *z*-shaped Arm Cross-Slots at 72 GHz Used in the Square Waveguide Power Combiner

Parameter	Description	Value		
		Scenario 1	*Scenario 2*	
			Slot 1	*Slot 2*
L_{z1}	long arm length	1.85 mm	1.85 mm	1.80 mm
L_{z2}	short arm length	0.46 mm	0.46 mm	0.46 mm
W_a	arm width	0.15 mm	0.15 mm	0.15 mm
S	slot center position	0.69 mm	0.69 mm	0.69 mm
α_2	arm angle with y-axis	46°	46°	46°
t_{w3}	slot thickness	0.4 mm	0.4 mm	0.4 mm

3.4.3.1.2 Scenario 2. Slots Have Close Resonance Frequencies

In this scenario, the slots had dimensions that were different but very close. This configuration of the slots resulted in a wider bandwidth of operation of the polarizer and in higher efficiencies of the system over a wider frequency range than in scenario 1. The dimensions of the slots are given in Table 16.

The slots were located on the broad wall of a WR-12 waveguide and had a separation distance of L_{ss} = 6 mm for both scenarios. For both scenarios, the frequency of operation was close to 72 GHz. The coupling between the slots along with the dimensions of the slots contributed to the frequency shift between the different designs.

3.4.3.2 Full System Design

The square waveguide combiner, shown in Figure 85, had two square waveguide inputs and one square waveguide output. The square waveguide inputs had a cross section width of $a_{s\_in1} = a_{s\_in2}$ = 2.4 mm, while the square waveguide output had a cross section width a_{s_out} = 2.7 mm. The input waveguide cross section width plays a role in the efficiency of the extraction of power from the rectangular waveguide. On the other hand, the output waveguide cross section width plays a role in the matching of the power combiner. The output waveguide was located at the same distance from the two input waveguides. This position ensured that the power combined from each input waveguide did not "bounce" upon reaching the output waveguide. It also ensured that the power from both waveguides did not add-up off the centerline of the output waveguide, causing beam "squinting" in the radiation pattern.

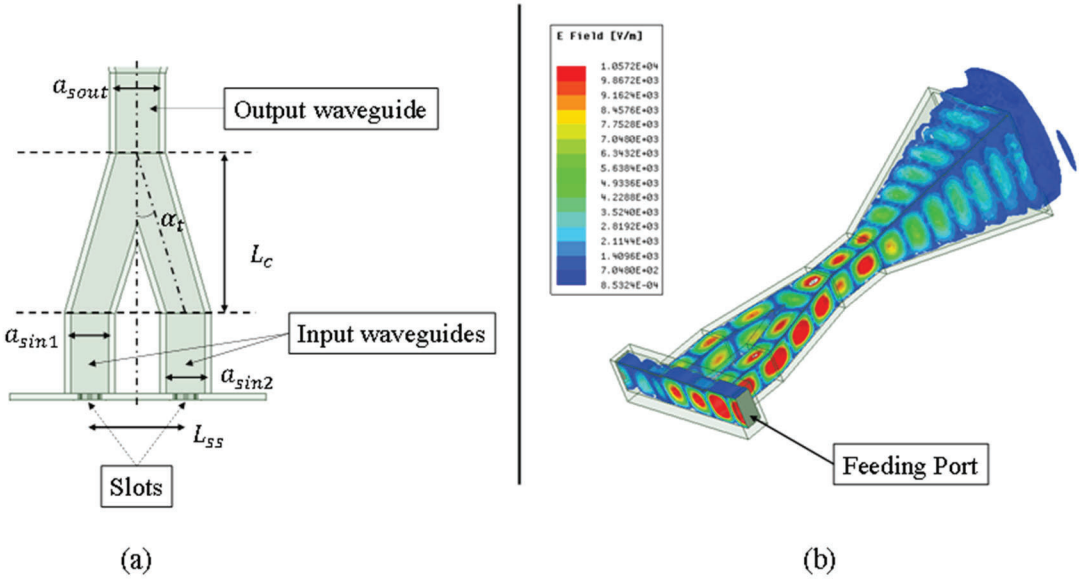

Figure 85. (a) The Layout and the Different Parameters of the Square Waveguide Combiner; (b) The E-field Inside the Different Sections of the Full System at 72 GHz When a Pyramidal Horn is Connected

The power combiner had its input and output waveguides connected by tapered tilted waveguides. The taper in the connecting waveguides plays an essential role in better matching the entire design, since the waveguides it is connecting have different cross-section widths. The taper causes minimal reflection to occur at the connection with the output waveguide of the power combiner. The tilting angle, α_t, of the waveguides was optimized in a way that minimized scattering at the intersection plane of the waveguides. This scattering might reflect back into the input waveguides and cause a standing wave. This phenomenon reduces the efficiency of the power combiner. For a power combiner working at 72 GHz, the tilting angle was α_t = 16.7°. The separation between the output of the input waveguides and the input of the output waveguides was L_c = 10 mm.

4 RESULTS AND DISCUSSION

4.1 W/V-band Terrestrial Link Experiments – Results and Analysis

4.1.1 Optical Thickness Calculated Using the Standard Atmosphere Model

It is informative to calculate the optical thickness for the WTLE propagation path assuming the Standard Atmosphere model. The scenario is illustrated in Figure 86. The approach was given by Eq. (51). Using Δh = 1 m and f_1 = 72.5 GHz, we find that τ_1 = 4.15 dB. For f_2 = 82.5 GHz, τ_2 = 2.62 dB. As reference, the zenith opacity from sea level was 1.31 dB and 0.80 dB for 72.5 GHz and 82.5 GHz, respectively. **Thus, the zenith opacity is substantially less than the WTLE slant path optical thickness.**

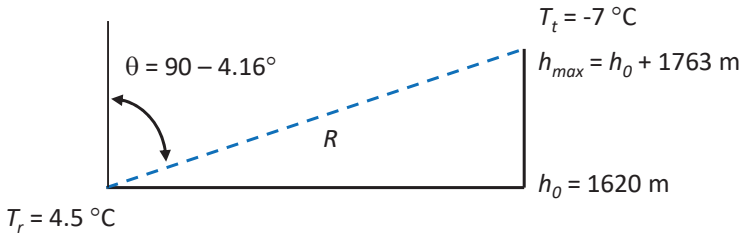

Figure 86. Model For WTLE Link Optical Thickness Calculation Using Standard Atmosphere Model

4.1.2 Optical Thickness Calculated Using WTLE Data – Clear Conditions

Figure 87 shows photographs from the receiver and transmitter sites for clear day measurements. Small green boxes are included on Figure 87 to indicate the transmitter and receiver locations. Data were collected over 4 days; 0000 UTC (Universal Coordinated Time) 25 April 2018 through 2359 UTC 28 April 2018. Figure 88 shows plots of (1) visibility sensor range from the transmitter site, (2) atmosphere temperature at the transmitter and receiver sites, (3) barometric pressure at the transmitter and receiver sites, and (4) relative humidity at the transmitter and receiver sites. The sample rate was (1/60) Hz (i.e., one sample per minute). Data were low-pass filtered to mitigate the effects of electronic noise, atmospheric turbulence (scintillation), and transients resulting from changes to the experiment system (i.e., wind-load of the receiver antenna or other abrupt environmental effects). Vertical dashed lines are superimposed to indicate midnight (12 AM) local time as reference for the reader.

The visibility sensor shows that visibility exceeded 7000 m over the 4 day period, which indicates clear conditions. The temperature plots illustrate daily temperature oscillations at both the transmitter and receiver sites. The receiver site was typically 10 °C (or 18-20 °F) warmer than the transmitter site. The pressure plots show little variation over the 4 day period. The mean pressure at COSMIAC was 839.7 hPa, while the mean pressure at Sandia Crest was 691.6 hPa, a difference

of 148.1 hPa. The atmospheric pressure at Sandia Crest was 82% of the atmospheric pressure at COSMIAC. The relative humidity plots show that the receiver site typically had lower relative humidity than the transmitter site. The mean relative humidity at Sandia Crest was 36%, while the mean relative humidity at COSMIAC was 27%.

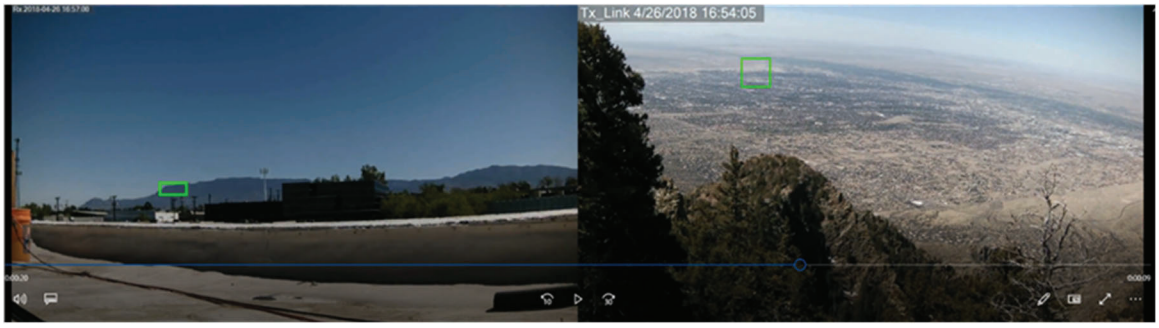

Figure 87. Photos of Clear Conditions; (Left) From Receiver, (Right) From Transmitter

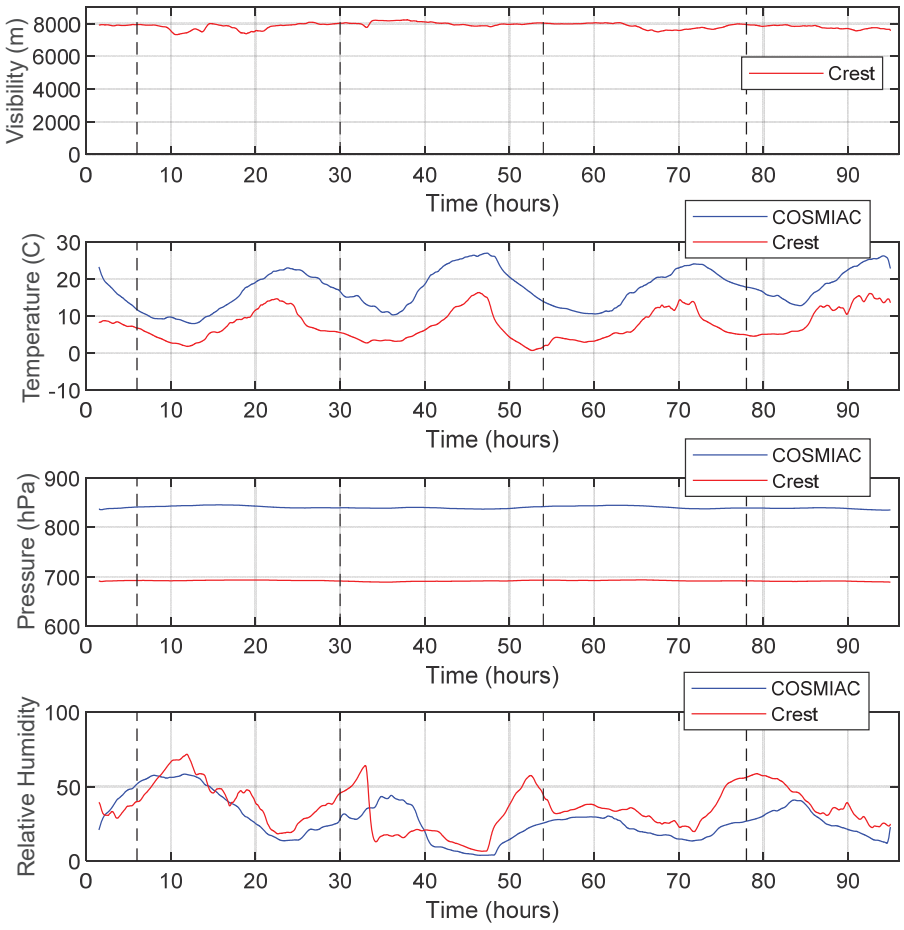

Figure 88. Measured WTLE Weather Data (Clear Conditions)

Measured data presented in Figure 88 were interpolated from h_0 = 1620 m to h_{max} = 3383 m at each time sample. Temperature and relative humidity were linearly interpolated, while pressure was interpolated using an exponential scale. This enabled calculation of the specific attenuation as a function of altitude for 72.5 GHz and 82.5 GHz. The specific attenuation was then numerically integrated to find the oblique optical thickness, which is plotted in Figure 89. For comparison, the oblique optical thickness computed using the Standard Atmosphere model is superimposed. Although the optical thickness fluctuated over time, the mean value at f_1 = 72.5 GHz was τ_1 = 4.11 dB, which is consistent with the value calculated using the Standard Atmosphere model (i.e., 4.15 dB). The mean value of the optical thickness at f_2 = 82.5 GHz was τ_2 = 2.95 dB, which is slightly above the value calculated using the Standard Atmosphere model (i.e., 2.62 dB). **It is remarkable that the mean oblique optical thickness over a 4-day period so closely matched the values calculated using the Standard Atmosphere model.**

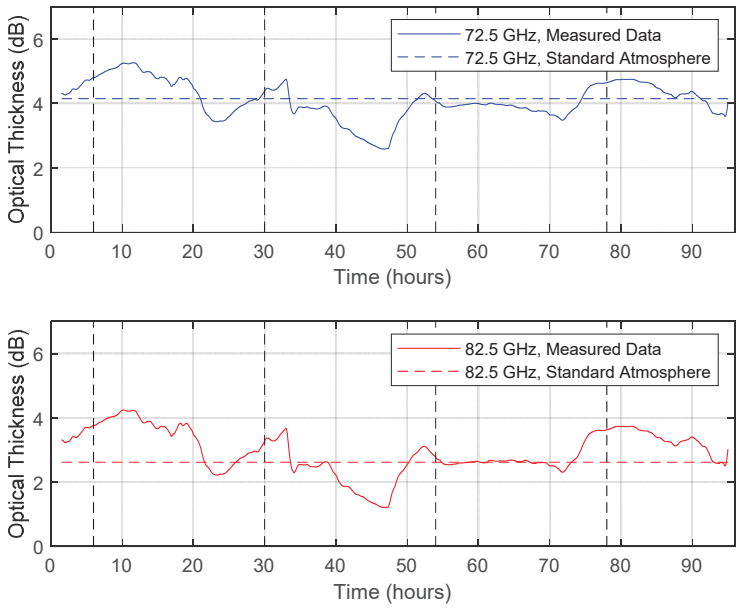

Figure 89. WTLE Oblique Optical Thickness Computed Using Measured Weather Data (Clear Conditions)

Let's now use the oblique optical thickness just calculated for 72.5 GHz to estimate the received signal power over the 4-day period. We will use the link budget parameters given in Table 13 and assume that the transmitted power (5 mW) was constant over the 4-day period. Figure 90 shows the estimated received signal power resulting from including the atmosphere optical thickness shown in Figure 89 (top). For reference, the received signal power from the link budget (Table 13) is superimposed.

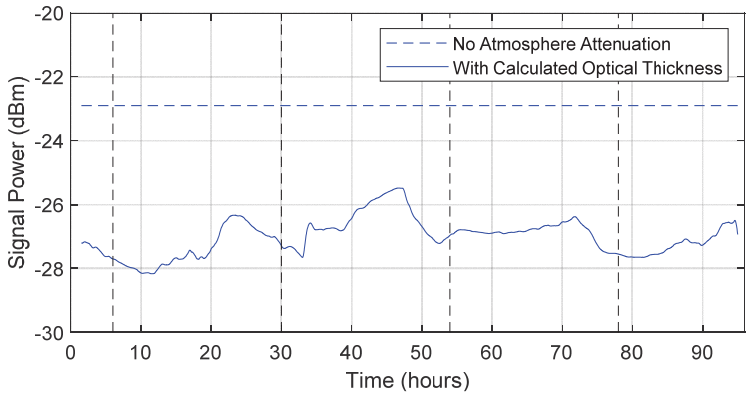

Figure 90. Estimated WTLE Received Signal Power at 72 GHz (Clear Conditions)

Figure 91 compares the ***estimated*** received signal power to the ***measured*** signal power. The sample rate for the measured signal was 1 Hz, but the data were down-sampled to (1/60) Hz (i.e., one sample per minute) and then low-pass filtered. Vertical dashed lines are superimposed to indicate midnight (12 AM) local time. **The similarity between the measured WTLE signal (72 GHz) and the estimated signal (72.5 GHz) based on the oblique optical thickness calculations is remarkable.** Not only do the daily trends closely match, but the variations over multiple days correspond reasonably well. The mean of the estimated received signal power was -27.01 dBm, and the mean of the actual received signal power was -26.90 dBm.

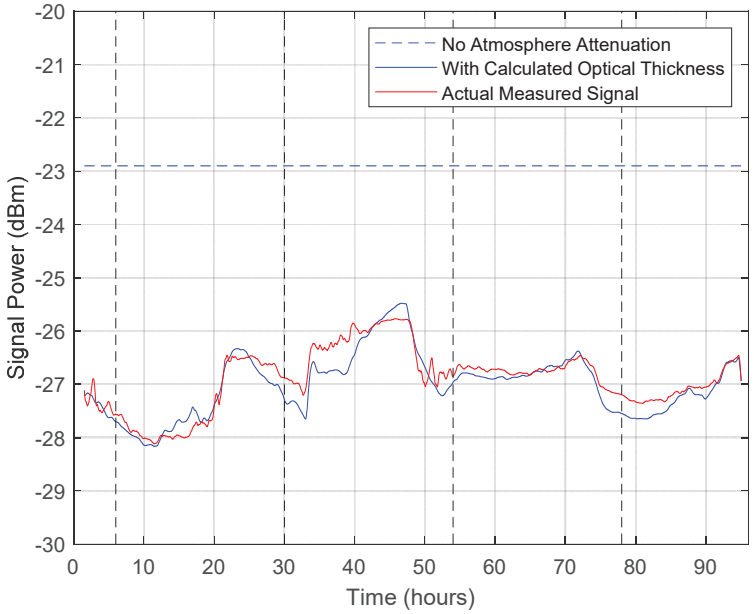

Figure 91. Comparison of Measured WTLE Signal to Estimated Signal (72 GHz) (Clear Conditions)

4.1.3 Optical Thickness Calculated Using WTLE Data – Cloudy Conditions

Next, we consider WTLE data measured during cloudy conditions and without precipitation. Figure 92 shows photographs taken from the receiver and transmitter sites during cloudy conditions. Small green boxes indicate the transmitter and receiver locations. The presence of a stratus cloud on part of the propagation path is apparent, but the thickness and LWC were unknown.

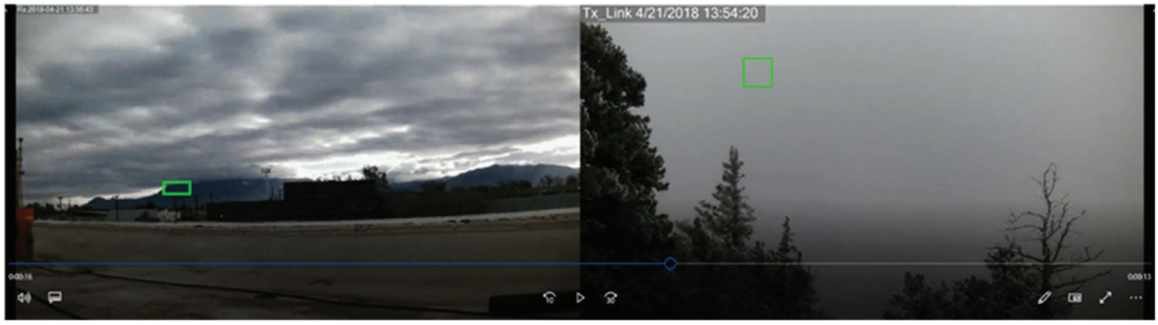

Figure 92. Photos of Cloudy Conditions; (Left) From Receiver, (Right) From Transmitter

The data presented here were collected starting 20 April 2018 and going through 22 April 2018. Figure 93 shows plots of (1) visibility sensor range from the transmitter site, (2) atmosphere temperature at the transmitter and receiver sites, (3) barometric pressure at the transmitter and receiver sites, and (4) relative humidity at the transmitter and receiver sites. The sample rate was (1/60) Hz (i.e., one sample per minute). Data were low-pass filtered to mitigate the effects of electronic noise, atmospheric turbulence (scintillation), and transients resulting from changes to the experiment system (i.e., wind-load of the receiver antenna or other abrupt environmental effects). Vertical dashed lines are superimposed to indicate midnight (12 AM) local time.

The visibility sensor shows the occurrence of three deep fades during the time period, where visibility was reduced to less than 300 m. This indicates clouds were on the propagation path around the hours of 30, 35, and 40. Clouds-at-a-distance are indicated at hour 13.

The temperature plots show that the temperature at Sandia Crest dropped a few degrees below freezing during the cloud events. This does not necessarily imply glaciation. Mixed-phase or super-cooled liquid droplets are likely. The pressure plots show little variation over the measurement period.

The relative humidity plots show that the measured relative humidity at the transmitter site exceeded 95% during the cloud events. Note that the relative humidity at the Crest was ~90% at hour 13. Also note that the relative humidity at COSMIAC was ~70% at hour 62, although the visibility sensor indicated clear conditions.

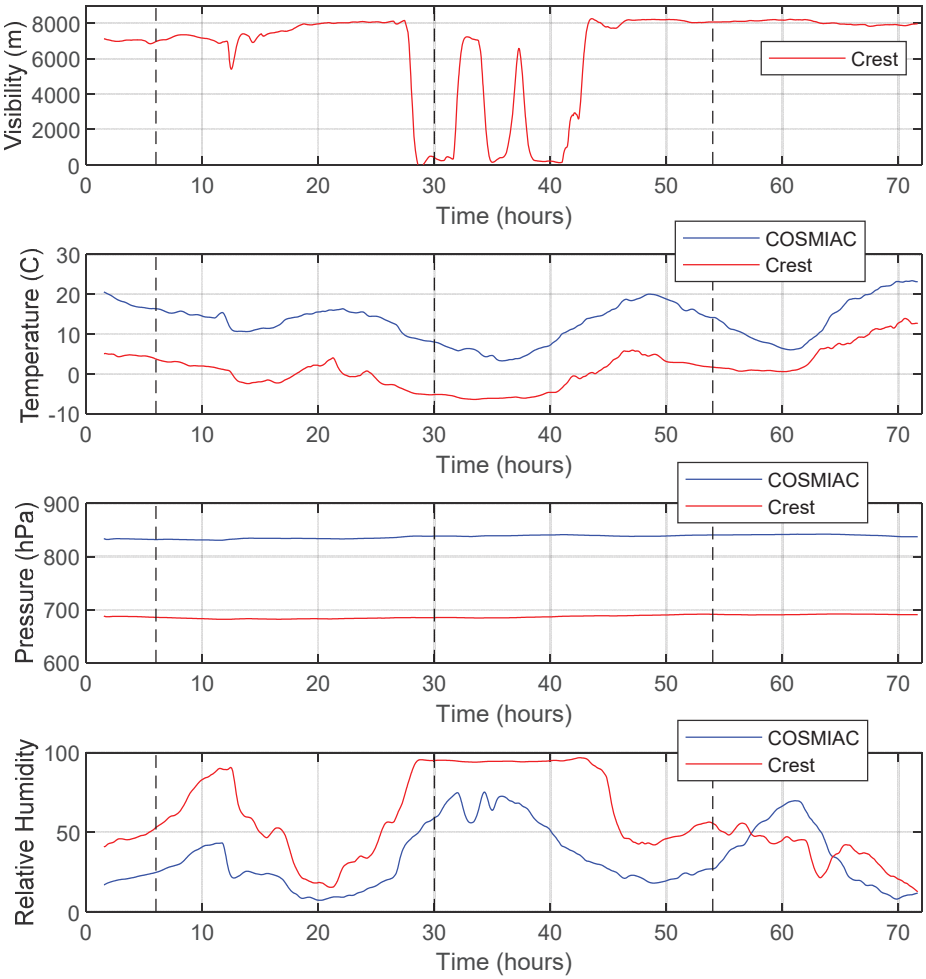

Figure 93. Measured WTLE Weather Data (Cloudy Conditions)

As with the clear-day case, measured data presented in Figure 93 were interpolated from $h_0 = 1620$ m to $h_{max} = 3383$ m at each time sample. Temperature and relative humidity were linearly interpolated, while pressure was interpolated using an exponential scale. This enabled calculation of the specific attenuation as a function of altitude for 72.5 GHz and 82.5 GHz. The specific attenuation was then numerically integrated to find the oblique optical thickness, which is plotted in Figure 94. For comparison, the oblique optical thickness computed with the Standard Atmosphere model is superimposed. The mean value at $f_1 = 72.5$ GHz was $\tau_1 = 4.38$ dB. The mean value at $f_2 = 82.5$ GHz was $\tau_2 = 3.17$ dB. As expected, these are higher than in the case of clear conditions.

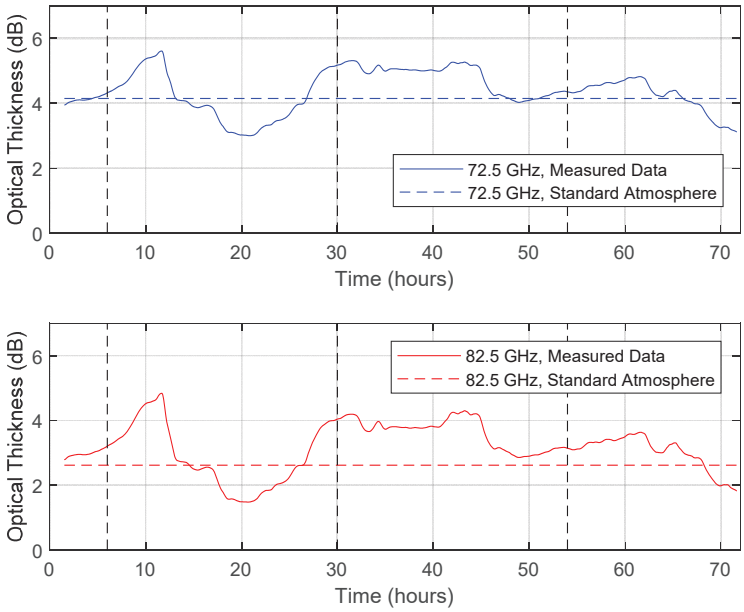

Figure 94. WTLE Oblique Optical Thickness Computed Using Measured Weather Data (Cloudy Conditions)

Let's now use the oblique optical thickness just calculated for 72.5 GHz to estimate the received signal power over the 3-day period. We will use the link parameters given in Table 13 and assume that the transmitted power (5 mW) was constant over the 3-day period. Figure 95 shows the estimated received signal power resulting from including the atmosphere optical thickness shown in Figure 94 (top). For reference, the received signal power from the link budget (Table 13) is superimposed.

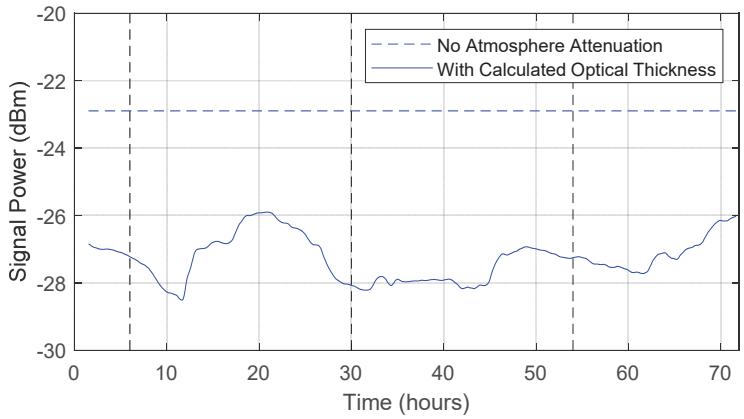

Figure 95. Estimated WTLE Received Signal Power at 72 GHz (Cloudy Conditions)

Figure 96 compares the ***estimated*** received signal power to the ***measured*** signal power. The sample rate for the measured signal was 1 Hz, but the data were down-sampled to (1/60) Hz (i.e., one sample per minute) and then low-pass filtered. Vertical dashed lines are superimposed to indicate midnight (12 AM) local time. The mean of the estimated received signal power was -27.28 dBm. The mean of the actual received signal power was -27.25 dBm.

The measured data indicate signal fades around the hours of 30, 35, and 40. The fades are approximately 2.5 dB, 0.6 dB, and 4.5 dB, respectively. Obviously, theses fades resulted from clouds on the WTLE path, and given the magnitude of the fades, the clouds were not glaciated. Next, we re-visit the different modeling approaches to estimate cloud attenuation.

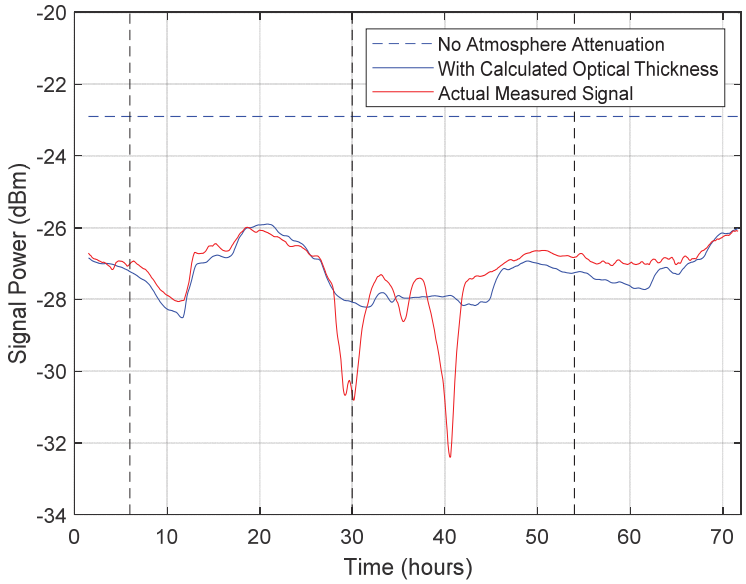

Figure 96. Comparison of Measured WTLE Signal to Estimated Signal (72 GHz) (Cloudy Conditions)

4.1.3.1 Adiabatic Lifting Model

For each minute during the 3-day period, conditions at COSMIAC (h_0) were used to define an air parcel, which was then adiabatically lifted to determine if it would saturate before the altitude corresponding to Sandia Crest (h_{max}). If saturation was achieved, then the lifted condensation level (LCL) occurred below h_{max} and a cloud was assumed to have formed along the propagation path. For this study, we assumed that the cloud base occurred at the LCL and that cloud thickness extended to h_{max}.

Values of the liquid extinction coefficient, k_L, were computed using the temperature profile of the lifted parcel from LCL to h_{max}. A stratus cloud was assumed with constant LWC of $m_L = 0.25$ g/m^3. The propagation path length, R, was estimated simply as the cloud thickness, $\Delta h_{cl} = h_{max} - \text{LCL}$.

The optical thickness (i.e., attenuation) of the cloud was then calculated by numerical integration following Eq. (60) and the description provided in Figure 49.

The results are shown in Figure 97. Vertical dashed lines are superimposed to indicate midnight (12 AM) local time. There was only a minor increase to attenuation at hour 13. There was broad increase of ~1 dB of attenuation from hours 28 – 42, which was expected since the relative humidity at COSMIAC was elevated (refer to Figure 93). There was a false indication of a cloud at hour 62, which also corresponded to elevated relative humidity at COSMIAC. The model was not able to predict the deep fades at hours 30 and 40. The mean of the estimated received signal power for the 3-day period with the adiabatic lifting cloud model as shown was τ_1 = -27.51 dBm. Adjusting the LWC and/or effective path length are tuning options, but in this case, would not improve the estimate. Any improvements at hours 30 and 40 would likely be negated by increased error at hour 62.

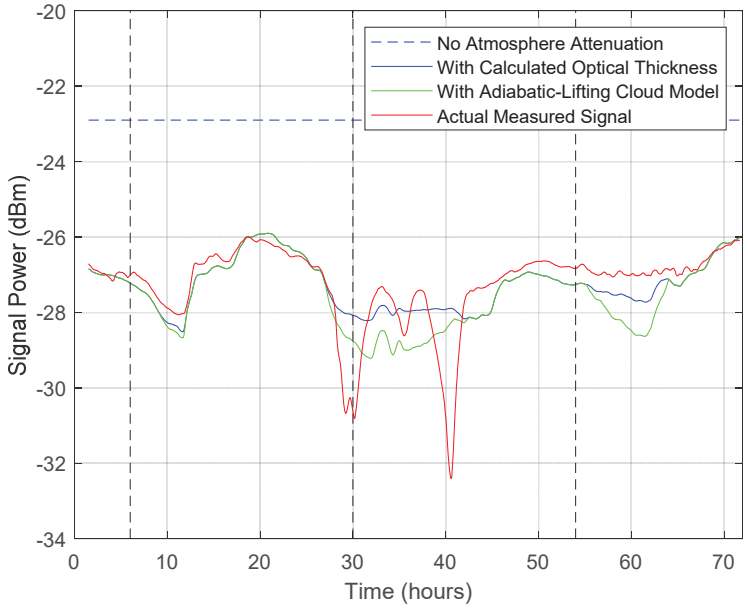

Figure 97. Comparison of Measured WTLE Signal to Estimated Signal (72 GHz) (Cloudy Conditions) – Using Adiabatic Lifting Cloud Model

4.1.3.2 Decker Model

The Decker model used temperature, pressure, and relative humidity data interpolated from WTLE weather sensor data to estimate cloud LWC, LCL, and cloud thickness. The relative humidity threshold was set to 90%. The propagation path length, R, was estimated as $R = 3(\Delta h_{cl})$. The results are shown in Figure 98. Vertical dashed lines are superimposed to indicate midnight (12 AM) local time. The Decker model with 90% threshold did ***not*** provide false indications of clouds at hour 13 or 62, which is an improvement over the adiabatic lifting model. It did indicate cloud attenuation between hours 30 and 40, although it did not predict the deep fade at hour 40. The mean of the

estimated received signal power for the 3-day period with the Decker model as shown was τ_1 = -27.51 dBm, which is the same as the adiabatic lifting model.

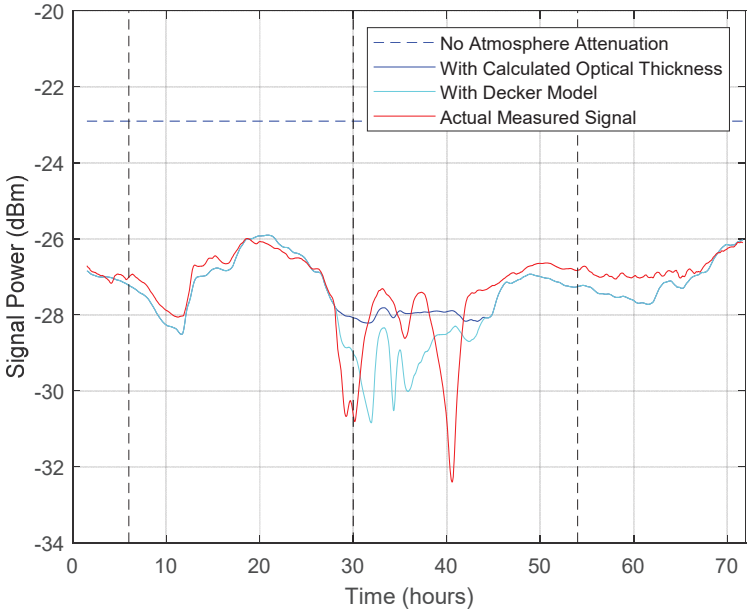

Figure 98. Comparison of Measured WTLE Signal to Estimated Signal (72 GHz) (Cloudy Conditions) – Using Decker Model

4.1.3.3 Salonen Model

The Salonen model used temperature, pressure, and relative humidity data interpolated from WTLE weather sensor data to estimate cloud LWC, LCL, and cloud thickness. It provided a variable estimate of the LWC based on the temperature and cloud thickness. The critical relative humidity was a function of the dry air pressure and water vapor pressure profile, and therefore varied with altitude. The propagation path length was estimated as $R = 3(\Delta h_{cl})$, which is consistent with the Decker model. Other parameters used for the Salonen model included $\alpha = 1.0$, $\beta = \sqrt{3}$, $w_0 = 1.7$ g/m^3, and $h_r = 1500$ m.

The results are shown in Figure 99. Vertical dashed lines are superimposed to indicate midnight (12 AM) local time. The Salonen model provided a false indication of clouds at hour 13. It did not provide false indication at hour 62. The response between hours 30 and 40 is very similar to the Decker model. The mean of the estimated received signal power for the 3-day period with the Salonen model as shown was τ_1 = -27.74 dBm.

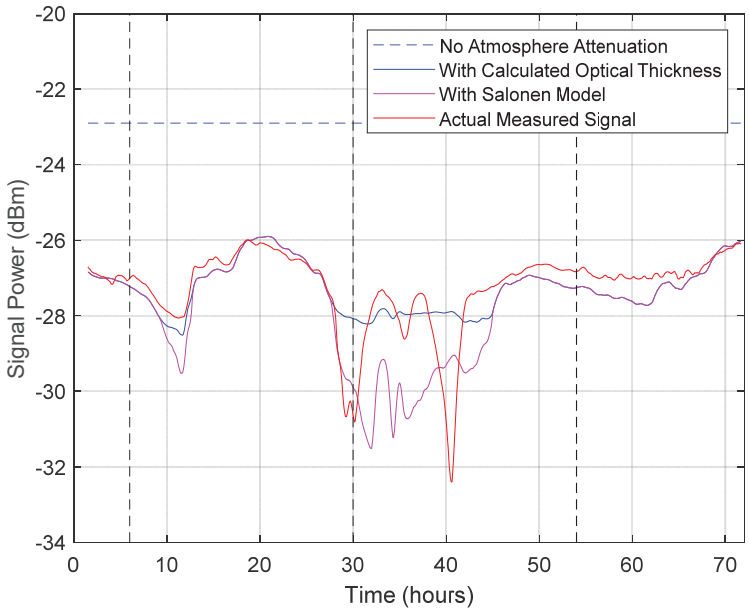

Figure 99. Comparison of Measured WTLE Signal to Estimated Signal (72 GHz) (Cloudy Conditions) – Using Salonen Model

4.1.3.4 Mattioli Model

Finally, we consider the Mattioli model, which also used temperature, pressure, and relative humidity data interpolated from WTLE weather sensor data to estimate cloud LWC, LCL, and cloud thickness. It also provided a variable estimate of the LWC based on the temperature and cloud thickness. The critical relative humidity varied with altitude, although it was more conservative than the calculation used for the Salonen model. The propagation path length was estimated as $R = 3(\Delta h_{cl})$, which is consistent with the Decker model. Other parameters used for the Mattioli model included $\alpha = 0.59$, $\beta = 1.37$, as presented in section 3.

The results are shown in Figure 100. Vertical dashed lines are superimposed to indicate midnight (12 AM) local time. The Mattioli model did not provide false indications of clouds at hour 13 or 62. The response between hours 30 and 40 was similar to the Decker and Salonen models, although the amount of LWC, and thus attenuation, was less. The mean of the estimated received signal power for the 3-day period with the Mattioli model as shown was $\tau_1 = -27.41$ dBm. Recall that the mean of the actual received signal power was -27.25 dBm. Adjusting the LWC or effective path length would not improve the model's ability to predict the deep fades at hours 30 and 40. It is noteworthy that the Mattioli model's attenuation estimate was very similar to the attenuation estimate from the adiabatic lifting model, with the exception that Mattioli did not give a false positive at hour 62.

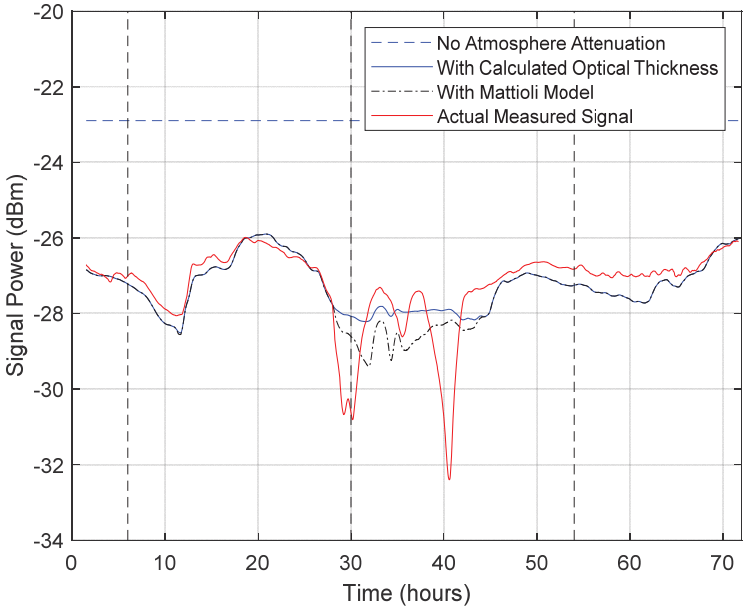

Figure 100. Comparison of Measured WTLE Signal to Estimated Signal (72 GHz) (Cloudy Conditions) – Using Mattioli Model

4.2 Rectangular Waveguide Antenna Array Measured Results

The entire array structure as fabricated is shown in Figure 101. The antenna operating bandwidth was 84.1 – 85.8 GHz for port 1, and 84.35 – 86 GHz for port 2 as depicted in Figure 102. The measurement results showed an acceptable agreement with the simulated results. In fact, port 1 exhibited a slightly different yet tolerable performance. The slight discrepancy was due to some of the fabrication imprecisions (5-10 μm) in terms of milling the various slots in addition to the assembly misalignment. Both ports shared a 1.45 GHz operating bandwidth extending between 84.35 – 85.8 GHz. The antenna had great isolation between both ports, since the measured isolation between the ports was more than 20 dB over the frequency of operation as shown in Figure 102.

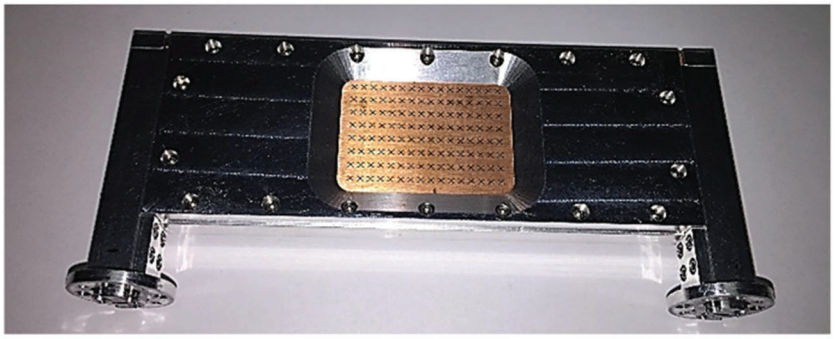

(a)

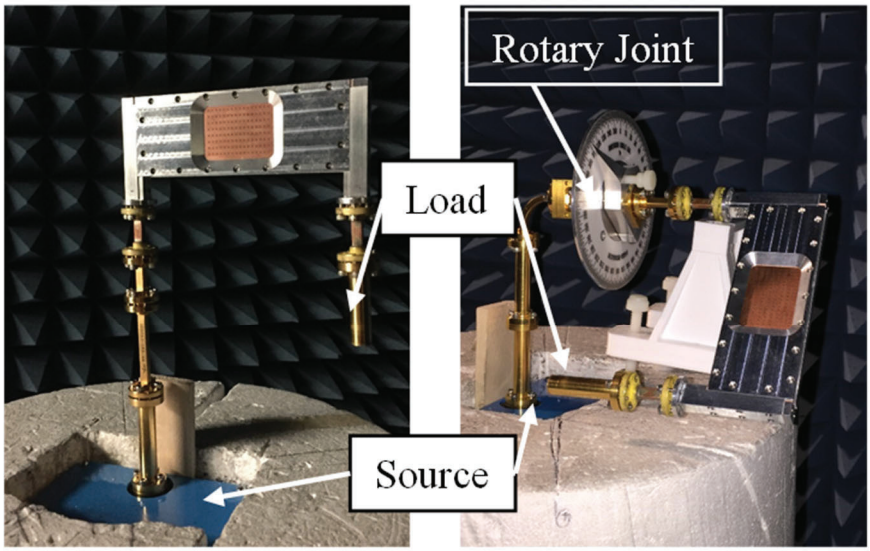

(b) (c)

Figure 101. (a) Antenna Prototype, (b) Radiation Pattern Measurement Setup in the Elevation Plane ($\phi = 0°$), and (c) Azimuthal Plane ($\theta = 40°$)

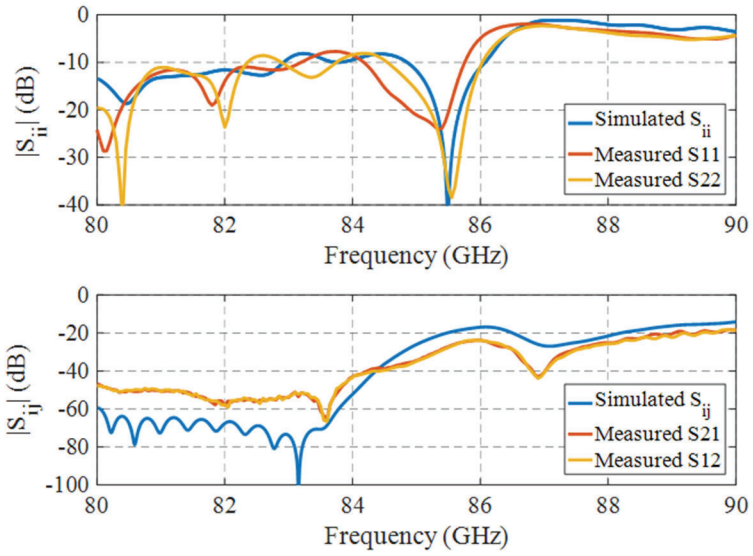

Figure 102. (Top) Simulated and Measured Results for the Reflection Coefficient at Both Ports; (Bottom) Simulated and Measured Isolation Between the Two Ports

The antenna's radiation pattern was measured in the azimuthal ($\theta = 40°$) and elevation ($\phi = 0°$) planes over different frequencies in the operating bandwidth. The measurement setup for both planes is shown in Figure 101(b) and Figure 101(c). A waveguide rotary joint was used for the azimuthal plane ($\theta = 40°$) measurement. When port 1 was fed, port 2 was loaded with a WR-12 waveguide matched-load and vice versa. The comparison between the simulated and measured gain patterns at $f = 85$ GHz and when feeding either port 1 or 2 are summarized in Figure 103 for the elevation plane ($\phi = 0°$) and in Figure 104 for the azimuthal plane ($\theta = 40°$). The measured gain patterns at 85 GHz prove that when the antenna was fed through port 1, it created a RHCP main beam in the elevation plane in the direction $\theta = 40°$. When it was fed through port 2, the antenna created a LHCP main beam in the elevation plane in the direction $\theta = -40°$. These results show that the change in port feeding caused the polarization to switch from LHCP to RHCP.

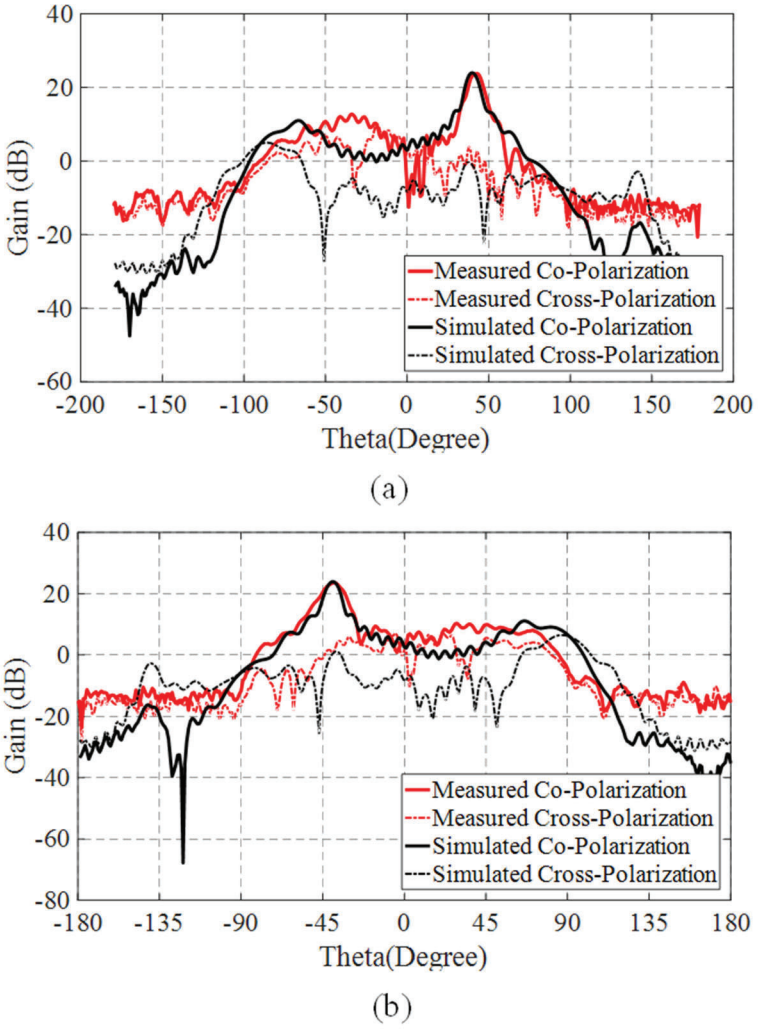

Figure 103. Simulated and Measured Gain Patterns of the Array in the Elevation Plane (ϕ=0°) at 85 GHz When (a) Port 1 is Fed, or (b) Port 2 is Fed

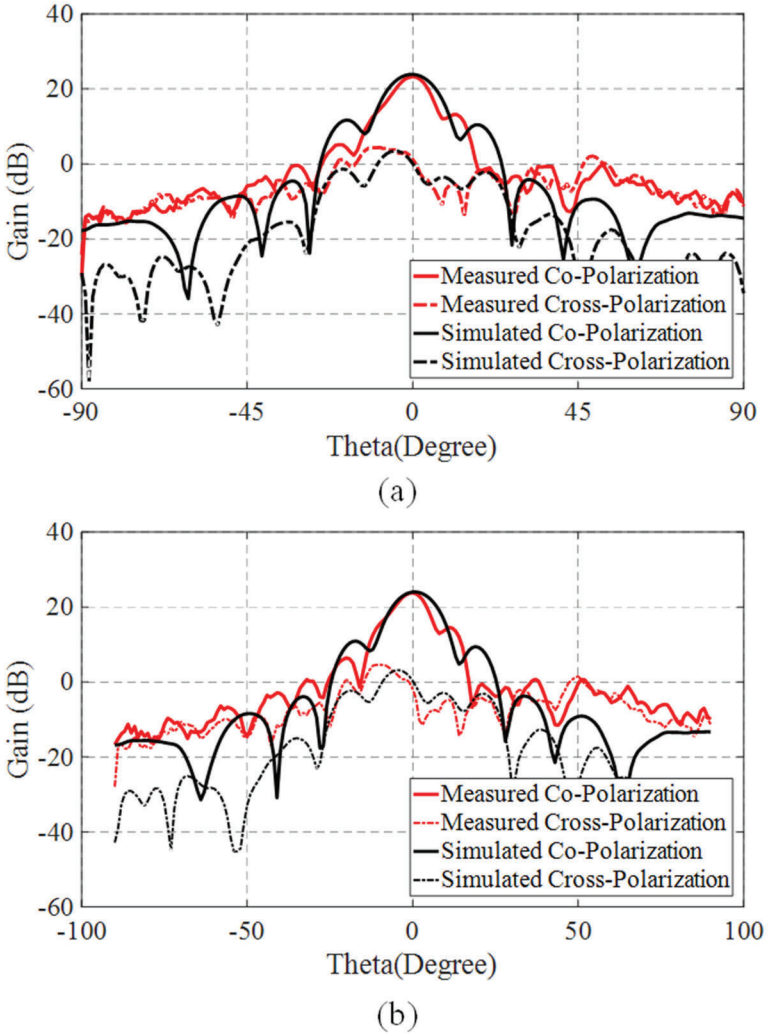

Figure 104. Simulated and Measured Gain Patterns of the Array in the Azimuth Plane (θ=40°) at 85 GHz When (a) Port 1 is Fed, or (b) Port 2 is Fed

The antenna's calculated RHCP gain was between 23.26 dB and 24.09 dB over the operating bandwidth as shown in Table 17. The calculated LHCP gain was between 23.2 dB and 24.35 dB, also given in Table 17. The measured results at 85 GHz showed that in the elevation plane, the antenna's measured HPBW was $\Theta_{ep} = 8°$. It was entirely circularly polarized for both polarizations. The sidelobe level was around 12 dB. The maximum grating lobe level was around 13.5 dB for both polarizations as shown in Figure 103. In the azimuthal plane, the antenna's HPBW was $\Theta_{ap} = 12°$ and it was entirely circularly polarized for both polarizations. The antenna's sidelobe level in this plane was around 11.5 dB for RHCP and 10.5 dB for LHCP as shown in Figure 104.

Table 17. The Array Calculated Gain for Both Ports at Different Frequencies

Frequency	RHCP Gain		LHCP Gain	
	Simulated	Measured	Simulated	Measured
84.35 GHz	21.5 dB	23.72 dB	21.5 dB	23.2 dB
84.5 GHz	23.1 dB	24.09 dB	23.1 dB	23.7 dB
85 GHz	23.31 dB	23.76 dB	23.31 dB	24.33 dB
85.3 GHz	24.07 dB	23.83 dB	24.07 dB	24.35 dB
85.5 GHz	24.4 dB	23.79 dB	24.4 dB	23.92 dB
85.7 GHz	24.5 dB	23.26 dB	24.5 dB	23.86 dB

The isolation between RHCP and LHCP in the direction of the maximum gain for both ports were measured. In the frequency of operation of both ports, the isolation level was found to be more than 18 dB and reached 26 dB in certain cases as shown in Figure 105. For the frequency band 84.4 – 85.55 GHz, both ports produced an isolation of more than 20 dB.

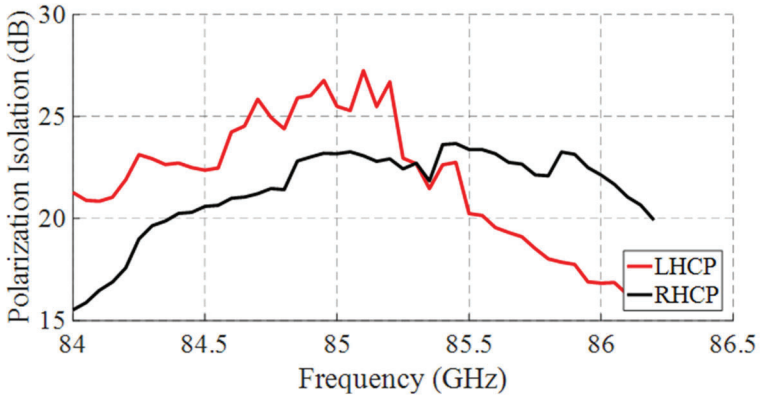

Figure 105. Isolation Between the Co- and Cross-Polarization in the Direction of the Maximum Gain

Table 18 compares the proposed design in this work with the ones available in the literature. In general, slotted rectangular waveguide arrays designed for millimeter-wave generate a gain close to 25 dB with an efficiency higher than 70%. These characteristics are close to the results presented in this work. However, the arrays operating at W-band were linearly polarized, while the arrays we developed were circularly polarized with the ability to generate both LHCP and RHCP waves.

Table 18. Comparison Between Different Planar Slotted Waveguides Working at Millimeter Wave Frequencies

Reference	Frequency (GHz)	Gain (dB)	Polarization	Efficiency	Size
SIW 2D Array	81.75	14	Linear	50%	2x8
2D Slot array	94	26.8	Linear	81.9%	8x8
Ka-band X-slot array	30	22.9	RHCP	74%	16x1
Dual linear Polarization	30 / 35	24.8 / 25.4	VP/HP	N/A	8x10 / 9x10
This work	85	24	LH/RH CP	82%	8x16

4.3 Cross-Slotted Waveguide-Fed Horn Antenna Results

4.3.1 Single Slot Conical Horn

The 72 GHz system was fabricated and tested. The system assembly is shown in Figure 106. The cross slot was fabricated on two sheets of copper with thickness 0.2 mm each using a laser cutting machine. The copper sheets were stacked as shown in Figure 106. The circular waveguides along with the tapered waveguide were fabricated in a separate aluminum block, component (1) in Figure 106. This block contained an area where the sheets with the cross slot can fit and be flat with the bottom of the block. Finally, the WR-12 waveguide channel was fabricated using mechanical milling onto a separate aluminum block (3) in Figure 106. The two different aluminum blocks sandwich the copper sheet and the whole design was aligned using alignment pins. The whole design was screwed together and the gaps between the different blocks were suppressed to the order of 1 μm, which doesn't affect the functionality of the fabricated polarizer.

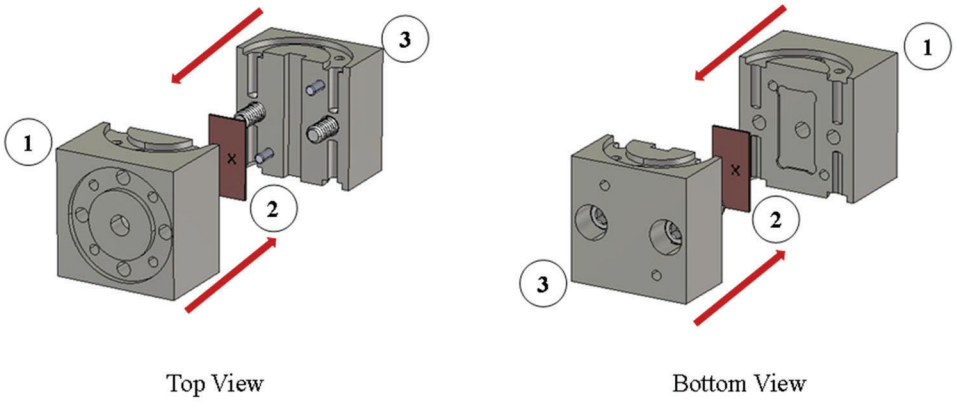

Figure 106. Polarizer Assembling Technique

The polarizer was tested for *s*-parameters while a conical horn was connected to it and while the circular waveguide output was left open as shown in Figure 107. Both scenarios led to the same results, proving that the polarizer parameters were barely affected by the device connected to the circular waveguide output. The measured results show that the resonant frequency of the slot was shifted down by 500 MHz and occurred at 71.25 GHz as shown in Figure 108. This shift was caused by the fabrication errors caused by the laser prototyping machine that was used to cut out the slots leaving a slot width larger on the top level than the bottom level of the copper sheet. The reflection coefficient of both feeding ports was less than -14 dB for the entire operating frequency range.

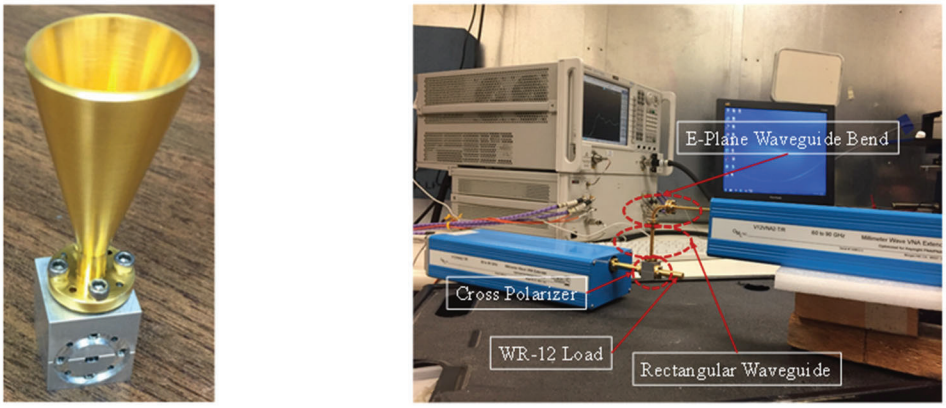

(a) (b)

Figure 107. (a) The Conical Horn Attached to the Polarizer; (b) the Measurement Setup for the *s*-Parameters of the Polarizer

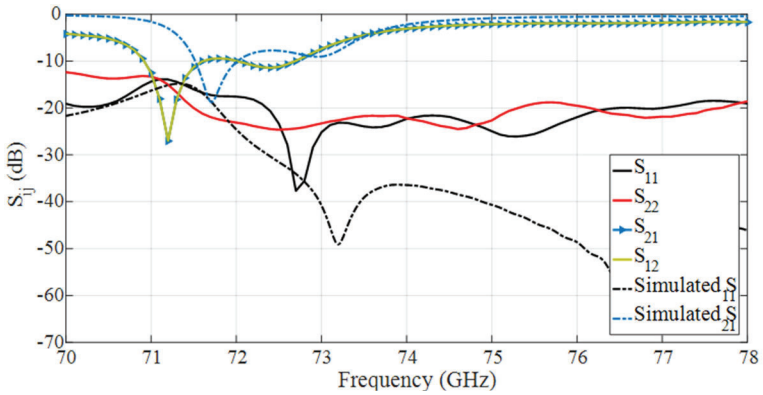

Figure 108. Plot of the Measured *s*-Parameters of the Polarizer

In an attempt to measure the E-field power and phase of the two orthogonal TE_{11} modes at the output of the circular waveguide, a rectangular waveguide with a waveguide bend was connected to the circular waveguide output directly as shown in Figure 107. The connection allowed the measurement of one of the modes and then the rectangular waveguide was rotated by 90° to measure the other mode. The direct connection caused reflections at the output of the circular waveguide, which made the power reading inaccurate, but still allowed us to measure the power difference and phase difference between the two excited modes.

The power measured by the two different setups of the rectangular waveguide showed that both modes had very close powers over the operating frequency range as shown in Figure 109 and predicted by the simulated results. The power difference was at a maximum of 1.7 dB at around 72.6 GHz. The measured phase difference between the two orthogonal modes was between 90° and 105° in the operating frequency band as shown in Figure 110. The phase difference values might be affected by the connection of the rectangular waveguide to the circular waveguide without any transitions. These results show that a circularly polarized wave was present at the circular output of the polarizer.

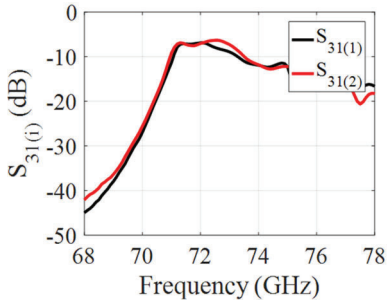

Figure 109. Plots of the Power Received by Port 3 from Port 1 for Two Orthogonal TE_{11} Modes

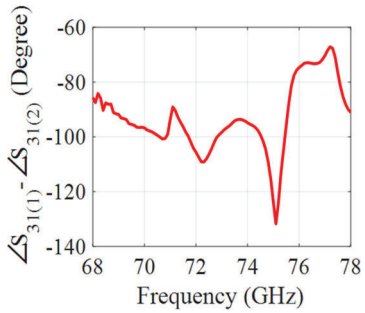

Figure 110. Plots of the Phase Difference between the Two Orthogonal TE_{11} Modes Seen at Port 3

4.3.2 Dual Slot Polarizer Using Serpentine Power Combiner

The performance of the serpentine combiner is discussed in what follows and a comparison with the single slot polarizer is performed. The serpentine power combiner was used to feed the conical horn producing a gain of 23 dB as shown in Figure 84. A tapered circular waveguide of length L_{trans} = 8 mm was used to match the polarizer to the conical horn.

By examining the E-fields inside the system, it was noticed that the slot closer to the feeding port extracted the most power from the rectangular waveguide as seen in Figure 111. The intensity of the E-field decreased after passing slot 1 and it decreased again after passing slot 2. In the circular waveguides used for extracting the power and feeding it to the serpentine combiner, two orthogonal TE_{11} modes can be seen. These modes were combined at the end of the serpentine combiner and the intensity of the E-field is shown to have increased.

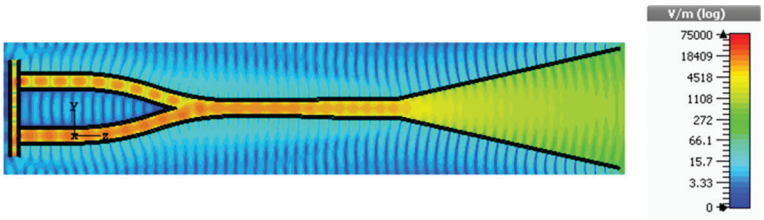

Figure 111. The E-field Inside the Different Parts of the System at 84 GHz

The *s*-parameters of the system, shown in Figure 112, show that the system was well matched for the frequency range 80 – 86 GHz. The system showed two different resonances at 82 and 83.5 GHz caused by the coupling between the slots. Those resonances created two different frequency bands where the isolation between ports 1 and 2 was $|S_{21}| > 10$ dB. These frequency bands were BW_1 = 81.8 – 82.35 GHz and BW_2 = 82.9 – 83.9 GHz. BW_2 had a range where the isolation reached values higher than 20 dB over a frequency band of 250 MHz.

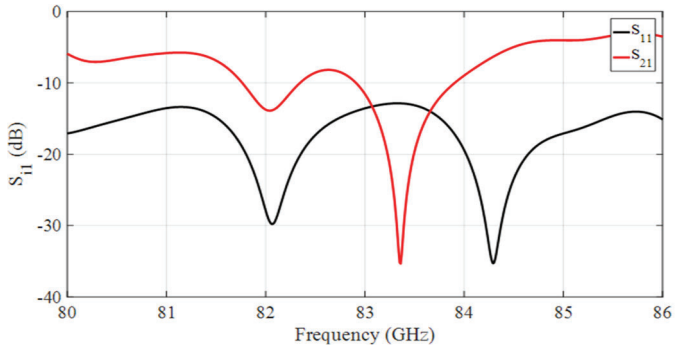

Figure 112. The *s*-Parameters of the System with a Serpentine Power Combiner

The system produced a LHCP main beam if fed by port 1, and a RHCP main beam if fed by port 2. The maximum gain generated by the system, shown in Figure 113, was improved for the frequency range of 80 – 83 GHz in comparison to the single slot polarizer, and it reached values between 20 – 21 dB. In the frequency range of 83 – 86 GHz, the gain decreased in comparison to the single slot polarizer by 1 dB. This decrease was due to the conduction losses in the serpentine combiner due to its large dimensions. The system had an efficiency $50\% < \varepsilon_s < 70\%$ over the frequency band 80 – 86 GHz.

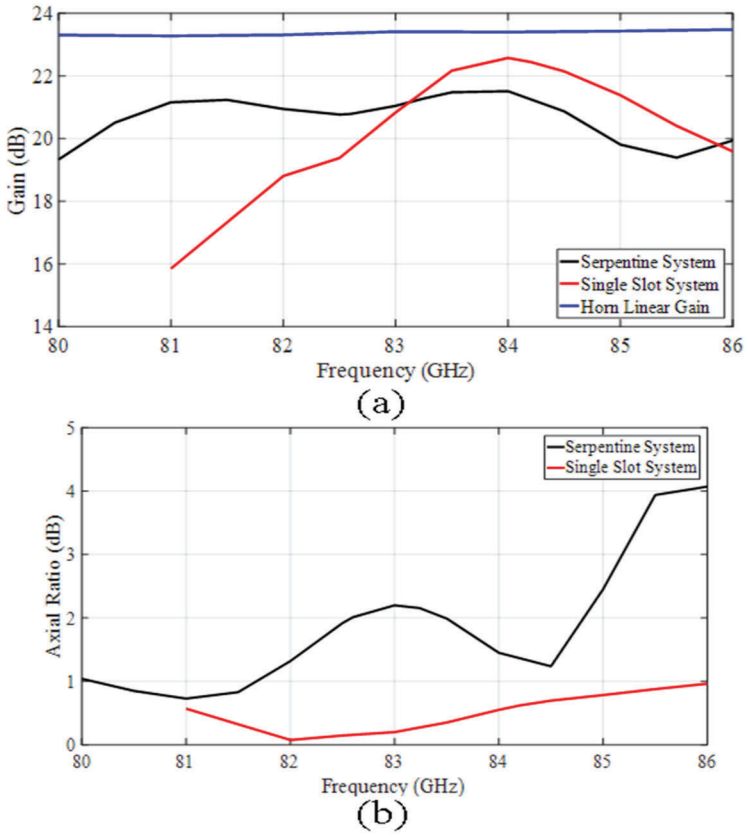

Figure 113. (a) Plot of the Comparison of the Maximum Gain Performance; (b) Plot of the Comparison Between the Axial Ratios of the Serpentine vs the Single Slot Polarizer

The axial ratio of the wave radiated by the serpentine fed horn had values higher than the one fed by the single slot polarizer. This deterioration in the axial ratio was due to the serpentine structure that caused a change in the phase difference between the E-fields of the different TE_{11} modes. However, the axial ratio, in the direction of the maximum gain, was less than 3 dB over the frequency range of 80 – 85.2 GHz as shown in Figure 113. The axial ratio reached a minimum value of 0.65 dB at 81 GHz.

The serpentine polarizer did not affect the radiation pattern of the conical horn. The HPBW of the horn was still 12° in all plane cuts as shown in Figure 114. The reflection coefficient (S_{11}) was improved and reached a value of -27.9 dB for all plane cuts at 84 GHz. The cross-polarization discrimination (XPD) was around 22 dB at 84 GHz and the entire HPBW was circularly polarized.

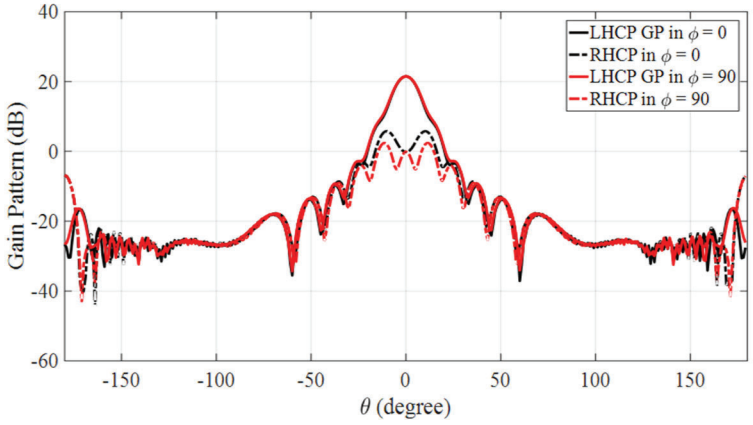

Figure 114. The LHCP and RHCP Radiation Pattern of the Serpentine Fed Horn in Different Plane Cuts at 84 GHz

4.3.3 Dual Slot Polarizer Using A Square Waveguide Power Combiner Results

The power combiner feeds into a pyramidal horn as shown in Figure 101. The pyramidal horn had a gain of 17 dB. As Figure 101 shows, when the wave passes the first slot, its power in the rectangular waveguide was reduced. When it passes the second slot, its power becomes insignificant in the rectangular waveguide. The power transfer into the square waveguides by the slots caused this power reduction. In the square waveguides, the E-fields of the two TE_{10} modes can be seen. These E-fields were in two orthogonal directions all over the entire combiner. Note that there was a phase difference of about ±90° between them. This phase difference was carried through the entire square power combiner and can be seen in the horn. At the intersection plane between the titled waveguides, it can be noticed that the scattering was minimal and the power was being combined successfully, resulting in higher intensities of both E-fields in the power combiner's output waveguide. This was true for both scenarios and for both feeding ports.

For scenario 1, the designed resonant frequency was at 72.4 GHz as shown in Figure 115. The design was well matched for the frequency range 70.5 – 76 GHz. The different loading that was imposed on the slots, in comparison to the single-slot design, caused the shift in the operating frequency. In addition, the coupling between the two slots contributed to this frequency shift. For a better matching to improve the efficiency of the slots, a rectangular ridge was added in the rectangular waveguide on the opposite side of each slot as shown in Figure 116. The ridge had a width W_R = 0.2 mm and a ridge length L_R = 2 mm. The ridge improved the resonant frequency and the 10 dB and 20 dB isolation between ports 1 and 2 as shown in Figure 115, along with the

efficiency of the system. The ridge did not affect the input matching bandwidth. The design of scenario 1 had an isolation of $|S_{21}| > 10$ dB in the frequency range 71.7 – 73.1 GHz with or without a ridge installed in the rectangular waveguide. The $|S_{21}|$ was greater than 20 dB for a bandwidth of 400 MHz in the case of a ridge, and 300 MHZ when the ridge was not added. The same *s*-parameter results were obtained if port 2 was fed instead of port 1.

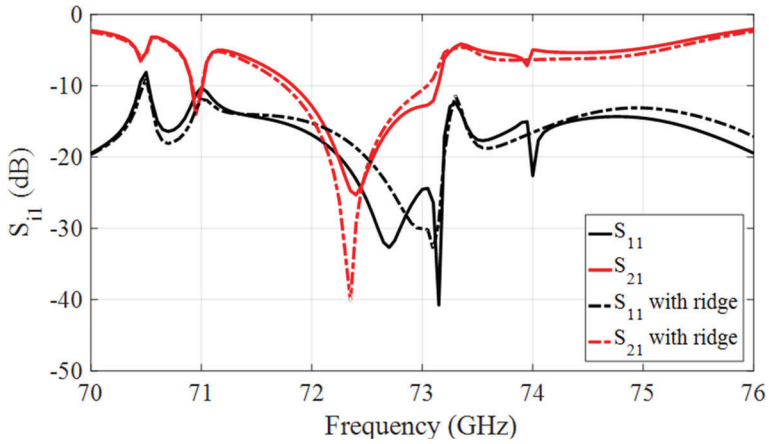

Figure 115. *S*-Parameters Comparison Between a Regular Combiner and a Combiner with a Ridge

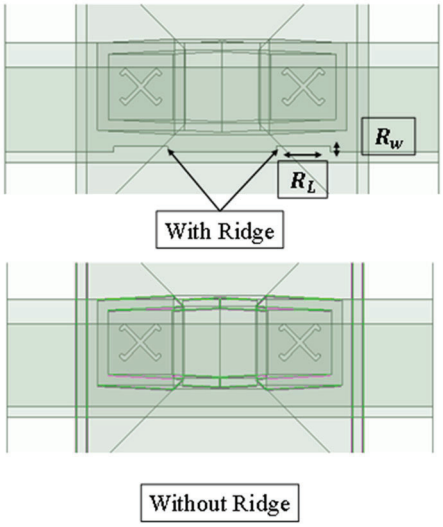

Figure 116. Illustration of the Design with and Without a Ridge in the Rectangular Waveguide

Simulations indicate that scenario 1 produced a maximum gain of 17.1 dB at 72.4 GHz with or without the ridge. At this frequency, the system had a total efficiency of $\varepsilon_{c,max} = 89$ %. The system

had a total efficiency of more than $\varepsilon_c > 70$ % over the frequency range 71.5 – 73.1 GHz as shown in Figure 117. The improvement of the gain that the two slot combiner introduced over the single slot fed horn is also shown in Figure 117. The gain improvement is noticed over the frequency band of 70 – 76 GHz. The axial ratio in the direction of the highest gain is shown in Figure 117. For both combiner designs, with or without a ridge, the axial ratio in the direction of the highest gain was less than 3 dB over the bandwidth over which the system had an efficiency of more than 70%. The introduction of the ridge improved the axial ratio between 72 – 73 GHz. The radiation pattern of the horn was not affected by the introduction of the combiner as shown in Figure 118. The HPBW was circularly polarized in all plane cuts over the frequency range 71.7 – 73 GHz. The system exhibited a LHCP main beam when fed through port 1 and RHCP main beam when fed through port 2.

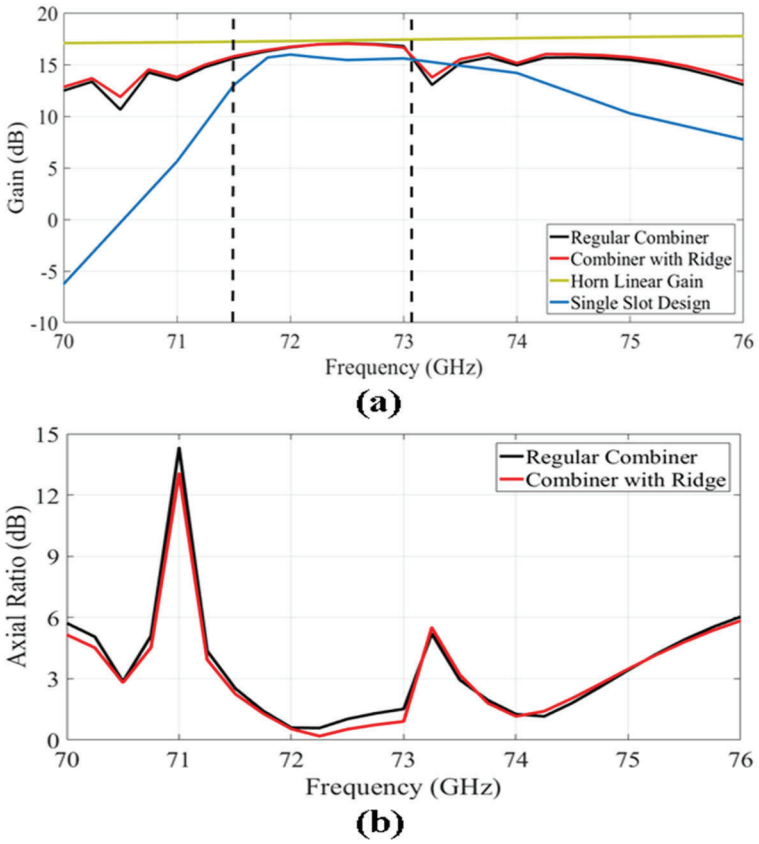

Figure 117. (a) Gain vs Frequency for Different Designs, (b) Axial Ratio vs Frequency for the Rectangular Waveguide with and Without Ridge

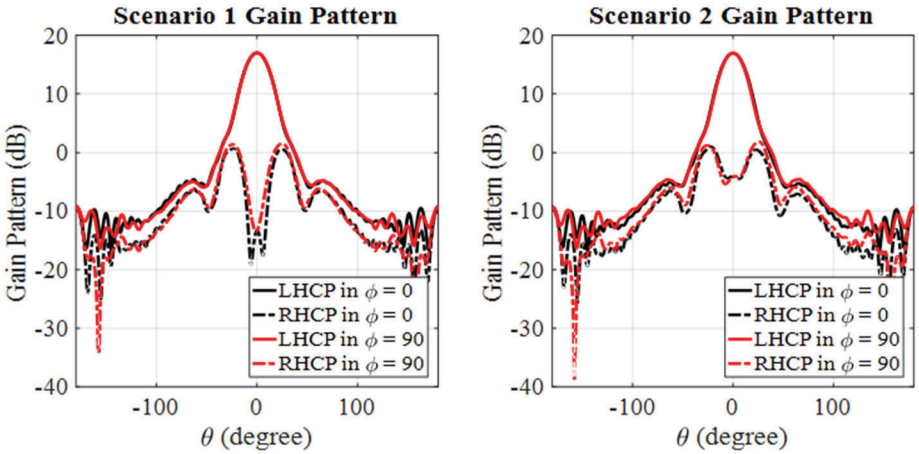

Figure 118. Gain Pattern of Scenarios 1 and 2 for Both LHCP and RHCP When Port 1 is Fed at 72.5 GHz

For scenario 2, the same ridge was also used, since it improved the performance of the system. The resonant frequency of scenario 2 was at f = 72.65 GHz. The shift in resonant frequency in comparison to scenario 1 was caused by the slot 2 size, which was smaller than the size of slot 1. The system was well matched in the frequency bandwidths of 71.4 – 73.4 GHz and 74 – 76 GHz as shown in Figure 119. Scenario 2 shows two different frequency ranges where the isolation between ports 1 and 2 was good, showing a good slot power extraction in these frequency bands, which promises a good polarizer efficiency in these ranges. The isolation between ports 1 and 2 was $|S_{21}| > 10$ dB for the frequency range 72.2 – 73.2 GHz. The isolation 7 dB $< |S_{21}| <$ 9.5 dB in the frequency range 74.2 – 75.2 GHz. In these two bands the system worked well as a polarizer. This is shown in the analysis of the radiation properties of the horn in scenario 2.

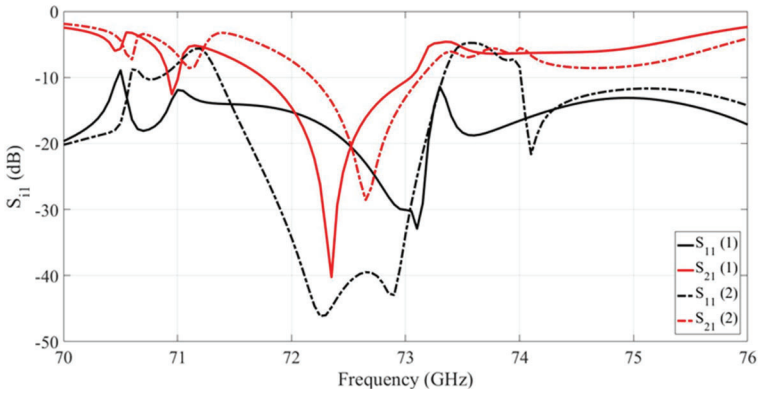

Figure 119. *S*-Parameters of the Different Scenarios versus Frequency

The maximum gain achieved in scenario 2 was 17.1 dB at 71.65 GHz. The system total efficiency was $\varepsilon_{c,max}$ = 84% at this frequency. This scenario exhibited two frequency ranges, BW_1 = 71.9 – 73.1 GHz and BW_2 = 74.3 – 75.2 GHz where the system total efficiency was ε_c > 70% as shown in Figure 120. The axial ratio over these two frequency bandwidths was less than 3 dB as shown in Figure 120. Note that over BW_1, the axial ratio of scenario 2 was higher than scenario 1. This deterioration in axial ratio was caused by slot 2, since it had a resonance at a higher frequency. In BW_2, both the gain and the axial ratio of scenario 2 were improved in comparison to scenario 1. The radiation pattern of the horn was not affected by scenario 2 as shown in Figure 118. The reflection coefficient (S_{11}) and HPBW were the same as in the case of a linear gain horn. The HPBW of the system was entirely circularly polarized, exhibiting a LHCP when fed through port 1 and a RHCP when fed through port 2, and an axial ratio AR > 3 dB for all the angles and plane cuts.

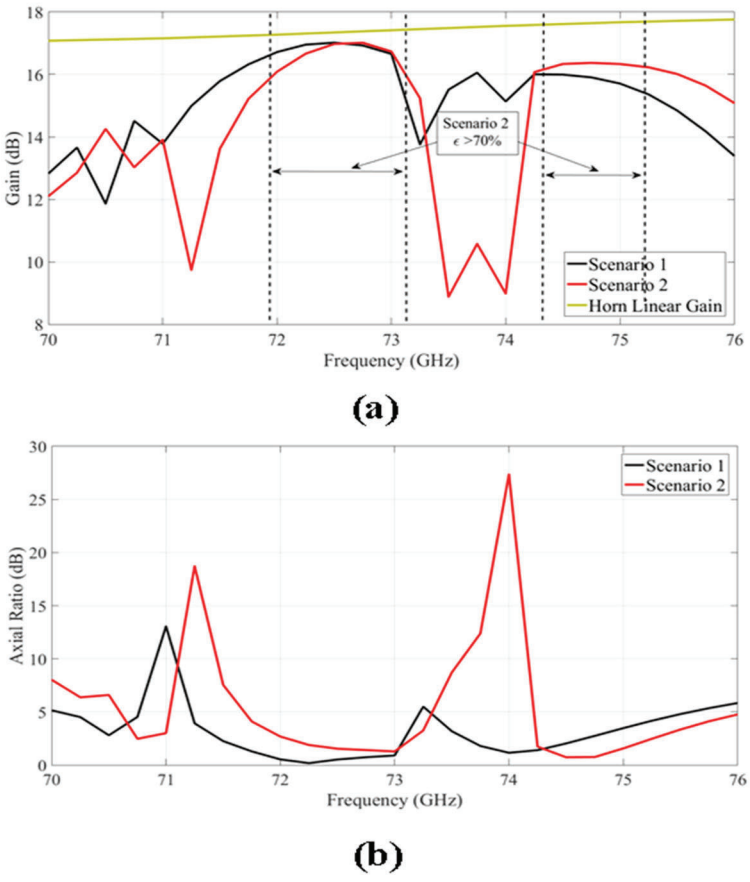

Figure 120. (a) Gain Comparison versus Frequency, (b) Axial Ratio Comparison versus Frequency for Scenarios 1 and 2

5 CONCLUSIONS

5.1 Atmosphere Propagation Effects Conclusions

Atmospheric propagation effects are critical parts of a satellite communication link budget at W/V-band. This report presented fundamental concepts for modeling absorption and scattering by atmosphere gases, clouds, and precipitation. Calculations of specific attenuation, optical thickness, and opacity were illustrated using the Standard Atmosphere model and radiosonde measurements.

Radiosonde data are measured twice daily at many locations around the world. Results presented in this work suggest that radiosonde data can be used to calculate relatively good estimates of clear-day attenuation. We recommend continued analysis of radiosonde data to assess utility for developing W/V-band link budget models.

The W/V-band Terrestrial Link Experiment (WTLE) was used to compare model estimates of attenuation (rather, received signal power) to actual measurements for clear and cloudy conditions. The agreement between model estimates and measured data during clear conditions was extraordinary. We recommend comparison of model estimates using WTLE data to model estimates using radiosonde data. It would be informative assess the degree to which radiosonde data can be interpolated and still provide reasonable estimates of clear-day attenuation. In other words, determine whether interpolated radiosonde data can replace weather measurements (temperature, pressure, and relative humidity) at the receiver and transmitter sites. This could support and validate clear-day attenuation modeling based on radiosonde measurements.

Liquid water precipitation was shown to be the most significant source of extinction on a propagation path. Liquid water precipitation causes both absorption and scattering of W/V-band electromagnetic waves. Effects from frozen precipitation are about two-orders of magnitude less than that of liquid precipitation. AFRL continues to lead model development and validation efforts related to precipitation effects at W/V-band.

Cloud attenuation is relatively less than attenuation from liquid water precipitation, but cloud attenuation generally occurs more frequently and is significant. As with liquid precipitation, our modeling ability is limited by our lack of knowledge of the density of the water particles on the propagation path (i.e., liquid water content), and the extent (i.e., distance) to which they occur on the path. Four models were presented and then used to estimate attenuation effects from clouds on the WTLE propagation path. The cloud models included: (1) an adiabatic lifting model, (2) Decker model (1977), (3) Salonen model (1991), and (4) Mattioli model (2009). The WTLE “cloudy condition” scenario that was presented is representative of partial-path obscuration by a stratus, non-precipitating cloud event. Although weather data from both the receiver site and the transmitter site were available in 1 minute increments, we were unable to predict deep-fade events and suffered false positives. Nevertheless, we recommend analysis of additional events of cloudy conditions to assess variability of model performance.

New radiometer technology developed over the last decade provides atmospheric attenuation estimates at 72 GHz and 84 GHz, in addition to estimating the integrated water path and liquid water content. New multichannel profilometers can provide detailed information regarding cloud

cover and precipitation events. AFRL has multichannel radiometers capable of measuring meteorology parameters and estimating W/V-band attenuation. We recommend analysis of radiometer data to assess correlation with clear-day estimates that can be derived from radiosonde measurements. The reliability of radiosonde measurements for predicting path opacity at W/V-band is still an area of on-going research.

This work showed that cloud models can be tuned to provide reasonable estimates of attenuation (i.e., optical thickness) over a period of time and in a statistical sense, but data also indicated that models cannot accurately predict deep-fade events, which are critical for link budget models. Therefore, whether for WTLE or for a satellite link, physics-based models and empirical "curve fit" models must be verified and validated with measured data[17]. For WTLE, we recommend analyzing multiple prior years of data to establish a baseline empirical model (i.e., exceedance probability function), which can then be validated against future measurements. This would facilitate uncertainty estimation (i.e., standard deviation or variance) of the model. For a satellite link, there is no better alternative than to use a geostationary beacon to statistically characterize propagation effects. A beacon provides data that are traceable to the application, and enables continuous measurements that are needed to capture deep-fade events. We recommend coupling beacon measurement with analysis of meteorology data, radiosonde data, and radiometer data. It would be beneficial if modeling tools can be developed and validated that synthesize reasonable estimates of atmosphere effects based on meteorology data, radiosonde data, and radiometer data. Those tools could then be applied to estimate link performance in locations for which validation by beacon measurement are not available or possible.

5.2 Rectangular Waveguide Antenna Array Conclusions

A new high-gain, circularly polarized waveguide antenna array was presented. The waveguide antenna array had eight elements with *z*-shaped cross-slots across each element's broad-wall. The rectangular waveguide array operated between 84.35 – 85.8 GHz. The array produced right-hand circularly polarized radiation with a main-beam in the direction $\theta = 40°$ if fed through port 1, and left-hand circularly polarized radiation with a main-beam in the direction $\theta = -40°$ if fed through port 2. The gain achieved for both ports was between 23 – 24.5 dB. The half-power beam width had an elliptical shape and was entirely circularly polarized in both elevation and azimuthal planes. The isolation between the co- and cross-polarized gain patterns in the direction of the maximum gain was more than 20 dB for both ports. The array was proven to be a good candidate for point-to-point terrestrial communication systems as well as satellite-to-earth communication systems.

[17] Model verification and validation are the primary processes for quantifying and building credibility in numerical models. Verification is the process of determining that a model implementation accurately represents the developer's conceptual description of the model and its solution. Validation is the process of determining the degree to which a model is an accurate representation of the real world from the perspective of the intended uses of the model. Both verification and validation are processes that accumulate evidence of a model's correctness or accuracy for a specific scenario; thus, V&V cannot prove that a model is correct and accurate for all possible scenarios, but, rather, it can provide evidence that the model is sufficiently accurate for its intended use [61].

5.3 Cross-Slotted Waveguide-Fed Horn Antenna Conclusions

The large size of the serpentine combiner decreases its efficiency due to conduction losses. The polarizer improved the gain performance of the system at frequencies close to the resonant frequencies of the slots. Scenario 1 improved the bandwidth over which the system had good efficiency and good isolation between both ports. The system worked as an efficient polarizer for a bandwidth of 2.2% of the frequency band. Scenario 2 created two separate but close frequency bands where the system worked well as a polarizer with a bandwidth of 1.4% and 1.6% of the frequency band.

REFERENCES

[1] Friis, H. T., "A Note on a Simple Transmission Formula," *Proceedings of the IRE*, Volume: 34, Issue: 5 May 1946, pp. 254-256.

[2] Ulaby, F. T. and Long, D. G., *Microwave Radar and Radiometric Remote Sensing*, University of Michigan Press, Ann Arbor, MI, 2014, pp. 85-87.

[3] Ulaby, F. T. and Long, D. G., *Microwave Radar and Radiometric Remote Sensing*, University of Michigan Press, Ann Arbor, MI, 2014, pp. 35.

[4] Demarest, K. R., *Engineering Electromagnetics*, Prentice Hall, Hoboken, NJ, 1998, pp. 122.

[5] Ulaby, F. T. and Long, D. G., *Microwave Radar and Radiometric Remote Sensing*, University of Michigan Press, Ann Arbor, MI, 2014, pp. 328-333.

[6] *Recommendation ITU-R P.676-11, (09/2016), Attenuation by Atmospheric Gases*, International Telecommunications Union, 2016.

[7] Liebe, H. J., "Modeling Attenuation and Phase of Radio Waves in Air at Frequencies below 1000 GHz," *Radio Science*, Vol. 16, No. 6, 1981, pp. 1183-1199.

[8] Liebe, H. J., "An Updated Model for Millimeter Wave Propagation in Moist Air," *Radio Science*, Vol. 20, No. 5, 1985, pp. 1069-1089.

[9] Liebe, H. J., Hufford, G., and Cotton, M., "Propagation Modeling of Moist Air and Suspended Water / Ice Particles at Frequencies Below 1000 GHz," *AGARD Conference Proceeding*s, 1993.

[10] *Recommendation ITU-R P.835-6 (12/2017), Reference Standard Atmospheres*, International Telecommunications Union, 2017.

[11] Ulaby, F. T. and Long, D. G., *Microwave Radar and Radiometric Remote Sensing*, University of Michigan Press, Ann Arbor, MI, 2014, pp. 326-328.

[12] Sonntag, R. E., Borgnakke, C., and Van Wylen, G. J., *Fundamentals of Thermodynamics*, 6th Edition, John Wiley and Sons, New York, NY, 2003, Table A.5, pp. 658.

[13] Sonntag, R. E., Borgnakke, C., and Van Wylen, G. J., *Fundamentals of Thermodynamics*, 6th Edition, John Wiley and Sons, New York, NY, 2003, pp. 480-482.

[14] Sonntag, R. E., Borgnakke, C., and Van Wylen, G. J., *Fundamentals of Thermodynamics*, 6th Edition, John Wiley and Sons, New York, NY, 2003, pp. 513.

[15] Brune, W., *Fundamentals of Atmospheric Science*, LibreTexts Project (https://LibreTexts.org), 2022.

[16] Sonntag, R. E., Borgnakke, C., and Van Wylen, G. J., *Fundamentals of Thermodynamics*, 6th Edition, John Wiley and Sons, New York, NY, 2003, Table B.1.1, pp. 674.

[17] Sonntag, R. E., Borgnakke, C., and Van Wylen, G. J., *Fundamentals of Thermodynamics*, 6th Edition, John Wiley and Sons, New York, NY, 2003, Table B.1.5, pp. 690.

[18] Ulaby, F. T. and Long, D. G., *Microwave Radar and Radiometric Remote Sensing*, University of Michigan Press, Ann Arbor, MI, 2014, pp. 333-338.

[19] Ulaby, F. T. and Long, D. G., *Microwave Radar and Radiometric Remote Sensing*, University of Michigan Press, Ann Arbor, MI, 2014, pp. 342.

[20] Mie, G., "Beiträge zur Optik trüber Medien, speziell kolloidaler Metallösungen," *Annalen der Physik*, Vol. 330, No. 3, 1908, p. 377-445.

[21] Deirmendjian, D, *Electromagnetic Scattering on Spherical Polydispersions*, Elsevier, NY, 1969.

[22] Ulaby, F. T. and Long, D. G., *Microwave Radar and Radiometric Remote Sensing*, University of Michigan Press, Ann Arbor, MI, 2014, pp. 343.

[23] van de Hulst, H. C., *Light Scattering by Small Particles*, Wiley & Sons, New York, NY, 1957.

[24] Mätzler, C., *Thermal Microwave Radiation: Applications for Remote Sensing*, Institution of Engineering and Technology, Stevenage, UK, 2006, pp. 431-455.

[25] Mätzler, C. and Wegmüller, U., "Dielectric Properties of Fresh Water Ice at Microwave Frequencies," *Journal of Physics D Applied Physics*, Vol. 20, 1987, pp. 1623-1630.

[26] Ulaby, F. T. and Long, D. G., *Microwave Radar and Radiometric Remote Sensing*, University of Michigan Press, Ann Arbor, MI, 2014, pp. 128.

[27] Wegmüller, U., *Signaturen zur Mikrowellen-Fernerkundung: Bodenrauhigkeit und Permittivitat von Eis*, Thesis, Institut fur Angewandte Physik der Universität Bern, Germany, 1986.

[28] Carro-Calvo, L., Hoose, C., Stengel, M., and Salcedo-Sanz, S., "Cloud Glaciation Temperature Estimation from Passive Remote Sensing Data with Evolutionary Computing," *Journal of Geophysical Research: Atmospheres*, 121, 2016, pp. 13,591–13,608.

[29] Findeisen, W., "Die Kolloidmeteorologischen Vorgänge bei der Niederschlagsbildung (Colloidal Meteorological Processes in the Formation of Precipitation)," *Meteorologische Zeitschrift*, Vol. 55, 1938, pp. 121–133, (translated and edited by Volken, E., Giesche, A. M., and Brönnimann, S., *Meteorologische Zeitschrift*, Vol. 24, 2015.

[30] Hallett, J. and Mossop, S. C., "Production of Secondary Ice Particles During the Riming Process," *Nature*, Vol. 249, 1974, pp. 26–28.

[31] Korolev, A. V., Isaac, G. A., Cober, S. G., Strapp, J. W., and Hallett, J., "Microphysical Characterization of Mixed-phase Clouds," *Q. J. R. Meteorology Society*, Vol. 129, 2003, pp. 39–65.

[32] Lloyd, G., et al. (2015), "The Origins of Ice Crystals Measured in Mixed-Phase Clouds at the High-Alpine Site Jungfraujoch," *Atmos. Chem. Phys.*, Vol. 15, pp. 12,953-12,969.

[33] Hakim, G. and Patoux, J., *Weather, A Concise Introduction*, Cambridge University Press, New York, NY, 2018, pp. 90-112.

[34] Wallace, J. M. and Hobbs, P. V., *Atmospheric Science, An Introductory Survey*, 2nd Edition, Elsevier, Burlington, MA, 2006, pp. 67.

[35] Wallace, J. M. and Hobbs, P. V., *Atmospheric Science, An Introductory Survey*, 2nd Edition, Elsevier, Burlington, MA, 2006, pp. 77.

[36] Wallace, J. M. and Hobbs, P. V., *Atmospheric Science, An Introductory Survey*, 2nd Edition, Elsevier, Burlington, MA, 2006, pp. 106.

[37] Wallace, J. M. and Hobbs, P. V., *Atmospheric Science, An Introductory Survey*, 2nd Edition, Elsevier, Burlington, MA, 2006, pp. 216-217.

[38] Ulaby, F. T. and Long, D. G., *Microwave Radar and Radiometric Remote Sensing*, University of Michigan Press, Ann Arbor, MI, 2014, pp. 349.

[39] Fraser, K. S., et al, "Interaction Mechanisms Within the Atmosphere," *Manual of Remote Sensing: Interpretation and Applications*, American Society of Photogrammetry, 1975.

[40] Allnutt, J. E., *Satellite-to-Ground Radiowave Propagation*, 2nd Edition, Institute of Engineering and Technology, London, 2011, pp. 175.

[41] Dissanayake, A. W., Allnutt, J. E., and Haidara, F., "A Prediction Model That Combines Rain Attenuation and Other Propagation Impairments Along Earth-Satellite Paths," *IEEE Transactions of Antennas Propagation*, Vol 45, No. 10, 1997, pp. 1546-1558.

[42] Kampe, H. J., "Visibility and Liquid Water Content in Clouds in the Free Atmosphere," *Journal of Meteorology*, Vol. 7, 1950, pp. 54-57.

[43] Decker, M. T., Westwater, E. R., and Guiraud, F. O., "Experimental Evaluation of Ground-Based Microwave Radiometric Sensing of Atmospheric Temperature and Water Vapor Profiles," *Journal of Applied Meteorology and Climatology*, Vol. 17, No. 12, 1978, pp. 1788-1795.

[44] Salonen, E. and Uppala, W., "New Prediction Method of Cloud Attenuation," Electronics Letters, Vol. 27, No. 12, 1991, pp. 1106-1108.

[45] Mattioli, V., Basili, P., Bonafoni, S., Ciotti, P., and Westwater, E., "Analysis and Improvements of Cloud Models for Propagation Studies," *Radio Science*, Vol. 44, 2009, pp. 1-13.

[46] Laws, J. O. and Parsons, D. A., "The Relation of Rain Drop Size to Intensity," *Transactions of the American Geophysical Union*, Vol. 24, 1943, pp.452-460.

[47] Wexler, R., "Rain Intensities by Radar," *Journal of Meteorology*, Vol. 5, Number 4, 1948, pp. 171-173.

[48] Marshall, J. S. and Palmer, W. M., "The Distribution of Raindrops with Size," *Journal of Meteorology*, Vol. 5, Number 4, 1948, pp. 165-166.

[49] Best, A. C., "The Size Distribution of Raindrops," *Quarterly Journal of the Royal Meteorological Society*, Vol. 76, Number 327, 1950, pp. 16-36.

[50] de Wolf, D. A., "On the Laws-Parsons Distribution of Raindrop Sizes," *Radio Science*, Vol. 36, No. 4, 2001, pp. 639-642.

[51] Olsen, R., Rogers, D. V., and Hodge, D. B., "The aR^b Relation in the Calculation of Rain Attenuation," *IEEE Transactions on Antennas and Propagation*, , Vol. 26, No. 2, 1978, pp. 318-329.

[52] Ulaby, F. T. and Long, D. G., *Microwave Radar and Radiometric Remote Sensing*, University of Michigan Press, Ann Arbor, MI, 2014, pp. 356.

[53] *Recommendation ITU-R P.838-3 (2005), Specific Attenuation Model for Rain for Use in Prediction Methods*, 2005.

[54] CCIR, *Attenuation by Precipitation and Other Atmospheric Particles*, ITU, Draft Report 721 (Mod F), Document 5/5046, Committee Consultative Internationale de Radio, Geneva, Switzerland, 1981.

[55] Pratt, T. and Allnutt, J. E., *Satellite Communications*, 3rd Edition, John Wiley & Sons, Hoboken, NJ, 2020, pp. 360.

[56] *Recommendation ITU-R P.618-10, Propagation Data and Prediction Methods Required for the Design of Earth-Space Telecommunication Systems*, 2010.

[57] Tarasenko, N., *Design and Implementation of a 72 & 84 GHz Terrestrial Propagation Experiment; Exploitation of NEXRAD Data to Statistically Estimate Rain Attenuation at 72 GHz*, PhD Dissertation, University of New Mexico, Albuquerque, NM, 2019.

[58] Pratt, T. and Allnutt, J. E., *Satellite Communications*, 3rd Edition, John Wiley & Sons, Hoboken, NJ, 2020, pp. 358.

[59] Pratt, T. and Allnutt, J. E., *Satellite Communications*, 3rd Edition, John Wiley & Sons, Hoboken, NJ, 2020, pp. 364.

[60] King, A. P., "The Radiation Characteristics of Conical Horn Antennas," *Proceedings of the IRE*, Vol. 38, 1950, pp. 249-251.

[61] Schaller, C., editor, *Concepts of Model Verification and Validation*, LA-14167-MS, Los Alamos National Laboratory, 2004, pp. v.

LIST OF SYMBOLS, ABBREVIATIONS AND ACRONYMS

α	Absorption Constant
β	Phase Constant
χ	Normalized Particle Circumference
ε	Average Relative Dielectric Constant of a Material
Δh_{cl}	Cloud Layer Thickness
ε_0	Permittivity of Free Space
ε_h	Efficiency of Horn Antenna
ε'	Relative Permittivity
ε''	Dielectric Loss Factor
ϕ	Relative Humidity
ϕ	Also used to indicate elevation plane for antenna
γ	Propagation Constant
Γ_d	Dry Adiabatic Lapse Rate
Γ_m	Moist Adiabatic Lapse Rate
φ	Mixing Ratio
κ_a	Absorption Coefficient, (Np/m), (dB/km)
$\kappa_{a_{cl}}$	Absorption Coefficient for Clouds, Cloud Volume Absorption Coefficient, (Np/m), (dB/km)
κ_{a_g}	Absorption Coefficient for Atmosphere Gases, (Np/m), (dB/km)
κ_{a_p}	Absorption Coefficient for Precipitation, (Np/m), (dB/km)
κ_e	Extinction Coefficient, (Np/m), (dB/km)
$\kappa_{e_{rn}}$	Rain Volume Extinction Coefficient
κ_I	Ice Extinction Coefficient, (Np/m)/(g/m^3)
κ_L	Liquid Extinction Coefficient, (Np/m)/(g/m^3)
κ_s	Scattering Coefficient
λ	Wavelength
λ_0	Wavelength in Free Space
μ	Magnetic Permeability
μm	Micrometer, unit of length (1e-6 m)

μ_0	Permeability in Free Space
θ	Used to indicate azimuthal plane for antenna
Θ	Antenna Half Power Beam Width
ρ_d	Density of Dry Air
ρ_L	Density of Liquid Water
ρ_p	Parcel Density
ρ_v	Volume Charge Density
ρ_v	Density of Water Vapor
σ	Conductivity
τ	Optical Thickness, Opacity
τ_0	Zenith Optical Thickness, Zenith Opacity
ω	Angular Frequency (rad/sec)
ξ_a	Absorption Efficiency Factor
ξ_e	Extinction Efficiency Factor
ξ_s	Scattering Efficiency Factor
ψ	Polarization Tilt Angle Relative to the Horizontal
AR	Axial Ratio
A_p	Particle Physical Cross Section Area
c	Speed of Light in Vacuum
C	Coulomb, unit of charge
c_p	Specific Heat of Air
CNR	Carrier to Noise Ratio
CP	Circular Polarization
COSMIAC	Configurable Space Microsystems Innovations and Applications Center
dB	Decibel
d_i	Rain Drop Diameter
e	Partial Pressure of Water Vapor
e_s	Saturation Pressure of Water Vapor
e_{si}	Saturation Pressure of Ice

E_0	Field Intensity at $z = 0$
E_b	Energy per Bit
EM	Electromagnetic
f	Angular Frequency (sec^{-1}) (Hz)
F	Faraday, unit of capacitance
g	Acceleration Due to Gravity
GHz	Giga Hertz (1e9 Hz)
G_r	Receive Antenna Gain
G_t	Transmit Antenna Gain
H	Henry, unit of inductance
h_b, h_{base}	Cloud Base Height
$h_{surface}$	Altitude or Height of the Surface
HPBW	Half Power Beam Width
hPa	Hecto Pascal, unit of pressure (1e2 Pa)
ITU	International Telecommunications Union
ITU-R	International Telecommunications Union - Radio
j	$\sqrt{-1}$
J	Joule, unit of energy
k	Wavenumber (m^{-1})
K	Kelvin, unit of temperature
kg	Kilogram, unit of mass
km	Kilometer, unit of length
k_0	Wavenumber in Free Space
L_{atm}	Atmospheric Loss
L_{cell}	Length of the Base of a Storm Cell
LCL	Lifted Condensation Level
L_{FS}	Free Space Loss
LHCP	Left Hand Circular Polarization
$L_{pointing}$	Antenna Pointing Loss

L_s	Enthalpy of Sublimation
L_{TL}	Transmission Line Loss
L_v	Enthalpy of Vaporization
LWC	Liquid Water Content
m	Meter, unit of length
mm	Millimeter, unit of length (1e-3 m)
m_d	Mass of Dry Air
m_L	Mass Density of Liquid Water of the Mixture, Liquid Water Content
m_v	Mass of Water Vapor
n	Index of Refraction, Relative Index of Refraction
n_b	Index of Refraction of Background Material (air)
n_0	Noise Power Spectral Density
n_p	Index of Refraction of Particle (water (vapor, liquid, ice))
NEXRAD	Next Generation Weather Radar
Np	Neper, unit for ratio of fields or power quantities
p	Pressure
P_a	Power Absorbed
P_d	Partial Pressure of Dry Air
P_e	Power Extinction
P_p	Parcel Total Pressure
P_r	Received Power
P_s	Power Scattered
P_t	Transmitted Power
P_t, p_t	Total Atmospheric Pressure
Q_a	Effective Absorption Cross Section Area
Q_e	Extinction Cross Section Area
Q_s	Effective Scattering Cross Section Area
R	Propagation Distance
rad	Radians

R_d	Gas Constant for Dry Air (287 J/(kg·K))
R_r	Rainfall Rate
R_v	Gas Constant for Water Vapor (461.51 J/(kg·K))
RF	Radio Frequency
RH	Relative Humidity
RH_c	Critical Relative Humidity
RHCP	Right Hand Circular Polarization
S	Specific Attenuation (dB/km)
S	Siemens, unit of conductivity
sec	Seconds, unit of time
SNR	Signal to Noise Ratio
S_{11}	Reflection Coefficient
S_{21}	Isolation Between Port 1 and Port 2
T	Temperature
TE_{11}	Transverse Electric Wave
TM_{01}	Transverse Magnetic Wave
T_0	Standard Temperature at Sea Level
T_p	Parcel Temperature
TWC	Total Water Content
T_v	Virtual Temperature of Parcel
u_p	Phase Velocity
UTC	Universal Coordinated Time
V_p	Particle Volume
W	Watts, unit of power
w_s	Saturation Mixing Ratio
WTLE	W/V-band Terrestrial Link Experiment
XPD	Cross Polarization Discrimination
XPI	Cross Polarization Isolation

DISTRIBUTION LIST

DTIC/OCP
8725 John J. Kingman Rd, Suite 0944
Ft Belvoir, VA 22060-6218 1 cy

AFRL/RVIL
Kirtland AFB, NM 87117-5776 1 cy

Official Record Copy
AFRL/RVB/Dr. Steven A. Lane 1 cy